Dissertation Advisor: Vinothan N. Manoharan Sofia Magkiriadou

Structural Color from Colloidal Glasses

Abstract

When a material has inhomogeneities at a lengthscale comparable to the wavelength of light, interference can give rise to structural colors: colors that originate from the interaction of the material's microstructure with light and do not require absorbing dyes. In this thesis we study a class of these materials, called *photonic glasses*, where the inhomogeneities form a dense and random arrangement. Photonic glasses have angle-independent structural colors that look like those of conventional dyes. However, when this work started, there was only a handful of colors accessible with photonic glasses, mostly hues of blue.

We use various types of colloidal particles to make photonic glasses, and we study, both theoretically and experimentally, how the optical properties of these glasses relate to their structure and constituent particles. Based on our observations from glasses of conventional particles, we construct a theoretical model that explains the scarcity of yellow, orange, and red photonic glasses. Guided by this model, we develop novel colloidal systems that allow a higher degree of control over structural color. We assemble glasses of soft, core-shell particles with scattering cores and transparent shells, where the resonant wavelength can be tuned independently of the reflectivity. We then encapsulate glasses of these core-shell particles into emulsion droplets of tunable size; in this system, we observe, for the first time, angle-independent structural colors that cover the entire visible spectrum. To enhance color saturation, we begin experimenting with *inverse* glasses, where the refractive index of the particles is lower

than the refractive index of the medium, with promising results. Finally, based on our theoretical model for scattering from colloidal glasses, we begin an exploration of the color gamut that could be achieved with this technique, and we find that photonic glasses are a promising approach to a new type of long-lasting, non-toxic, and tunable pigment.

Contents

Title Page i
Abstract iii
Table of Contents v
List of Figures vii
Prior Publications xvi
Acknowledgments xvii

1 Introduction **1**
1.1 Scattering from Photonic Materials 3
1.1.1 Photonic Crystals 3
1.1.2 Photonic Glasses 7
1.1.3 Photonic Glasses in Fourier Space and their Scattering Properties 12
1.2 Previous Work on Photonic Glasses 14
1.3 Overview 15

2 Disordered Packings of Core-Shell Particles with Angle-Independent Structural Colors **17**
2.1 Introduction 17
2.2 Experimental Details 19
2.2.1 Synthesis and Characterization of Core-Shell Particles 19
2.2.2 Assembly of Core-Shell Particles into Disordered Packings . . 20
2.2.3 Characterization of Packings 21
2.3 Results and Discussion 23
2.3.1 Structure of Core-Shell Packings 23
2.3.2 Optical properties 23
2.4 Conclusions 30

3 On the Absence of Red Structural Color in Photonic Glasses, Bird Feathers and Certain Beetles **31**
3.1 Introduction 31
3.2 Experiment 33

3.3 Theory . . . 35
3.4 Results and Discussion . . . 39
3.5 Conclusion . . . 54

4 Full-Spectrum Photonic Pigments with Non-Iridescent Structural Colors through Colloidal Assembly 56
4.1 Introduction . . . 56
4.2 Methods . . . 57
4.3 Results and Discussion . . . 62

5 Inverse Glasses 71
5.1 Introduction . . . 71
5.2 Theory . . . 72
5.3 Experiments . . . 76
5.3.1 Infiltration of Colloidal Glasses with High-Refractive Index Oils 76
5.3.2 Air Cavities in a Silica Matrix . . . 78
5.3.3 Spectrometry . . . 80
5.4 Results and Discussion . . . 81
5.4.1 Infiltrated Colloidal Glasses . . . 81
5.4.2 Air Cavities in a Silica Matrix . . . 83
5.5 Conclusion . . . 87

6 Towards Design Rules for Photonic Glasses as Pigments 89
6.1 Introduction . . . 89
6.2 From Scattering Theory to Color . . . 91
6.3 sRGB Colors of Photonic Glasses . . . 93
6.4 Results and Discussion . . . 94
6.5 Conclusion . . . 100

7 Conclusion and Outlook 101

Bibliography 105

A Protocol for Inverse Glasses of Air Cavities in Silica 113
A.1 Clean the substrates . . . 113
A.2 Prepare the silica precursor . . . 114
A.3 Prepare the colloidal suspensions . . . 114
A.4 Retrieve the substrates . . . 115
A.5 Assemble it all together for slow evaporation . . . 116
A.6 Bake . . . 117

B Analytic Structure Factor for a Glass of Hard Spheres 118

List of Figures

1.1 (a) A flat surface reflects light specularly. (b) A rough surface reflects light specularly on each of its microsurfaces; overall, light is scattered in many directions, diffusely. 2

1.2 Photonic crystals reflect light specularly, and the color of reflected light depends on the orientation of the material. (a) Crystalline packing of polystyrene spheres with diameter $\sim$ 230 nm. (b) The packing shown in (a) looks bright orange when viewed at an angle close to the illumination axis, as shown in the left schematic of (c). The same packing looks bright green when viewed at about 50° with respect to the illumination axis, as shown in the right schematic of (c). 4

1.3 Photonic glasses reflect light diffusely, and the color of reflected light does not depend on the orientation of the material. (a) Amorphous packing of silica spheres with diameter $\sim$ 250 nm. (b) A different amorphous packing, of polystyrene-poly(N-isopropylacrylamide) particles in water. The packing looks blue regardless of orientation. In the left side of (b) we show a picture taken at an angle close to the illumination axis, as illustrated in the left schematic of (c); and in the right side of (b) we show a picture taken at about 50° with respect to the illumination axis, as illustrated in the right schematic of (c). . . . 5

1.4 The relation between the wavelength reflected from a crystal and the angle of ϕ of incidence and reflection can be understood from geometry. (a) Schematic of a crystalline array of scatterers, positioned on planes a distance d apart, and illuminated at an angle ϕ with respect to the surface normal. For two waves to add up constructively, the optical pathlength difference, marked in red, has to be an integer multiple of the wavelength. (b) Top: Spherical waves emanating from three of the scatterers in (a). There are special directions, marked with the light blue lines, along which all wavefronts meet: these are areas of constructive interference. Bottom: representation of the actual waves as they might be seen on a two-dimensional surface, such as water. (c) Same as (b), but for a longer wavelength. The directions of constructive interference, marked with the orange line, are now different: they occur at a smaller angle with respect to the vertical axis. 8

1.5 Scattering from two particles. Left: two particles, at $\mathbf{x}_\mathrm{i}$ and $\mathbf{x}_\mathrm{j}$, are illuminated by light with wavevector $\mathbf{k}_\mathrm{in}$ and scatter light with wavevector $\mathbf{k}_\mathrm{s}$. The angle θ between $\mathbf{k}_\mathrm{in}$ and $\mathbf{k}_\mathrm{s}$ is the scattering angle, and the vector difference between the two wavevectors is $\mathbf{q} = \mathbf{k}_\mathrm{in} - \mathbf{k}_\mathrm{s}$. 10

1.6 Structure factor of a colloidal glass with volume fraction $\phi = 0.55$. The peaks denote the existence of characteristic lengthscales of periodicity. The first peak of the structure factor, at x_max, corresponds to the average spacing between coordination shells in the glass, $a = 2\pi d/x_\mathrm{max}$, shown schematically in the inset. 13

2.1 (a) Schematic of the system showing all components and refractive indices at 500 nm (PS: polystyrene, poly(NIPAM-*co*-AAc): poly(*N*-isopropylacrylamide-*co*-acrylic-acid), water). (b) Differential interference contrast micrograph of an amorphous aggregate of core-shell particles. The hydrodynamic diameter of the cores is 230 nm and that of the shells is 2100 nm (here the shells are compressed). (c) Schematic of the apparatus for spectral transmission measurements. Only one of the two rotation stages is shown. 19

2.2 (a) Confocal microscope images (left) and azimuthally-averaged, 2D spatial power spectra of the images (right) for an amorphous, dense suspension of core-shell particles with hydrodynamic core and shell diameter (δ, d) = (230 nm, 2500 nm). The inset on the right is the average of the power spectra of a z-stack of confocal images with depth 19 µm. (b) Same as (a), but for a suspension of core-shell particles with hydrodynamic core and shell diameter (δ, d) = (180 nm, 940 nm). The inset on the right is the power spectrum of the image on the left. The peaks in frequency space correspond to a characteristic length scale of 897 nm in (a) and 322 nm in (b). In both insets we have masked the values around zero wavevector and we have set a threshold to the dynamic range for better contrast. The bars correspond to 10 µm^{-1}. . 24

2.3 (a) Photographs of amorphous packings made from particles with various core and shell diameters, showing the range of appearances that can be produced. The field of view for each sample is 2 mm x 2 mm. (b),(c) Transmission spectra of two amorphous packings of core-shell particles with different shell diameters, at various angles. The hydrodynamic diameter of the shells is 430 nm in (b) and 640 nm in (c), and the diameter of the cores is 180 nm in both cases. The angles are measured between the axis of illumination-detection and the normal to the sample surface. Insets show photographs of samples with a 1 mm x 1 mm field of view. 25

2.4 (a) Azimuthal averages of the power spectra of a z-stack of confocal images taken for two amorphous aggregates of core-shell particles. The depth of the stack was 6 µm in both cases. The 2D power spectra are shown in the insets, where we have masked the values around zero wavevector and we have set a threshold to the dynamic range of the image for better contrast. The bars are 10 µm^{-1}. The hydrodynamic core and shell diameters are (δ, d) = (180 nm, 940 nm) for the upper green curve and (140 nm, 1400 nm for the lower blue curve. The samples have a peak in spatial frequency at 20.3 µm^{-1} (green) and 20.2 µm^{-1} (blue). (b) Transmission spectra through the samples shown in (a) as a function of wavelength (upper x-axis) and wavevector q (lower x-axis). The values for q were calculated using $n = 1.35$. The sample thickness was about 130 µm in both cases. Inset:$-\ln T/\sigma_s$ (see text). 26

2.5 Transmission spectra through core-shell suspensions in which (a) the particles have crystallized and (b) the particles have formed a disordered packing. Both samples were prepared using a depletion attraction. The crystalline sample was prepared from a monodisperse suspension of particles with hydrodynamic core and shell diameters (δ, d) = (180 nm, 430 nm), whereas the amorphous sample was prepared from a bidisperse suspension of particles with hydrodynamic core and shell diameters (δ, d) = (180 nm, 430 nm) and (180 nm, 640 nm). Insets show photographs of the samples with a 2 mm x 2 mm field of view. 29

3.1 Measured reflectivity spectra for three similarly-prepared colloidal glasses of poly(methyl methacrylate) particles in air. Insets show photographs of the samples and diameters of the particles used to make the samples. The purple sample would appear red if not for the high reflectivity in the blue, indicated by the arrow. 32

3.2 Scattering geometry for our model. 35

3.3 Structure factor of a colloidal glass with volume fraction $\phi = 0.55$ calculated from the Ornstein-Zernike equation under the Perkus-Yevick approximation. 36

3.4 Calculated reflectivity as a function of kd for a photonic glass of spheres at a volume fraction $\phi = 0.55$, as calculated from Equation 3.6 with the Fresnel reflection coefficient omitted. The vertical dashed lines denote the kd-values that correspond to the range of visible wavelengths we detect, 425 nm (blue line) and 800 nm (red line), when the particle size is $d = 334$ nm. 40

3.5 (a),(b) Measured (smooth lines) and calculated (dashed lines) reflection spectra of colloidal photonic glasses made of poly(methyl methacrylate) spheres. Theoretical spectra are calculated from Equation (3.6) with $\phi = 0.55$ and $l = 16$ μm. Particle diameters that best fit the measured peaks are 238 nm (a) and 334 nm (b), in good agreement with the measured particle diameters. (c) Calculated reflection spectrum for a photonic glass made from $d = 334$ nm particles, including only the structure factor (thick curve, divided by 10) and only the form factor (thin curve). 42

3.6 (a) Reflection spectra from Figure 3.1 plotted against the dimensionless lengthscale kd. Note the increased scattering at high kd-values (short wavelengths) for the $d = 330$ nm sample. (b) Same as (a) but normalized to the single-particle form factor integrated over the detected scattering angles, $\sigma_{F,\text{detected}}$, as defined in Eq. 3.7. The increased scattering at high kd-values disappears, indicating that it is due to the form factor. Differences in amplitude of the peaks are likely due to differences in the sample thickness l. 43

3.7 Resonant wavelengths of the backscattering cross-section, as calculated from Mie theory, as a function of optical diameter $n_\text{p}d$ for a refractive index contrast $m = 1.2$, which corresponds to that in our experimental system. The resonant wavelength follows the linear relation $\lambda = 2n_\text{p}d/z$ (solid lines), where z is the order of the resonance. Lines correspond to different values of z (top: $z = 1$, middle: $z = 2$, bottom: $z = 3$). 45

3.8 Single-particle differential scattering cross-sections for various scattering angles as a function of wavelength for a 330 nm PMMA sphere in a colloidal glass of spheres in air at a volume fraction $\phi = 0.55$. The blue-shift in the resonance is consistent with the decrease in optical pathlength inside the sphere with decreasing angle: The longest possible pathlength a is twice the diameter, and $a > b$ for any angle that differs from backscattering. 45

3.9 Calculated transport length as a function of wavelength for the green ($d = 238$ nm) and purple ($d = 334$ nm) photonic glasses of polymethylmethacrylate spheres, using a volume fraction $\phi = 0.55$, as calculated from Equation 3.6 with the Fresnel reflection coefficient omitted. The vertical dashed lines denote the kd-values that correspond to the range of visible wavelengths we detect, 425 nm (blue line on the right) and 800 nm (red line on the left), when the particle size is $d = 334$ nm. 48

3.10 We can use dispersion to partially index-match the scatterers and the medium and suppress scattering in the blue. (a) Dispersion curves for poly-methylmethacrylate and for a Cargille refractive index liquid with $n = 1.486$ at 589 nm. The indices of the two materials are very similiar at short wavelengths and deviate from each other at larger wavelengths. (b) Detection cross section for a glass of poly-methylmethacrylate particles in air and in the same oil as in (a). Because the poly-methylmethacrylate is almost index-matched to the oil at short wavelengths, scattering in that regime is suppressed. For comparison, we also show the reflectivity for a similar glass of particles are in air, divided by 200. In both calculations we use $\phi = 0.55$ and $l = 16\mu$m; the particle sizes are 238 nm for the system in oil and 278 nm for the system in air, chosen to yield a resonance at the same wavelength. 51

3.11 Calculated reflection for an inverse glass of core-shell spheres engineered to scatter most strongly in the red. The continuous red curve includes both the structure and the form factor, the dashed black curve only the structure factor (divided by 2), and the black continuous curve only the form factor. The vertical dashed line marks 425 nm, the low-wavelength limit in our spectral measurements. The optimal design has air cores with diameter 260 nm and silica shells with diameter 280 nm, and the particles are embedded in a silica matrix. The reflectivity peak at 632 nm is primarily due to the structure factor and determined by the shell diameter. One form-factor resonance occurs in the near-IR, boosting the structural resonance in the red, and another occurs deep in the ultra-violet (at about 150 nm), too far away from the visible regime to affect the color. 53

4.1 Fabrication of photonic pigments. a) Schematic of a capillary microfluidic device for the production of water-in-oil-in-water double-emulsion droplets with a thin ethoxylated trimethylolpropane triacrylate (ETPTA) membrane. b) Optical micrograph showing generation of uniform water-in-oil-in-water droplets. The innermost phase contains an aqueous suspension of coreshell particles with a volume fraction $\phi_{\text{coreshell}}) \sim 0.28$. c) Time-series optical micrographs of osmosis-driven condensation of droplets at 340 mOs/mL, where t_1, the elapsed time for microscope analysis, is about 5 minutes. d) Schematic of the structure of particles during osmosis-driven condensation. e,f) A photograph and an optical micrograph of the photonic pigments in water after UV-curing of the ETPTA shell. The sample is compressed at 440 mOs/mL. A few capsules show yellow spots due to local deformation of the polymer shell. g) Scanning electron micrograph of a cross-section of a cryogenically fractured photonic pigment microcapsule prepared under compression at 440 mOs/mL. The field of view is 20 μm wide. The inset in (g) is the two-dimensional Fourier power spectrum derived from (g), with a 220 μ^{-1}m field of view. 59

4.2 Control of structural colors through osmotic pressure. a) Reflectance spectra of the microcapsules equilibrated under different osmotic pressures. b) Plots of peak positions (dark squares) and normalized full-width at half maximum (FWHM; open circles) of the microcapsules as a function of osmotic pressure. c) Estimated concentration of PS scatterers (dark squares) and average spacing between PS scatterers (open circles) as a function of osmotic pressure. Insets are bright-field (reflection) optical micrographs of red, yellow, and green microcapsules prepared under 180 mOsm/L, 260 mOsm/L, and 440 mOsm/L, respectively. The field of view for the insets is 100 μm wide. d) Co-polarization (lines) and cross-polarization (dots) reflection spectra of red (upper) and green (lower) photonic microcapsules. 61

4.3 A schematic illustration of our spectrometry setup for measuring the co-polarized and cross-polarized reflection spectra of the photonic microcapsules. 64

4.4 Photonic microcapsules with blue, green, and red structural colors prepared with different shell thicknesses of coreshell particles. a) Bright-field (reflection) and b) dark-field (reflection) optical micrographs of photonic microcapsules. c) Reflectance spectra of the microcapsules. All droplets are incubated at 440 mOsm/L for one hour before ETPTA polymerization. 66

4.5 Photonic microcapsules show uniform structural colors under different illumination directions. Bright-field (reflection) optical micrographs of (a) photonic microcapsules and (b) crystalline balls. (c) Schematic of the apparatus used to measure the reflection spectra of a single microcapsule or ball. (d,e) Reflectivity (yellow: 100%, blue: 0%) of a microcapsule (d) and a crystalline ball (e) as a function of position (x), where x=0 at the center and x=1 at the edge. 68

4.6 (a) Reflectance spectra of the photonic pigments at various viewing angles. (b) Peak position ($\lambda_{\max}$, dark squares) and normalized full-width at half-maximum ($\Delta\lambda/\lambda_{\max}$, open circles) of each peak at various angles. In this measurement we varied the angles of the sample stage with respect to the normal to the substrate. 69

5.1 There is an optimal value for the refractive index contrast, $m \sim 0.7$, for which the resonances of the structure factor dominate scattering. (a) Reflection cross section as a function of kd, for various values of m, including both the form and the structure factor, (b) only the form factor, (c) only the structure factor. By inspection, we see that, in the full calculation shown in (a), the resonance at $x =\sim 4.8$ comes from the first resonance of the structure factor, while the resonances at higher x come from a combination of resonances of the structure and of the form factor. The vertical dashed blue line corresponds to 400 nm if the resonance of the structure factor is at 650 nm, chosen for red color. For comparison, we also show the curves for $m = 1.2$, corresponding to a typical glass of colloidal particles. 74

5.2 Inverse glasses made of colloidal particles immersed in high-index oils can have weak, red structural color; however their spectra have short-wavelength features that our model does not predict. (a) Reflection spectrum of a glass of PMMA particles with diameter $d = 240$ nm, infiltrated with an oil of refractive index $n_{\text{medium}} = 1.6$ (shown in the inset). (b) Reflection spectrum of a glass of silica particles with diameter $d = 250$ nm, before and after infiltration with an oil of refractive index $n_{\text{medium}} = 1.486$ (shown in the inset). (c) Calculated cross section for the system in (a) for near backscattering, with $170 < \theta < 180$ degrees. The cross section has a peak that matches the data for $d = 246$ nm, but no other peak at shorter wavelengths. (d) Calculated cross-section for the system in (b) for near backscattering, with $170 < \theta < 180$ degrees, before and after inflitration. The peaks of the cross sections match the data for $d = 242$ nm, but, again, our theory does not predict another visible peak at short wavelengths. 77

5.3 Our calcination method for making inverse glasses is succesful in yielding glassy packings of air spheres, with short-range order and long range disorder; SEM images courtesy of Nicolas Vogel. 79

5.4 The volume fraction can exceed the random close packing limit of $\phi_{\mathrm{rcp}} = 0.65$ in a random packing of spheres that are allowed to overlap, as is the case in our samples (see inset). Here the overlap is defined as the difference between the distance of the centers of touching particles and the sum of their radii. Volume fraction (x axis) versus average overlap (y-axis) in simulated glassy packings of spheres with bidispersity 1:1.2. For each volume fraction there are 100 different realizations of packings. The error bars are the standard deviation of overlaps within a single packing. Simulation courtesy of Zorana Zeravcic. . . . 86

6.1 The sRGB values calculated from the measured reflection spectra of our colloidal glasses agree reasonably well with the appearance of the samples. Left column: sRGB colors calculated with ColorPy. Right column: pictures of colloidal glasses made with poly-methylmethacrylate particles. 95

6.2 Our model predicts that colloidal glasses can produce a wide range of structural colors. Calculated sRGB colorsfor colloidal glasses of core-shell particles as a function of core and shell diameter. We used a thickness of 15μm and a volume fraction $\phi = 0.5$, and we have index-matched the shells to the medium. (a) Air-silica core-shell particles in silica. The colors are primarily determined by the shell diameter, indicating that the form factor does not have strong features in the visible. (b) Polystyrene scatterers in water. (c) Silica scatterers (n=1.4) suspended in air. In (b) and (c), the range of colors is fairly wide and the hue can be tuned with both the shell and the core diameter. (d) Titania cores in silica. While the refractive index contrast here is the same as in (c), the range and saturation of colors is limited. 99

Prior Publications

This thesis is largely based on the following publications:

- Chapter 2: Sofia Magkiriadou, Jin-Gyu Park, Young-Seok Kim, and Vinothan N. Manoharan, "Disordered packings of core-shell particles with angle-independent structural colors." *Optical Materials Express* **2**(10), 1343–1352 (2012).

- Chapter 4: Jin-Gyu Park, Shin-Hyun Kim, Sofia Magkiriadou, Tae Min Choi, Young-Seok Kim, and Vinothan N. Manoharan, "Full-spectrum photonic pigments with non-iridescent structural colors through colloidal assembly." *Angewandte Chemie* **126**(11), 2943–2947 (2014).

- Chapter 3: Sofia Magkiriadou, Jin-Gyu Park, Young-Seok Kim, and Vinothan N. Manoharan, "Absence of red structural color in photonic glasses, bird feathers, and certain beetles." *Physical Review E* **90**, 062302 (2014).

The author has also contributed to:

- W. Benjamin Rogers, Madeleine Corbett, Sofia Magkiriadou, Philippe Guarillof, and Vinothan N. Manoharan, "Breaking trade-offs between translucency and diffusion in particle-doped films." *Optical Materials Express* **4**(12), 2621–2631 (2014).

Acknowledgments

Where to begin! Graduate school has been a learning experience in science and beyond, and I am lucky to have encountered many people along the way who taught me not only with their knowledge, but also with their wisdom.

First and foremost, I am thankful to my research advisor, Vinny Manoharan. I think one of the most important things I have learned while working with Vinny is to loose fear of doing things that I do not know how to do. Moreover, I have learned from his methodical ways and from his high standards of writing papers and giving presentations.

I cannot imagine how any of this work would have been done without Jin-Gyu Park. Jin-Gyu is not only an excellent chemist that can produce a variety of colloidal particles upon request, but also an insightful conversationalist with questions that make me think hard.

My first experiments on structural colors were based on the work of Jason Forster and Eric Dufresne. They both welcomed me warmly into the field and shared all that they knew; I am grateful for all the support that I received from them. Also a Yalie, Rick Prum, who first understood that the feathers of blue birds are structurally colored, has always been excited to exchange biology for physics facts; it has been very interesting to learn about structural colors from his point of view.

When I joined the Manoharan group, I had the luck to be surrounded by the experimental genius of Dave Kaz. Not only did I thoroughly enjoy our conversations about machining, but also I learned that it is possible to make a high-quality working apparatus from unlikely parts. Of the same generation was Ryan McGorthy, who helped me gradually feel at home in the wet lab - starting with teaching me how to

pipette. For my initiation to microscopy, I have to thank Guangnan Meng. Guangnan was also my deskmate for many months, during which he developed the ability to sense when I was confused without even looking at me; this prompted many good conversations, on science and on life.

On my other side sat for many months Becca Perry, who always has an ear available for trouble-shooting and who has actively shown her support from the day I joined the group. Becca and Tom Dimiduk have been my invaluable resources for questions related to programming. Ben Rogers has taught me a lot with his clear way of thinking and infallible sense of perspective. Nick Schade has been my default resource for all the basic physics I should already know; a great consultant for preparing talks; and a reliable source of good spirits.

Beautiful colloidal particles and great suggestions for experiments came from Tom Kodger and Rodrigo Guerra, both of the Weitz group. Young-Seok Kim, from the Korea Electronics Technology Institute; Prof. Gi-Ra Yi, from Sungkyunkwan University; and Shin-Hyun Kim, now a professor at the Korea Advanced Institute of Science and Technology, have also contributed significantly to this work, with materials and with ideas.

Nicolas Vogel, now a professor at the University of Erlangen-Nürnberg, was integral in our experiments on inverse glasses and an enthusiastic lab companion. Mathias Kolle offered a lot of advice on spectrometry techniques.

It was very fun and instructive to teach electronics lab with Tom Hayes, and an honor to know Stan Cotreau and have taken his machine shop class.

Melissa Franklin, Jacob Barandes, and Jim McArthur were generous with their

wise words throughout graduate school.

I am grateful to Elise Novitski for her constant support during this time, and for proof-reading this thesis.

Finally, I would probably be somewhere else, thousands of miles away from here, if it were not for my family's invincible and contageous optimism.

Chapter 1

Introduction

Light has a dual nature: particle and wave. In many situations, light-matter interactions can be likened to systems of balls bouncing from interfaces. However, there are also phenomena that cannot be explained without evoking wave mechanics and in particular interference.

Most of what we see around us is visible via a ballistic process, namely reflection. If a surface is very smooth, such as a mirror or a calm sea, it simply deflects light rays that are incident upon it at an angle equal to the angle that it received them, thus appearing very bright from certain points of view. If a surface is rough, such as wood or most fabric, it similarly deflects light rays at an angle equal to the angle of incidence, except in this case there is a different angle of incidence for each sub-surface and hence a wide range of angles over which the reflected intensity is distributed. This gives rise to a matte appearance.

However, since light is also a wave, it has an inherent lengthscale: a wavelength. If the roughness of a material occurs at this lengthscale the phenomenology of light-

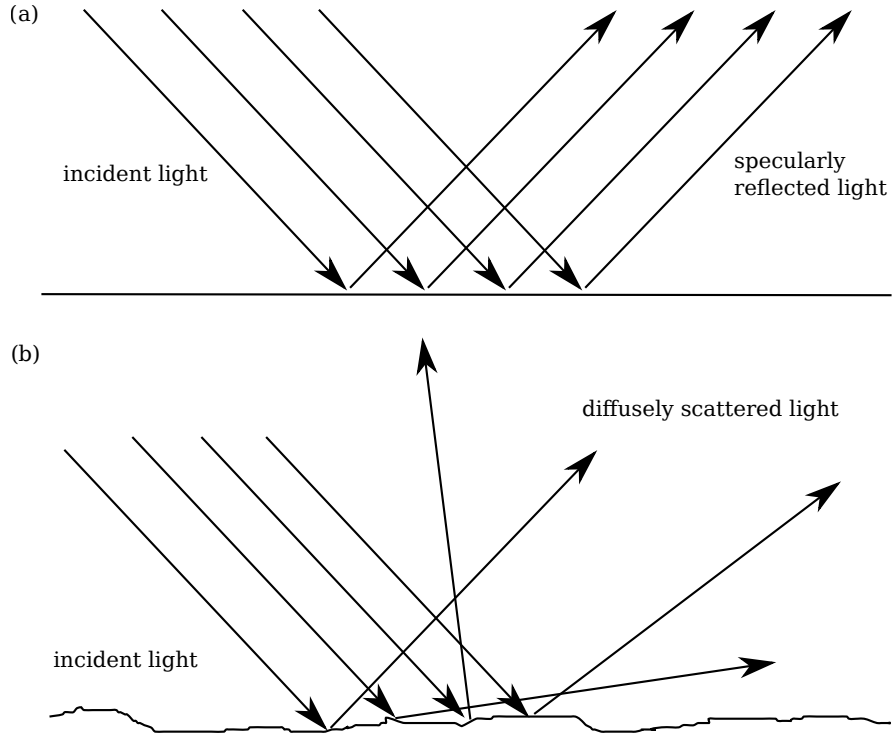

Figure 1.1: (a) A flat surface reflects light specularly. (b) A rough surface reflects light specularly on each of its microsurfaces; overall, light is scattered in many directions, diffusely.

matter interactions changes dramatically. For example, a material with periodically arranged inhomogeneities, such as the one shown in Figure 1.2, can reflect light specularly like a completely smooth surface, but only for specific wavelengths that depend on the angle of illumination. This gives rise to a metallic and iridescent appearance. Other materials, such as the one shown in Figure 1.3, have randomly arranged inhomogeneities at the wavelength scale. Most of these appear white, but some of them can have a matte colored appearance, depending on the type of disorder in their internal structure. It is this special class of *disordered materials with angle-independent structural colors* that have inspired this thesis.

1.1 Scattering from Photonic Materials

To understand the behavior of these materials, often called *photonic materials*, it is useful to treat each scattering point as a point-source. In this picture, the light scattered from each point is a spherical wave, and the total scattered field can be described as a the sum of all the spherical waves radiating from each point.

1.1.1 Photonic Crystals

Before we apply this approach to the study of materials with random internal structure, it is instructive to think about materials with crystalline order at the wavelength scale, otherwise called *photonic crystals*. In Figure 1.4(a) we show schematically such a periodic arrangement of scatterers and in Figures 1.4(b),(c) we show spherical waves emanating from some of the scatterers (we have omitted the others for simplicity). Figure 1.4(c) shows a wave with longer wavelength than Figures 1.4(b).

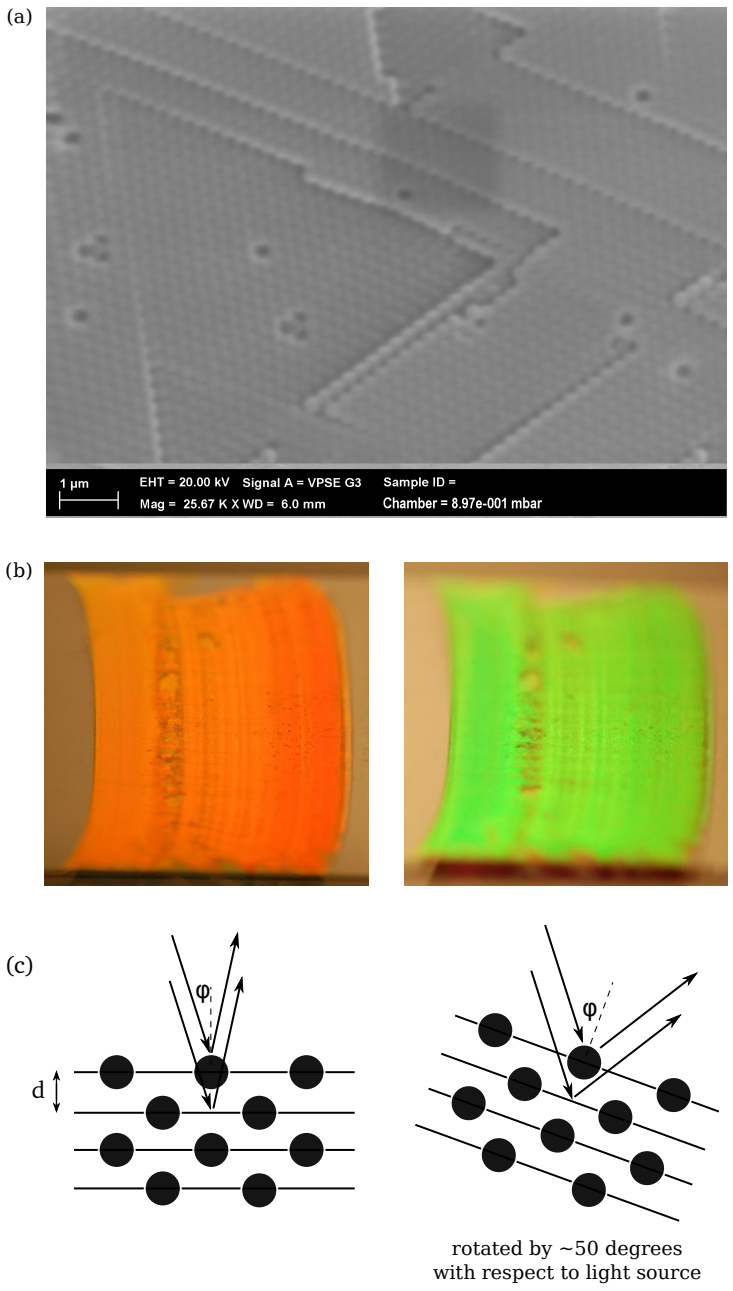

Figure 1.2: Photonic crystals reflect light specularly, and the color of reflected light depends on the orientation of the material. (a) Crystalline packing of polystyrene spheres with diameter $\sim$ 230 nm. (b) The packing shown in (a) looks bright orange when viewed at an angle close to the illumination axis, as shown in the left schematic of (c). The same packing looks bright green when viewed at about 50° with respect to the illumination axis, as shown in the right schematic of (c).

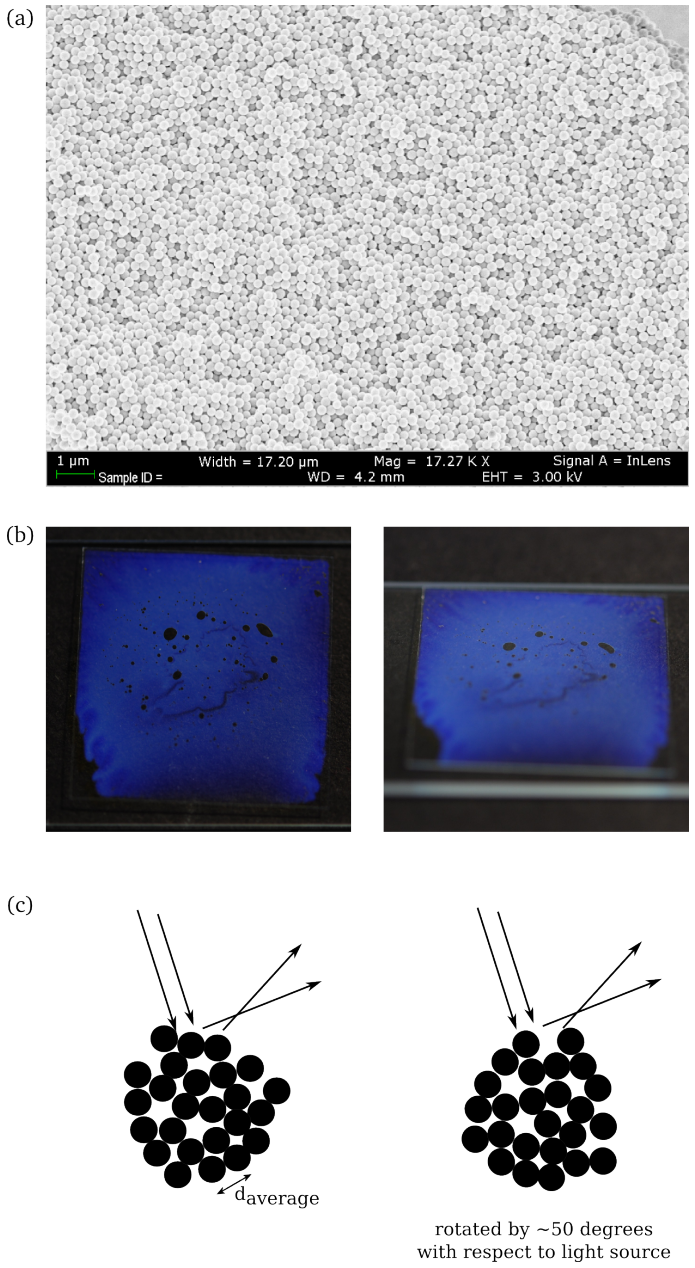

Figure 1.3: Photonic glasses reflect light diffusely, and the color of reflected light does not depend on the orientation of the material. (a) Amorphous packing of silica spheres with diameter ~ 250 nm. (b) A different amorphous packing, of polystyrene-poly(N-isopropylacrylamide) particles in water. The packing looks blue regardless of orientation. In the left side of (b) we show a picture taken at an angle close to the illumination axis, as illustrated in the left schematic of (c); and in the right side of (b) we show a picture taken at about 50° with respect to the illumination axis, as illustrated in the right schematic of (c).

We see that, for each wavelength there are special directions of propagation along which the wavefronts meet and add up constructively. This means that if light of a certain wavelength is incident on a crystal along one of these special directions, it can be scattered into another one of these directions; but if the incoming light is incident on a crystal along a direction that is far from one of the special directions, there will be no reflected light at that wavelength. Note that here we have drawn the waves radiating from each point as all being in phase. This is not generally true: the interference pattern will shift depending on the relative phases of the spherical waves, and these phases in turn depend on the phase of the incident wave as it reaches each point. In any case, the relation between wavelength and angle can be calculated from geometry, if we consider the relative phase differences between scattered waves that reach an observer far from the material. For maximum constructive interference to occur, the relative phase difference between any two waves must be an integer multiple of 2π. As shown in Figure 1.4(a), given a lattice spacing d and an angle of incidence ϕ with respect to the surface normal, this condition can only be satisfied at specific wavelengths given by the following expression:

$$\lambda = 2d\cos(\phi)/z \tag{1.1}$$

where λ is the wavelength of light *inside* the material, related to the wavelength of light in vacuum via the refractive index of the material n ($\lambda = \lambda_{vacuum}/n$), and z is an integer. Changing the angle of incidence results in a change of the resonant wavelength: this phenomenon is familiar from opal gem stones and is colloquially described as iridescence (see Figure 1.2), or *angle-dependent structural color* – where "structural" refers to the fact that the color arises from the structural configuration of

the material and does not require the existence of an absorbing dye. This description of scattering from a crystal is known as the *von Laue* picture; it is equivalent to a description that treats crystals as arrays of scattering planes, known as the *Bragg* picture.

1.1.2 Photonic Glasses

However, this thesis is concerned with disordered photonic materials, and in particular *photonic glasses*: dense and random assemblies of particles that, despite their disordered nature, can also scatter resonantly at specific wavelengths [1, 2]. As we show in Figure 1.3, photonic glasses can have angle-*in*dependent structural colors. How can we understand the origin of these colors?

The Fourier Transform and Scattering

When it comes to disordered materials, it is much more difficult to draw a clean picture of scattering and make geometric arguments about whether or not there should be scattering resonances. Instead, it can be more helpful to step away from real space and into momentum space. The two spaces are related via the Fourier transform; any well-behaved function f [1] that is known in real space (x-space) can be projected onto a dual q-space via

$$f(\mathbf{q}) = \int_{-\infty}^{\infty} e^{-i\mathbf{qx}} f(\mathbf{x}) d\mathbf{x}. \tag{1.2}$$

[1] By 'well-behaved' here we mean a function that is single-valued, has a finite number of maxima and minima, a finite number of discontinuities, and a finite integral, as imposed by Dirichlet's theorem [3].

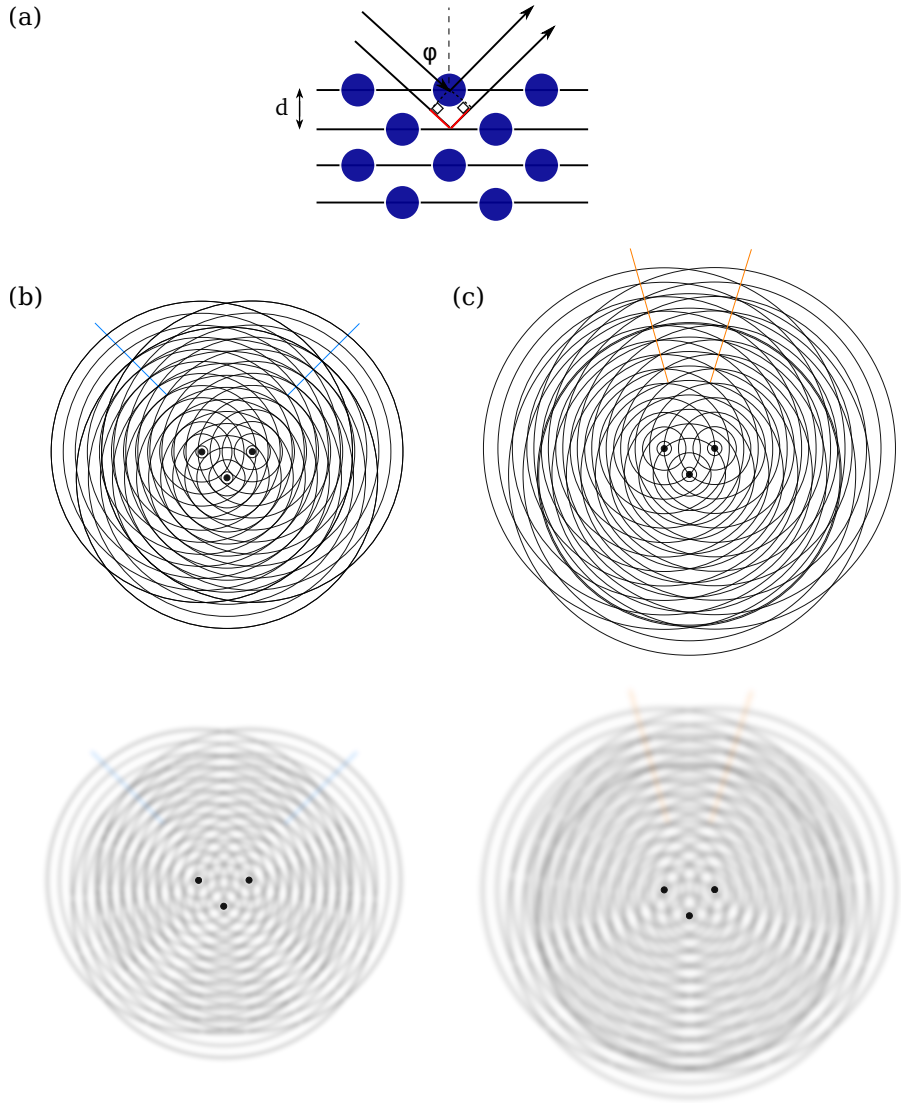

Figure 1.4: The relation between the wavelength reflected from a crystal and the angle of ϕ of incidence and reflection can be understood from geometry. (a) Schematic of a crystalline array of scatterers, positioned on planes a distance d apart, and illuminated at an angle ϕ with respect to the surface normal. For two waves to add up constructively, the optical pathlength difference, marked in red, has to be an integer multiple of the wavelength. (b) Top: Spherical waves emanating from three of the scatterers in (a). There are special directions, marked with the light blue lines, along which all wavefronts meet: these are areas of constructive interference. Bottom: representation of the actual waves as they might be seen on a two-dimensional surface, such as water. (c) Same as (b), but for a longer wavelength. The directions of constructive interference, marked with the orange line, are now different: they occur at a smaller angle with respect to the vertical axis.

For a discrete function we can use the discrete Fourier transform:

$$f(\mathbf{q}) = \sum_i e^{-i\mathbf{q}\mathbf{x}_\mathrm{i}} f(\mathbf{x}_\mathrm{i}). \tag{1.3}$$

The Fourier transform is very convenient for identifying periodic features: if a function has a periodicity x_o, say in real space, its Fourier transform has a peak at a corresponding spatial frequency $q_\mathrm{o} = 2\pi/x_\mathrm{o}$. Moreover, the width of this peak contains information about the spatial extent of periodicity: if a function is periodic over a long range in x-space, its spatial period is well-defined and the corresponding peak in q-space is narrow; whereas if a function is only periodic over a short range in x-space, its spatial period cannot be well defined and the corresponding peak in q-space has a width that is inversely proportional to the range where it is periodic.

The reason why this – perhaps counter-intuitive – representation is convenient for describing scattering goes back to the depiction of scattered light as the sum of spherical waves radiating from every scattering point. In what follows, we explain this connection.

The electromagnetic field E of a spherical wave at $\mathbf{x}$ radiating outwards from $\mathbf{x}_\mathrm{o}$ through a medium with refractive index n is described by

$$E(\mathbf{x}) = E_\mathrm{o} e^{-i\mathbf{k}\cdot(\mathbf{x}-\mathbf{x}_\mathrm{o})} \frac{(\mathbf{x}-\mathbf{x}_\mathrm{o})}{|\mathbf{x}-\mathbf{x}_\mathrm{o}|^2} \tag{1.4}$$

where $E_\mathrm{o}(\mathbf{x})$ is field amplitude at $\mathbf{x}$, $\mathbf{k}$ is the wavevector, with magnitude that is related to the wavelength via $|\mathbf{k}| = 2\pi n/\lambda$, $\mathbf{x}$ is the location of observation and $\mathbf{x}_\mathrm{o}$ is the origin of the wave.

Consider now a pair of identical scatterers at $\mathbf{x}_\mathrm{i}$, $\mathbf{x}_\mathrm{j}$ illuminated by light with wavevector $\mathbf{k}_\mathrm{in}$, as shown in Figure 1.5. In the picture we presented above, each

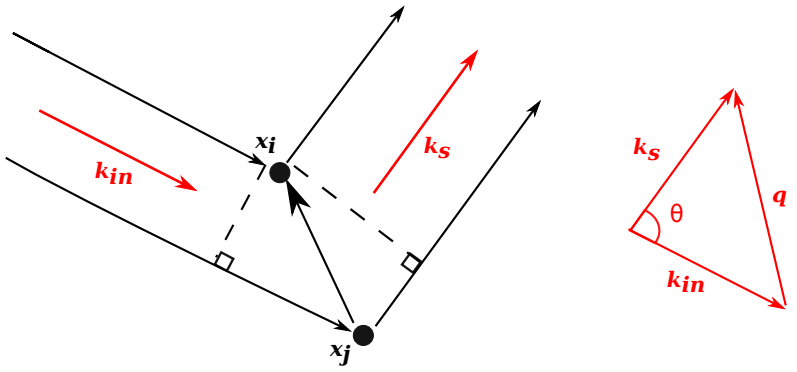

Figure 1.5: Scattering from two particles. Left: two particles, at $\mathbf{x}_\mathrm{i}$ and $\mathbf{x}_\mathrm{j}$, are illuminated by light with wavevector $\mathbf{k}_\mathrm{in}$ and scatter light with wavevector $\mathbf{k}_\mathrm{s}$. The angle θ between $\mathbf{k}_\mathrm{in}$ and $\mathbf{k}_\mathrm{s}$ is the scattering angle, and the vector difference between the two wavevectors is $\mathbf{q} = \mathbf{k}_\mathrm{in} - \mathbf{k}_\mathrm{s}$.

scatterer will radiate its own spherical wave in response to this field. Two waves radiating from points $\mathbf{x}_\mathrm{i}$, $\mathbf{x}_\mathrm{j}$ will generally differ in phase by

$$\Delta\phi_{\mathrm{i,j}} = \mathbf{k}_\mathrm{s} \cdot (\mathbf{x}_\mathrm{j} - \mathbf{x}_\mathrm{i}) - \mathbf{k}_\mathrm{in} \cdot (\mathbf{x}_\mathrm{j} - \mathbf{x}_\mathrm{i}) \equiv \mathbf{q} \cdot (\mathbf{x}_\mathrm{j} - \mathbf{x}_\mathrm{i}) \tag{1.5}$$

where $\mathbf{q} \equiv \mathbf{k}_\mathrm{s} - \mathbf{k}_\mathrm{in}$ is the momentum change between the incident and the scattered wave. To calculate the total scattered field at $\mathbf{x}$ from an ensemble of scatterers, we can simply add all the spherical waves originating from all points $\mathbf{x}_\mathrm{i}$, taking special care to account for their phases: $E_\mathrm{total}(\mathbf{x}) = E_\mathrm{o} \sum_i f_\mathrm{i} e^{-i\phi_\mathrm{i}} \frac{(\mathbf{x}-\mathbf{x}_\mathrm{i})}{|\mathbf{x}-\mathbf{x}_\mathrm{i}|^2}$. Here f_i is a quantity that describes the scattering properties of particle i, also known as its *form factor* and related to the *scattering cross section* as we will discuss in Chapter 3; and ϕ_i is the phase of the field scattered by particle i. Assuming identical scatterers, and that we are far enough from the material such that $|\mathbf{x} - \mathbf{x}_\mathrm{i}| \sim |\mathbf{x}|$, this expression can be simplified to

$$E_\mathrm{total}(\mathbf{x}) = \frac{E_\mathrm{o} f}{|\mathbf{x}|^2} \hat{x} \sum_i e^{-i\phi_\mathrm{i}} \tag{1.6}$$

The similarity of this expression to Equation 1.3 is already suggestive of the relevance of the Fourier transform for scattering.

However, in most experiments it is the light intensity that we measure, not the field. To obtain an expression for the intensity, we simply square Equation 1.6: $I_{\text{total}}(\mathbf{x}) = \frac{I_o|f|^2}{|\mathbf{x}|^2}\sum_{i,j} e^{-i(\phi_j-\phi_i)}$ where $I_{\text{total}} = |E_{\text{total}}|^2$. The phase difference is given in Equation 1.5, so we finally arrive at

$$I_{\text{total}}(\mathbf{x}) = \frac{I_o\,|f|^2}{|\mathbf{x}|^2}\sum_{i,j} e^{-i\mathbf{q}\cdot(\mathbf{x}_j-\mathbf{x}_i)}. \tag{1.7}$$

Equation 1.7 has all the information we need to describe scattering from an arbitrary ensemble of identical scatterers, neatly divided into two parts: the part outside the sum only includes information about the scattering properties of the particles via the form factor, f, and the sum itself only includes information about the arrangement of particles in space. This term is aptly called the structure factor, S:

$$S(\mathbf{q}) = \frac{1}{N}\sum_{i,j} e^{-i\mathbf{q}\cdot(\mathbf{x}_j-\mathbf{x}_i)}. \tag{1.8}$$

The structure factor is related to the Fourier transform of the radial distribution function $g(\mathbf{x})$, which describes the density of particles a distance $\mathbf{x}$ from a particle in the ensemble: $S(\mathbf{q}) = 1 + n\int g(\mathbf{x})e^{i\mathbf{q}\cdot\mathbf{x}}d\mathbf{x}$, with n being the particle density [4]. Thus, as promised, we see that the q-space representation of a collection of particles is very convenient for extracting information about the scattered field.

Equation 1.7 suggests that if the structure factor has a peak for a certain $\mathbf{q}$ –corresponding to a spatial period $a = 2\pi/|\mathbf{q}|$ in the direction perpendicular to $\mathbf{q}$– there will also be a scattering peak. To identify the wavelength at which this resonance

will occur, we need simply notice from Figure 1.5 that, since $|\mathbf{k}_{\text{in}}| = |\mathbf{k}_{\text{s}}| \equiv k$,

$$q = 2k \sin(\theta/2). \tag{1.9}$$

Hence, we can relate each lengthscale of periodicity in the structure, a, to a combination of a wavelength and an angle:

$$\lambda = \frac{4\pi n}{q_{\text{o}}} \sin(\theta/2) = 2na \sin(\theta/2). \tag{1.10}$$

This, by the way, is identically Equation 1.1 for $d = a$, since $\theta = \pi - 2\phi$.

1.1.3 Photonic Glasses in Fourier Space and their Scattering Properties

However, the point of this exercise was to develop a formalism for understanding scattering from glassy structures. So what does a colloidal glass look like in q-space? The answer to this question is shown in Figure 1.6, where we plot the structure factor for a glass of hard spheres with diameter d at a volume fraction $\phi = 0.55$ as a function of a dimensionless variable qd (for the the analytic form of S, see Appendix B).

We see that the structure factor has several well-defined peaks at various q_{n}. From Fourier theory, we know that this signals the existence of lengthscales of periodicity $x_{\text{n}} = 2\pi/q_{\text{n}}$. Moreover, the peaks of the structure factor have a finite, non-zero width, indicating that order in glasses is short-ranged. This coexistence of order and disorder at different lengthscales is essential for angle-independent structural color: the short-range order ensures the existence of a resonance, and the long-range disorder ensures that the resonance condition is independent of the orientation of the material.

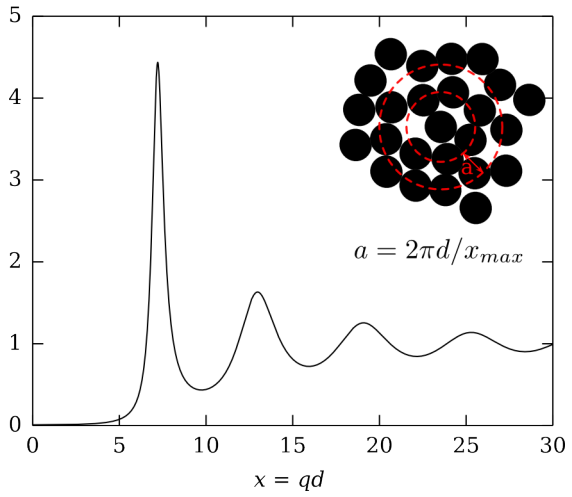

Figure 1.6: Structure factor of a colloidal glass with volume fraction $\phi = 0.55$. The peaks denote the existence of characteristic lengthscales of periodicity. The first peak of the structure factor, at $x_{\max}$, corresponds to the average spacing between coordination shells in the glass, $a = 2\pi d/x_{\max}$, shown schematically in the inset.

The lengthscales of order, x_{o}, describe correlations in the positions of neighboring particles. In this study we are primarily concerned with the first peak of the structure factor, which corresponds to the average spacing between coordination shells in a glass: the distance between consecutive particle layers around a central particle, drawn schematically in the inset of Figure 1.6. We will occasionally encounter the second peak. In our theoretical calculations, we use the analytic form of the structure factor included in Appendix B. To understand the connection between structure and scattering in experiments, we image our structures and from these images we calculate a proxy to the structure factor: the power spectrum, namely the squared absolute value of the Fourier transform of the image.

1.2 Previous Work on Photonic Glasses

Photonic glasses have likely existed for a very long time. The first report of angle-independent structural color from a glass structure came in 1998 from Prum et al [5], who discovered that photonic glasses give rise to the blue color of the feathers of the plum-throated cotinga. In this case the colloidal structures are composed of air bubbles in a matrix of β-keratin. Since then, similar structures have been discovered in hundreds of species, most of them avian [6, 7], but also in mammals [8] and mollusks [9]. In some cases, the underlying structure is a tortuous network of air channels in β-keratin [10], however some of the basic properties that affect scattering are the same: there is a characteristic lengthscale of short-range order, and long-range disorder. The term *Photonic glass* first appeared in the literature in 2000 by Ballato [1], who suggested they could be interesting photonic materials.

Since then, light transport through amorphous particle packings has been studied extensively. It has been shown that the short-ranged order can lead to enhanced backscattering [2, 11, 12, 13] and to resonances in the diffuse transmission and energy velocity of light [14]. Noh et al performed angularly-resolved measurements and observed that the structural colors of the photonic glasses found in bird feathers are independent of the angle of incidence and uniform under omni-directional illumination, but they depend on the angle between illumination and observation according to equation 3.1[15]. Based on biomimetic analogues made of bidisperse aggregates of polystyrene spheres, Forster et al showed the importance of another lengthscale, the sample thickness: by adding carbon black as an absorber, they restricted multiple scattering from the long-range disorder, and so they controlled the color saturation

[16]. Simultaneously with Forster et al, Harun-Ur-Rashid et al created bidisperse glassy packings of silica spheres and varied their colors by changing the ratio of the two components and thus the average inter-particle spacing [17]. In a different manifestation of the same principles, Ueno et al created liquid photonic glasses of polymer-grafted silica particles in an ionic liquid [18, 19].

In addition to fundamental studies, the potential of photonic glasses as a novel type of pigment has inspired a lot of research aimed at practical applications. Colloidal amorphous arrays have been used as ink for painting [20] and in colorful hydrophobic films [21], and glassy structures that respond to external stimuli have been proposed as sensors and as candidates for tunable electronic ink in reflective displays [22, 23, 24].

1.3 Overview

In this thesis we are primarily concerned with the color of photonic glasses. Our intention is to further understand and control the parameters that affect the structural color of colloidal glasses, with the aim to create highly saturated, angle-independent structural colors that cover the visible spectrum. We place particular emphasis on the study of long-wavelength colors, which, as we discuss, have been especially challenging to create and, to our knowledge, non-existent in nature. To that end, we explore novel colloidal systems with additional degrees of freedom; we show, experimentally and theoretically, the importance for color of an additional scattering process that has not been appreciated previously, namely resonant scattering within the colloidal particles; we suggest design rules for the creation of colloidal photonic glasses with optimal color saturation across the visible spectrum; and we report on our progress

towards this goal with experiments on a novel category of photonic glasses, *inverse* glasses, that we expect can have vivid red color.

Chapter 2

Disordered Packings of Core-Shell Particles with Angle-Independent Structural Colors

2.1 Introduction

Colloidal photonic glasses are most commonly made by randomly packing spherical colloidal particles at high density [16, 17, 20]. In these systems the lengthscale that characterizes the short-range order and determines structural color is the particle diameter. This parameter, however, also affects the scattering cross section of the particles and thus the intensity of scattered light of their assembly. In other words, in a system of densely packed hard spheres it is impossible to control structural color independently of color saturation: both are directly dependent on the particle size.

To allow decoupling of color hue from color saturation, we synthesized colloidal

particles with optical properties and packing characteristics designed so that the scattering can be controlled independently of the correlations. These particles consist of a hard, polystyrene core and a soft, poly(*N*-isopropylacrylamide-*co*-acrylic-acid) (poly(NIPAM-*co*-AAc)) shell. Unlike other types of core-shell particles used in optical studies [25, 18, 26, 27], the shells of our particles are transparent because they are index-matched to the solvent. The scattering is therefore dominated by the core and is decoupled from the particle size [28]. In dense samples, the scattering cross-section and form factor can be varied independently of the interparticle distance and structure factor; this is not possible in materials made from packed solid particles. As we show, the decoupling allows the wavelength of the structural color to be controlled independently of the transparency and saturation.

At the same time, the softness of the shells facilitates the assembly of disordered structures [29] that show angle-independent structural color. Much as in systems with highly-charged particles [2, 30], glassy structures can be made simply by concentrating the soft particles (Figure 2.1). The principal advantage of a soft steric interaction over a soft, long-range electrostatic interaction is that it obviates the need for long electrostatic screening lengths, which can be difficult to create and maintain in a colloidal suspension.

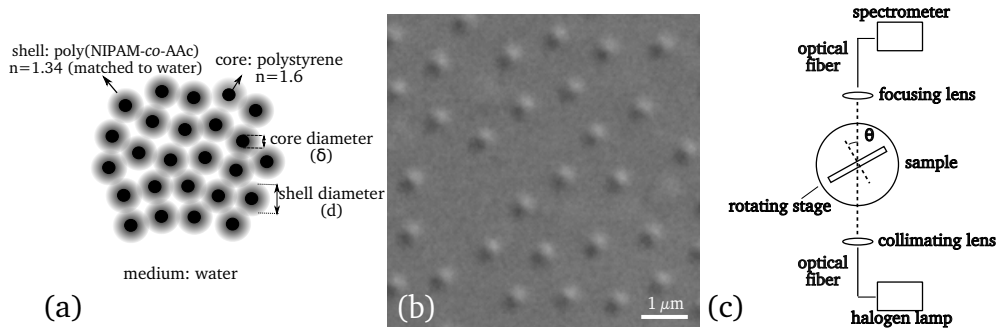

Figure 2.1: (a) Schematic of the system showing all components and refractive indices at 500 nm (PS: polystyrene, poly(NIPAM-*co*-AAc): poly(*N*-isopropylacrylamide-*co*-acrylic-acid), water). (b) Differential interference contrast micrograph of an amorphous aggregate of core-shell particles. The hydrodynamic diameter of the cores is 230 nm and that of the shells is 2100 nm (here the shells are compressed). (c) Schematic of the apparatus for spectral transmission measurements. Only one of the two rotation stages is shown.

2.2 Experimental Details

2.2.1 Synthesis and Characterization of Core-Shell Particles

Our particles consist of a polystyrene core ($n_{\mathrm{PS}} = 1.6$) and a poly(*N*-isopropylacrylamide-*co*-acrylic-acid) shell with refractive index matched to that of the surrounding water ($n_{\mathrm{water}} = 1.34$ at 500 nm). The particles were prepared by a two-stage emulsion polymerization process that allows independent control of the core and shell sizes [28]. All materials were used as received.

In a typical procedure for the core synthesis, 0.38 g of sodium dodecyl sulfate (SDS, 99%, J.T.Baker) and 3.75 g of *N*-isopropylacrylamide (NIPAM, 97%, Aldrich) were dissolved in 262.5 mL of Milli-Q-grade deionized water (Millipore, 18.2 MΩ-cm) in a 500 mL three-necked round-bottom flask equipped with a reflux condenser, a nitrogen inlet and a mechanical stirrer. Then 71.25 mL of styrene (99%, Alfa Aesar) were added under vigorous stirring. After the mixture was heated to 80 °C, 180 mg

of potassium persulfate (KPS, 99%, Acros) dissolved in 7.5 mL of deionized water were added. The reaction ran for 8 hours. The resulting polystyrene particles were dialyzed against deionized water for five days; the water was changed every two hours on the first day of dialysis and every twelve hours during the subsequent four days. The particle diameter was controlled by varying the amount of SDS, which sets the initial number of nuclei [31, 32].

To cover the polystyrene particles with shells, we first mixed 5.73 g of NIPAM, 0.03 g of *N,N'*-methylenebisacrylamide (MBA, molecular biology grade, Promega), 0.23 mL of acrylic acid (AAc, 99%, Sigma), and 30 mL of polystyrene latex at 20% w/w in a reaction vessel identical to that used in the core synthesis. The mixture was heated under stirring to 80 °C, and 0.222 g of KPS dissolved in 5 mL of deionized water were then added to start the reaction. The reaction ran for 3 hours. The resulting core-shell particles were dialyzed against deionized water for two days; the water was changed every two hours during the first day and every twelve hours during the second day. The thickness of the resulting poly(NIPAM-*co*-AAc) shells was controlled by varying the volume ratio of the monomer solution to the polystyrene seed particles [28].

We measured the hydrodynamic diameter of the synthesized particles with a dynamic light scattering apparatus (ALV SP-125) and a 532 nm Verdi laser (Coherent).

2.2.2 Assembly of Core-Shell Particles into Disordered Packings

We made amorphous packings by centrifuging aqueous suspensions of core-shell particles at 14000 g for two hours and removing supernatant until the final sample

was concentrated by a factor of 3. We then remixed the suspension by hand. The final volume fraction was high enough for the particles to pack into an amorphous structure. The packings were so dense that, when viewed under the microscope, there was no observable Brownian motion.

We also used depletion interactions [33, 34] to make dense packings. As depletant we used polyacrylamide (molecular weight $5\text{–}6\times10^6$, 100%, Polysciences). In a typical experiment, 1 mL of aqueous polyacrylamide solution at 1% w/w was added to 1 mL of core-shell suspension at 0.5% w/w. We waited one week for the particles to aggregate.

2.2.3 Characterization of Packings

We probed the structure of the concentrated core-shell suspensions with confocal microscopy. We prepared samples by confining 1–2 µL of suspension between a glass slide and a glass coverslip and sealing the chamber with optical-grade, low-viscosity, UV-curable epoxy (Norland Optical Adhesive 61, Norland Products, Inc.). Samples were imaged in reflection mode with a Leica TCS SP5 resonant confocal microscope using 63× and 100× NA=1.4 oil immersion objectives and an Argon laser at 458 nm and 476 nm.

We quantified the colors of our samples by measuring their optical transmission spectra over a range of angles from 0 to 30 degrees, measured with respect to the normal. Samples for spectroscopy were prepared in the same way as for confocal microscopy. Transmission spectra were measured using an Ocean Optics HR2000+ spectrometer. The incident light came from a halogen DH-2000 illumination lamp coupled into an optical fiber and collimated by a lens. The direction of the illumina-

tion beam was fixed with respect to the optical table, and the detector was positioned to face the beam. Light transmitted through the sample was focused by a lens onto another fiber, which was connected to the spectrometer. The setup was mounted on a two-axis goniometer allowing independent rotation of the sample and detector around a common axis (Figure 2.1). To account for the variation of illuminated area with angle, we normalized the transmitted spectrum to the spectrum transmitted at the same angle through a glass chamber filled with deionized water.

The resonant wavelength of each sample was determined from the transmission spectrum after correcting for non-resonant scattering. In the absence of correlations, the Beer-Lambert Law shows that the transmission should scale as

$$-\ln T/\sigma_s = \rho l \tag{2.1}$$

where T is the transmission (ranging from 0 to 1), σ_s is the single-particle scattering cross-section, ρ is the number density of scatterers, and l is the sample thickness [35]. We divided the negative logarithm of the measured transmission at each wavelength by the scattering cross-section of the particle core, which we calculated using Mie theory. Correlations introduce deviations from Equation 2.1 that result in clear peaks in the corrected spectra. We identified the resonances by locating the wavelengths corresponding to the maxima of the peaks.

2.3 Results and Discussion

2.3.1 Structure of Core-Shell Packings

We find that centrifuged particle suspensions are amorphous and packed, as can be seen in the microscope images shown in Figure 2.2. The 2D power spectra (insets) obtained from the spatial Fourier transforms of these images have a bright circular ring centered at zero wavevector, showing that the structures are isotropic. A peak in the power spectrum indicates a characteristic structural length scale $a = 2\pi/q_{\text{peak}}$, where q_{peak} is the magnitude of the wavevector. In both samples the length scale a agrees with the interparticle distance from the real-space images. This length is smaller than the measured hydrodynamic diameter of the core-shell particles because the poly(NIPAM-*co*-AAc) shells are deformable [26, 27, 28]. We were not able to measure inter-scatterer spacings much smaller than 310 nm because samples with these spacings did not yield clear real-space images for any layers besides the one closest to the coverslip, likely because such spacings are close to the diffraction limit. In subsequent studies, sub-diffraction optical imaging techniques such as Stochastic Optical Reconstruction Microscopy (STORM) [36] and PhotoActivated Localization Microscopy (PALM) [37] might prove useful for analyzing these structures.

2.3.2 Optical properties

Whereas dilute suspensions of the particles are turbid and colorless, the dense, centrifuged suspensions display colors that can be observed by eye (Figure 2.3a) and quantified by transmission spectra. The colors can be varied by changing the

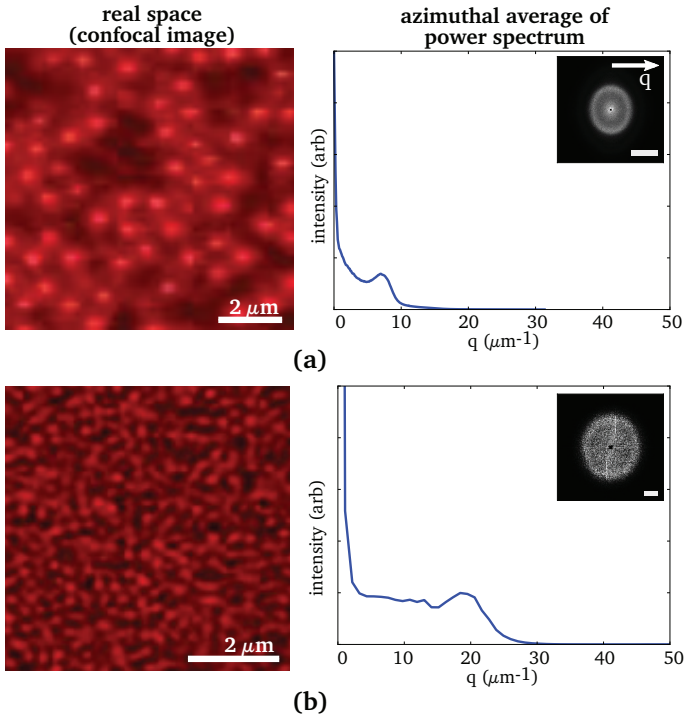

Figure 2.2: (a) Confocal microscope images (left) and azimuthally-averaged, 2D spatial power spectra of the images (right) for an amorphous, dense suspension of core-shell particles with hydrodynamic core and shell diameter (δ, d) = (230 nm, 2500 nm). The inset on the right is the average of the power spectra of a z-stack of confocal images with depth 19 µm. (b) Same as (a), but for a suspension of core-shell particles with hydrodynamic core and shell diameter (δ, d) = (180 nm, 940 nm). The inset on the right is the power spectrum of the image on the left. The peaks in frequency space correspond to a characteristic length scale of 897 nm in (a) and 322 nm in (b). In both insets we have masked the values around zero wavevector and we have set a threshold to the dynamic range for better contrast. The bars correspond to 10 µm^{-1}.

shell diameter, which controls the interparticle spacing. In Figure 2.3b and 2.3c we show photographs and transmission spectra as a function of angle for two dense packings of particles with the same cores but different shell diameters. Both were prepared using centrifugation. Because these samples have resonant wavelengths in the visible regime, the inter-particle spacing is too small to resolve with optical microscopy. However, the locations of the resonances – at 417 nm for the sample made of particles with shell diameter 430 nm and at 498 nm for a shell diameter of 640 nm – correlate with the particle sizes. Moreover, the colors are independent of the angle of illumination, indicating that the underlying structures are rotationally symmetric.

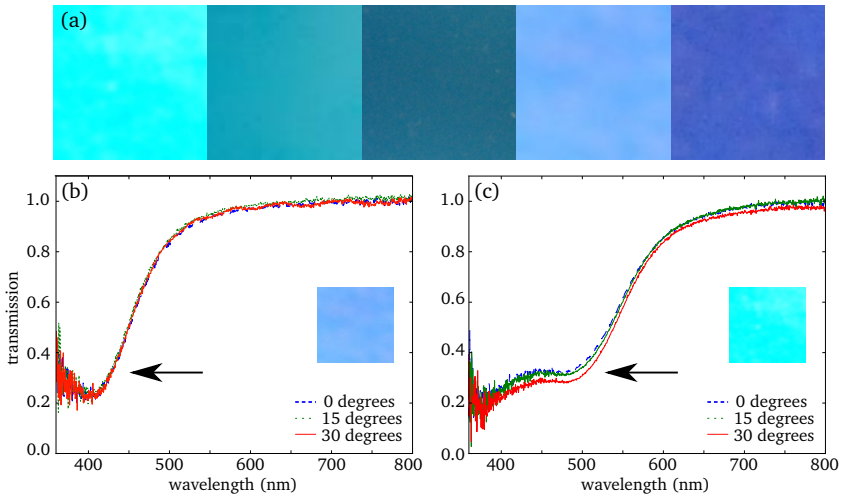

Figure 2.3: (a) Photographs of amorphous packings made from particles with various core and shell diameters, showing the range of appearances that can be produced. The field of view for each sample is 2 mm x 2 mm. (b),(c) Transmission spectra of two amorphous packings of core-shell particles with different shell diameters, at various angles. The hydrodynamic diameter of the shells is 430 nm in (b) and 640 nm in (c), and the diameter of the cores is 180 nm in both cases. The angles are measured between the axis of illumination-detection and the normal to the sample surface. Insets show photographs of samples with a 1 mm x 1 mm field of view.

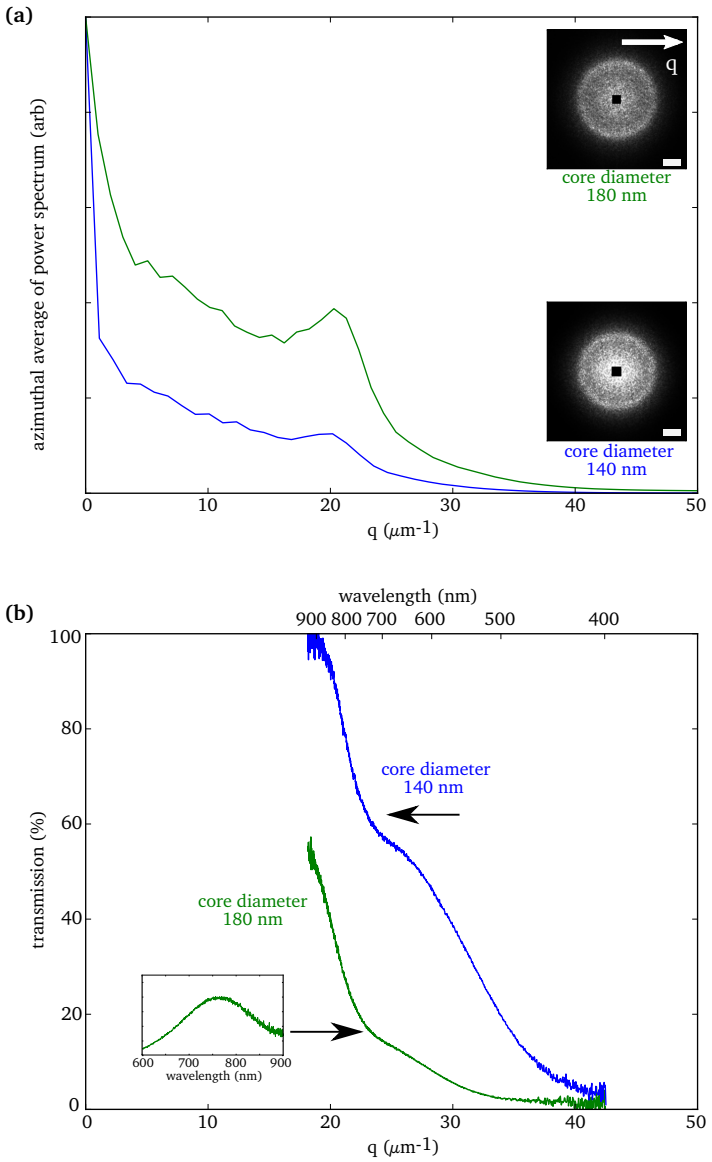

Figure 2.4: (a) Azimuthal averages of the power spectra of a z-stack of confocal images taken for two amorphous aggregates of core-shell particles. The depth of the stack was 6 µm in both cases. The 2D power spectra are shown in the insets, where we have masked the values around zero wavevector and we have set a threshold to the dynamic range of the image for better contrast. The bars are 10 µm^{-1}. The hydrodynamic core and shell diameters are (δ, d) = (180 nm, 940 nm) for the upper green curve and (140 nm, 1400 nm for the lower blue curve. The samples have a peak in spatial frequency at 20.3 µm^{-1} (green) and 20.2 µm^{-1} (blue). (b) Transmission spectra through the samples shown in (a) as a function of wavelength (upper x-axis) and wavevector q (lower x-axis). The values for q were calculated using $n = 1.35$. The sample thickness was about 130 µm in both cases. Inset:$-\ln T/\sigma_s$ (see text).

To elucidate the origin of these colors we used centrifugation to make disordered packings where the particle cores were far enough apart to image optically but close enough together to give rise to a resonance within the wavelength range of our spectrometer. The particles had hydrodynamic core and shell diameters (δ, d) = (180 nm, 940 nm). We determined the average interparticle spacing from the confocal images and from the spectral data shown in Figure 2.4 (green curves). The azimuthal average of the power spectrum of a confocal image stack (Figure 2.4a) has a peak at $q_{\text{peak}} = 20.3 \pm 2.4\ \mu\text{m}^{-1}$, corresponding to a length scale $a_{\text{confocal}} = 2\pi/q_{\text{peak}} = 310 \pm 36$ nm. This sample has a resonance at $\lambda_r = 765$ nm (Figure 2.4b).

We expect resonances to occur when the wavelength is comparable to the structural lengthscale, assuming that light is singly scattered and that the suspension behaves as an effective medium with an average index of refraction that depends on the volume fraction of the particles. Under these conditions, the magnitude of the incident wavevector at resonance should be equal to q_{peak}:

$$4\pi n/\lambda_r = 2\pi/a_r = q \tag{2.2}$$

where n is the effective refractive index of the medium, a_r the average interparticle spacing, and we have assumed normal incidence [16, 15]. We calculate the effective index from the Maxwell-Garnett relation [38], assuming that the index of the swollen poly(NIPAM-*co*-AAc) shells is the same as that of water:

$$n = n_{\text{water}} \sqrt{\frac{2n_{\text{water}}^2 + n_{\text{PS}}^2 + 2\phi(n_{\text{PS}}^2 - n_{\text{water}}^2)}{2n_{\text{water}}^2 + n_{\text{PS}}^2 - \phi(n_{\text{PS}}^2 - n_{\text{water}}^2)}} \tag{2.3}$$

where n_{PS} is the refractive index of polystyrene and ϕ is the volume fraction of polystyrene. We use this effective index because the particle packings are dense,

so that the scattered fields "see" an index intermediate between the particle and medium index. Although the Maxwell-Garnett approximation is typically used when the refractive index variations are much smaller than the wavelength, Vos and coworkers [39] showed that it is a good approximation even for photonic crystals, and Forster and coworkers [16] have shown the same for photonic glasses. From the interparticle spacing determined from the confocal images and the measured hydrodynamic diameter of the particle cores, we estimate the volume fraction of polystyrene to be $\phi = 0.10 \pm 0.03$. This leads to an effective index of $n = 1.35 \pm 0.01$. From Equation (2.2) we estimate the interparticle spacing to be $a_r = 283 \pm 3$ nm. The two values for the interparticle spacing, $a_{\text{confocal}} = 310 \pm 36$ nm and $a_r = 283 \pm 3$ nm, are in good agreement, considering that the measured interparticle distance is close to the diffraction limit. Thus the data are consistent with a model that assumes that the resonance arises from constructive interference of waves scattered from neighboring particle cores.

To explore the effect of changing the scattering cross-section of the particles, we made disordered packings using particles with the same inter-scatterer spacings but different core diameters. Figure 2.4 shows confocal and spectral data from two centrifuged suspensions with the same thickness. One sample contained particles with hydrodynamic core and shell diameters (δ, d) = (180 nm, 940 nm) and the other with (δ, d) = (140 nm, 1400 nm). Although the shell diameters differed, it was possible to make dense supensions with similar interparticle spacings through centrifugation. Indeed, both samples have peaks in their power spectra at similar wavevectors: $q_{\text{peak}} = 20.2 \pm 2.3$ µm^{-1} for the sample with the smaller cores and

$q_{\text{peak}} = 20.3 \pm 2.4\ \mu\text{m}^{-1}$ for the sample with the larger cores. As a result, they have similar optical resonances: $\lambda = 740$ nm and $\lambda = 765$ nm. However, changing the core diameter leads to a noticeable change in the transmitted intensity: the sample with the smaller cores is much more transparent than the sample with the larger cores. Thus for a given sample thickness the degree of transparency, which we expect to correlate with the color saturation, can be changed independently of the resonant wavelength.

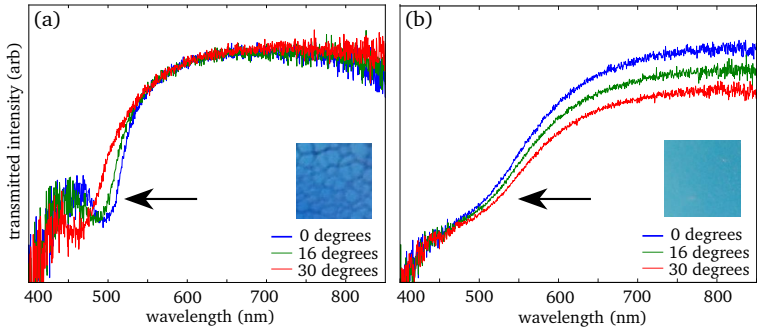

Figure 2.5: Transmission spectra through core-shell suspensions in which (a) the particles have crystallized and (b) the particles have formed a disordered packing. Both samples were prepared using a depletion attraction. The crystalline sample was prepared from a monodisperse suspension of particles with hydrodynamic core and shell diameters (δ, d) = (180 nm, 430 nm), whereas the amorphous sample was prepared from a bidisperse suspension of particles with hydrodynamic core and shell diameters (δ, d) = (180 nm, 430 nm) and (180 nm, 640 nm). Insets show photographs of the samples with a 2 mm x 2 mm field of view.

For comparison and to demonstrate the importance of disorder for the optical properties, we made both crystalline and disordered samples by introducing a depletion attraction between the particles. To make the crystalline sample we used a monodisperse suspension of core-shell particles with (δ, d) = (180 nm, 430 nm). The resulting sample, shown in the inset of Figure 2.5a, has cracks that form at well-defined angles, indicating facets and crystalline order. A sample prepared in the same

way but from a bidisperse suspension of core-shell particles with (δ, d) = (180 nm, 430 nm) and (180 nm, 640 nm), where the number ratio of smaller to larger particles was about 3:1, shows a resonance at a similar wavelength at normal incidence but with a different angular dependence. Whereas the resonance of the crystalline sample moves from cyan towards purple as the angle of illumination increases, in the amorphous sample it does not deviate from its value at normal incidence (Figure 2.5b).

2.4 Conclusions

We have demonstrated a way to create materials with structural colors by packing soft, core-shell colloidal particles. The softness of the particles facilitatesthe assembly of glassy structures, and the core-shell architecture of the particles allows independent control of the colors and the color transparency.

Even with this additional degree of control, we were not immediately able to create colors that cover the visible spectrum. Samples with resonances at green or blue wavelengths show distinct colors when viewed under ambient white light, but samples with resonances in the red look almost white. The absence of purely structural, angle-independent, saturated color with wavelength larger than about 550 nm is common to all amorphous photonic systems that we are aware of, including bird feathers, and will be adressed in the following chapter.

This chapter is based on the following publication: Sofia Magkiriadou, Jin-Gyu Park, Young-Seok Kim, and Vinothan N. Manoharan, "Disordered packings of core-shell particles with angle-independent structural colors," Opt. Mater. Express 2, 1343-1352 (2012) [40].

Chapter 3

On the Absence of Red Structural Color in Photonic Glasses, Bird Feathers and Certain Beetles

3.1 Introduction

Up to this point, we have not encountered any photonic glasses with saturated yellow, orange, or red color. While systems with angle-independent structural red have been reported [22, 17, 41, 24, 42], the color saturation for long-wavelength hues is poor compared to that for blue. Interestingly, red angle-independent structural color also appears to be rare in nature. Birds use structural color only for blue and green; red colors in bird feathers come from absorbing pigments [6]. And while the scales of the longhorn beetle *Anoplophora graafi* have structural colors that span the visible spectrum, there are no saturated red colors – only a pale purple [43].

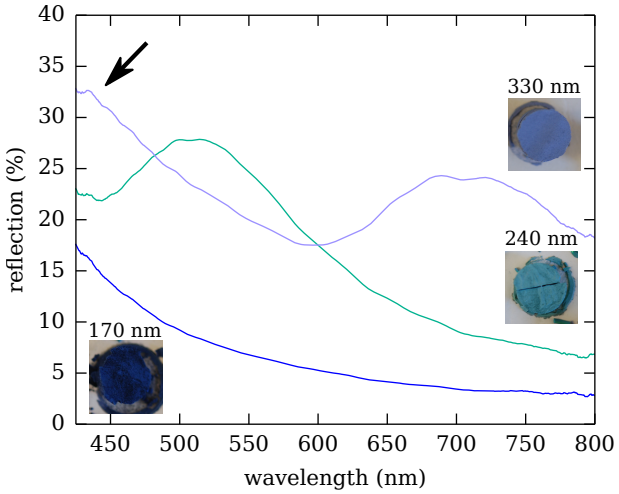

Figure 3.1: Measured reflectivity spectra for three similarly-prepared colloidal glasses of poly(methyl methacrylate) particles in air. Insets show photographs of the samples and diameters of the particles used to make the samples. The purple sample would appear red if not for the high reflectivity in the blue, indicated by the arrow.

The absence of red photonic glasses does not appear to have been acknowledged in prior literature, let alone explained. Previous work on photonic glasses [43, 15, 44, 45, 10, 16] has focused on structures found in nature and their biomimetic analogues, nearly all of which are blue. Noh and coworkers [46, 47] proposed a theoretical model based on single and double scattering to explain the optical properties of these blue samples, and Liew and coworkers [44] and Rojas-Ochoa and coworkers [2] showed that the inter-scatterer correlations not only give rise to color, but also suppress multiple scattering. However, if the color were entirely determined by correlations, one would expect that all colors could be made simply by linearly rescaling the structure. As we show below, this approach does not work (Figure 3.1).

Here we present a model that explains the absence of long-wavelength structural colors in photonic glasses. Our model accounts for both interparticle correlations as well as the scattering behavior of individual particles. We show that short-wavelength

resonances in the single-particle scattering cross-section, akin to cavity resonances, introduce a blue peak in the spectrum that changes the hue of a red structural color to purple. The model, which agrees with measured spectra from synthetic photonic glasses, provides a framework for understanding the limitations of current photonic glasses and enables the design of new systems without those limitations.

3.2 Experiment

To demonstrate that resonant scattering from the interparticle correlations is not sufficient to explain the colors of photonic glasses, we prepare colloidal glasses from poly(methyl methacrylate) (PMMA) spheres of various diameters and study their colors with spectrometry. Figure 3.1 shows color photographs and reflection spectra of samples prepared in the same way using three different particle diameters $d = 170$, 240, and 330 nm. These samples were prepared by mixing one part of an aqueous suspension containing 1% w/w carbon black (Cabot) and 2% w/w Pluronic F108 (BASF) with two parts of a monodisperse suspension of poly(methyl methacrylate) particles at 20% w/w, centrifuging the mixture at 5200 g for 30 minutes, removing the supernatant, and slip-casting on a gypsum substrate. The final samples are amorphous, dense packings of particles in air. The small amount of carbon black suppresses multiple scattering, making it easier to see the color [16].

We measure the reflection spectra as a function of wavelength with a fiber-optic spectrometer (OceanOptics HR2000+) mounted on an optical microscope (Nikon LV-100). The samples are illuminated with white light from a halogen lamp that is collimated by minimizing the condenser aperture. The divergence angle of the beam

is 0.02 radians. The light scattered by the sample is collected by a 50× objective (Nikon LU Plan Fluor, NA = 0.8) and imaged onto the detection fiber (OceanOptics QP600-2-UV/VIS). Because the objective NA is the limiting numerical aperture in our system, our measurements include light scattered up to a maximum angle $\theta_{\max} = \arcsin(0.80) = 0.93$ radians. We normalize all spectra to the reflected intensity from an aluminum mirror, we average the spectra measured over five different locations on the sample, and we smooth the spectra using a 50-nm window.

Two peaks are visible in the spectra, one at 515 nm in the $d = 240$ nm sample and the other at 710 nm in the $d = 330$ nm sample. The ratio of these peak wavelengths is approximately that of the two particle sizes $330/240 \approx 710/515$. The linear scaling is consistent with the hypothesis that the color is due to constructive interference of light scattered from correlated regions of particles. The high reflectivity of the $d = 170$ nm sample at short wavelengths suggests a structural resonance in the ultraviolet (UV), again consistent with this hypothesis. Thus the peak wavelength does appear to scale linearly with the particle size, and hence with the lengthscale of structural correlations, assuming that the volume fraction and structure of all of our samples are similar.

However, whereas the $d = 170$ nm sample appears blue and the $d = 240$ nm sample appears green, the $d = 330$ nm sample does not appear red. The reason is that its reflectivity rises toward the blue, suggesting a second peak at 430 nm or below. We have observed similar spectra in samples made of polystyrene and silica particles whenever the particle size is 250 nm or larger. Dong and coworkers [43] found a similarly-shaped spectrum, with one peak in the red and another apparent one at

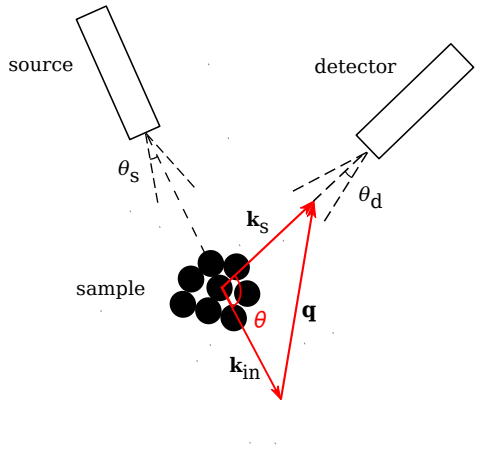

Figure 3.2: Scattering geometry for our model.

short wavelengths, for purple longhorn beetle scales [1]. Takeoka and coworkers [20] also observed a short-wavelength peak in the spectrum of their amorphous packings of $d = 360$ nm silica particles [2]. In order to understand the absence of red in all of these photonic glasses, we must understand the origin of this short-wavelength reflectivity peak.

3.3 Theory

To explain our observations, we use a single-scattering model where we treat scattering from a particle assembly as the result of two separable processes: scattering from each individual particle, as described by a form factor, and interference between waves scattered from the particles, as described by the structure factor of the glass. In our analysis, we first use the form and structure factor to calculate the differen-

[1] see the bottom spectrum in Figure 1c of [43]

[2] see Figure 1b, pink curve in their paper

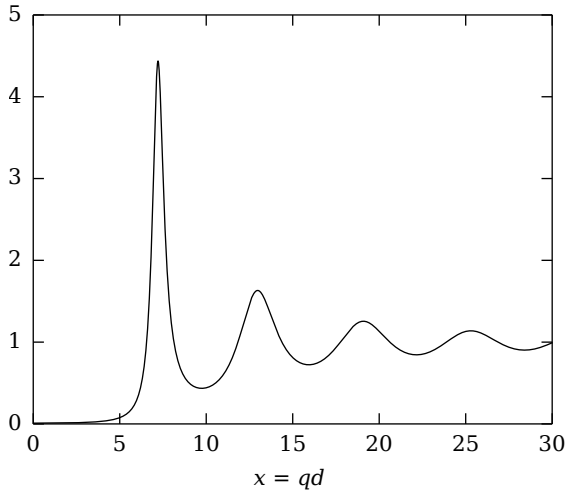

Figure 3.3: Structure factor of a colloidal glass with volume fraction $\phi = 0.55$ calculated from the Ornstein-Zernike equation under the Perkus-Yevick approximation.

tial scattering cross-section of a glass, and then we derive a formula that relates this cross-section to reflectivity, the quantity that we measure. According to our model, structural color in photonic glasses is primarily determined by the peaks of the structure factor. As we shall show, the form factor can either undermine this color or enhance it, depending on the structure of the system and the particle properties.

The scattering geometry that we model follows the picture presented in the Introduction (1.5); we show it again here in Figure 3.2, drawn in terms of a typical experimental setup. Recall that, assuming elastic scattering so that $|\mathbf{k}_{\text{in}}| = |\mathbf{k}_{\text{s}}| = k$, we can relate the magnitude of momentum change of the light field, q, to k, via Equation 3.1:

$$q = 2k \sin(\theta/2) \tag{3.1}$$

where $k = 2\pi n_{\text{eff}}/\lambda$, n_{eff} is the effective refractive index of the medium and λ is the wavelength of light in vacuum. As with the glasses of core-shell particles discussed in the previous chapter, for the effective index of the material we use a weighted average

calculated using the Maxwell-Garnett mean-field approximation [38]:

$$n_{\text{eff}} = n_{\text{med}} \sqrt{\frac{2n_{\text{med}}^2 + n_{\text{p}}^2 + 2\phi(n_{\text{p}}^2 - n_{\text{med}}^2)}{2n_{\text{med}}^2 + n_{\text{p}}^2 - \phi(n_{\text{p}}^2 - n_{\text{med}}^2)}}. \tag{3.2}$$

where n_{med} is the refractive index of the material surrounding the particles (air, in our case), n_{p} is the refractive index of the particles, and ϕ is the volume fraction occupied by the particles.

Assuming perfect monodispersity, we can express the differential scattering cross-section of a glassy ensemble of particles, $d\sigma_{\text{glass}}/d\Omega$, as a product of the form factor F and the structure factor S [48, 2]:

$$d\sigma_{\text{glass}}/d\Omega = (1/k^2)FS. \tag{3.3}$$

The form factor is related to the differential scattering cross section of a single particle, $d\sigma/d\Omega$, through $F = (1/k^2)d\sigma/d\Omega$ [35]; we calculate F using Mie theory [49, 35]. The structure factor is the Fourier transform of the pair correlation function of the particles [4]; we calculate it using a numerical solution to the Ornstein-Zernike equation with the Perkus-Yevick closure approximation [50]. In so doing, we are assuming that the structure of our particle glasses is close to that of a hard-sphere liquid. Figure 3.3 shows S calculated for a volume fraction $\phi = 0.55$ as a function of a dimensionless wavevector $x = qd$, where d is the diameter of the particles. We use this structure factor in all our calculations.

In the structure factor, the peak at x_o corresponds to the wavevector $q_o = 2\pi/d_{\text{avg}}$, where d_{avg} is the average center-to-center spacing between nearest neighbors. The peak wavevector q_o gives rise to constructive interference and color, because it sets the relative phase difference between light waves scattered from neighboring particles.

Resonant scattering occurs when this phase difference is an integer multiple of 2π. The wavelengths at which this happens can be determined from Equation 3.1:

$$\lambda = (4\pi n_{\text{eff}} d/x_{\text{o}}) \sin(\theta/2). \tag{3.4}$$

To describe the intensity of scattered light that reaches the detector, we integrate the differential scattering cross-section over the solid angle corresponding to the numerical aperture (NA) of our detector, taking into account transmission and refraction at the air-sample interface:

$$\sigma_{\text{detected}} = 1/k^2 \int_{\phi=0}^{2\pi} \int_{\theta_{\text{min}}}^{\pi} T_{\text{s-a}} F S \sin(\theta)\, d\theta\, d\phi \tag{3.5}$$

where $T_{\text{s-a}}$ is the Fresnel coefficient for transmission at the interface, $\theta_{\text{min}} = \pi - \arcsin(\text{NA}/n_{\text{p}})$ is the minimum scattering angle that we detect, and ϕ is the polar angle in the plane perpendicular to the scattering plane. There is no dependence on ϕ because the particles are spherical and the structure is isotropic.

To compare our calculations to our measurements we now derive a relation between σ_{detected} and the measured reflectivity, R. To do this we must account for extinction of light as it propagates through the sample; the intensity of light scattered from layers close to the surface is higher than the intensity of light scattered deeper in the sample because of attenuation by scattering. Under the assumption of single scattering, this attenuation scales exponentially with depth following Beer's Law, $I(x) = I_{\text{o}} e^{-\rho\sigma x}$, where ρ is the number density of particles, σ is the scattering cross-section for the full solid angle ($0 \leq \phi \leq 2\pi$, $0 \leq \theta \leq \pi$), and x is the distance light has propagated in the medium [35]. If the glass consists of slices of infinitesimal thickness δx, the total reflected intensity I is the sum of the intensities δI reflected from each slice:

$\delta I = I(x)\sigma_{\text{detected}}\rho\,\delta x$, where σ_{detected} is given by Equation 3.5. After integrating both sides and including the Fresnel coefficients for transmission ($T_{\text{a-s}}$) and reflection ($R_{\text{a-s}}$) at the air-sample interface, we find

$$R = T_{\text{a-s}}\frac{\sigma_{\text{detected}}}{\sigma}(1 - e^{-\rho\sigma l}) + R_{\text{a-s}} \tag{3.6}$$

where l is the optical thickness of the sample, or the maximum distance that light can propagate in it.

The reflectivity for a glass of poly(methyl methacrylate) spheres at a volume fraction $\phi = 0.55$, as calculated according to equation 3.6, is shown in Figure 3.4. We have omitted the Fresnel coefficient for reflection at the air-sample interface to better illustrate the features that arise from scattering from the bulk colloidal glass. The plot is shown as a function of the scaled particle size kd, where $k = 2\pi n_{\text{p}}/\lambda$. All terms in Equation 3.6—except for the Fresnel reflection coefficient, which adds an offset in amplitude—scale with kd. Thus this master curve describes reflectivity from a glass made of any particle size (of the same material and volume fraction), assuming dispersion is small. Depending on the particle sizes and refractive indices, different features of the curve will fall within the visible range; here we mark the edges of our detection range for $d = 334$ nm with the blue (425 nm) and red (800 nm) vertical dashed lines.

3.4 Results and Discussion

The calculated reflectivity reproduces the locations of all of the peaks in our data, as shown in Figure 3.5. The only free parameters are the volume fraction $\phi = 0.55$

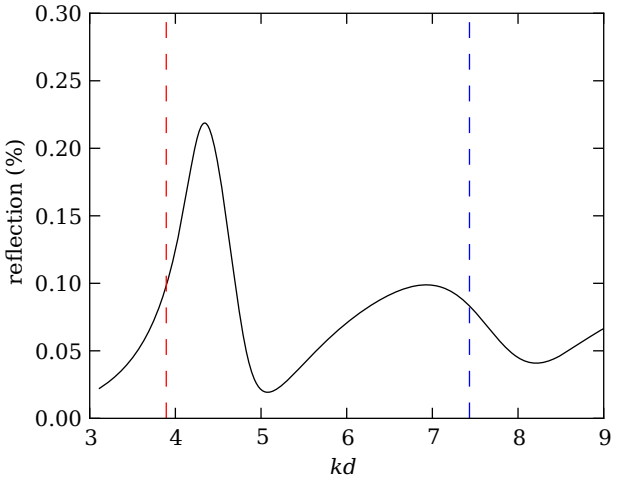

Figure 3.4: Calculated reflectivity as a function of kd for a photonic glass of spheres at a volume fraction $\phi = 0.55$, as calculated from Equation 3.6 with the Fresnel reflection coefficient omitted. The vertical dashed lines denote the kd-values that correspond to the range of visible wavelengths we detect, 425 nm (blue line) and 800 nm (red line), when the particle size is $d = 334$ nm.

and the thickness $l = 16$ μm. The peaks predicted by the theory coincide with the peaks in the data for particle diameters $d = 238$ nm (Figure 3.5(a)) and $d = 334$ nm (Figure 3.5(b)); these sizes are in good agreement with the sizes of the particles measured with scanning electron microscopy, 240 nm and 330 nm. The calculated reflectivity for the $d = 334$ nm system also reproduces the peak in the blue that we observe in the data.

With this model and data at hand we can address our original question: why does the glass made of 330 nm spheres have a resonance in the blue, when we expect the interparticle correlations to give rise only to a resonance in the red? Multiple scattering does not fully answer the question, because it does not predict any resonances – only a monotonic increase in the scattered intensity with decreasing wavelength. To identify the source of the reflection peaks in this sample, we compare our data

to the reflectivities predicted from the form factor alone and, in another comparison, the structure factor alone (Figure 3.5(c)). From the shapes of these two curves we immediately see that the blue peak comes from the form factor and the red peak from the structure factor, boosted by another peak in the form factor that occurs at a longer wavelength.

We conclude that the structural colors of our photonic glasses are determined not only by interference between waves scattered from correlated particles, but also by resonances in the single-particle scattering cross-section. This can also be seen by rescaling the measured reflectivities by $\sigma_{F,\text{detected}}$ and plotting them as a function of the dimensionless wavevector kd (Figure 3.6). Here $\sigma_{F,\text{detected}}$ is the single-particle differential scattering cross-section, integrated over the angle subtended by the detector:

$$\sigma_{F,\text{detected}} = 1/k^2 \int_{\phi=0}^{2\pi} \int_{\theta_{\min}}^{\pi} T_{\text{s-a}} F sin(\theta)\, d\theta\, d\phi \tag{3.7}$$

We see that after rescaling the long-wavelength reflectivity peak of the $d = 330$ nm sample coincides with the reflectivity peak of the $d = 240$ nm sample at the same value of kd, showing that these peaks arise from structural resonances, while the short-wavelength (high kd) peak in the $d = 330$ nm sample disappears, showing that it arises from single-particle scattering.

We note that the single-particle resonances responsible for the high reflectivity at small wavelengths are *not* the so-called "Mie resonances." Mie resonances are observed in the *total* single-particle scattering cross-section, obtained by integrating the differential scattering cross-section over all angles. The closest Mie resonance for a 334 nm poly(methyl methacrylate) particle in our effective medium occurs at 310

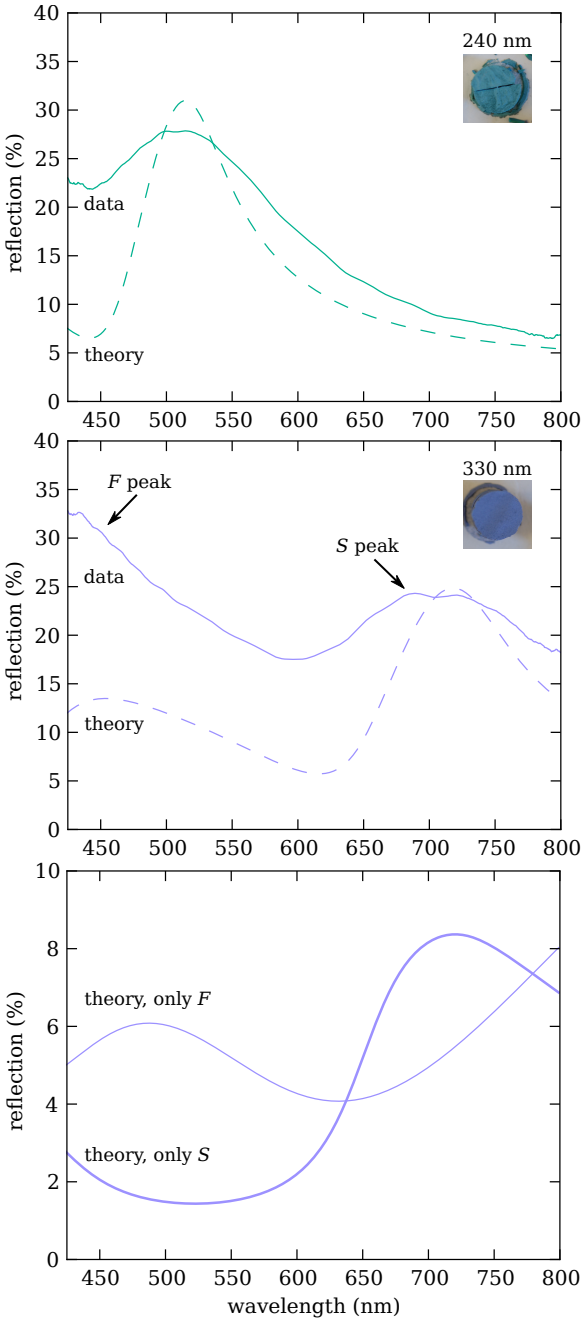

Figure 3.5: (a),(b) Measured (smooth lines) and calculated (dashed lines) reflection spectra of colloidal photonic glasses made of poly(methyl methacrylate) spheres. Theoretical spectra are calculated from Equation (3.6) with $\phi = 0.55$ and $l = 16$ μm. Particle diameters that best fit the measured peaks are 238 nm (a) and 334 nm (b), in good agreement with the measured particle diameters. (c) Calculated reflection spectrum for a photonic glass made from $d = 334$ nm particles, including only the structure factor (thick curve, divided by 10) and only the form factor (thin curve).

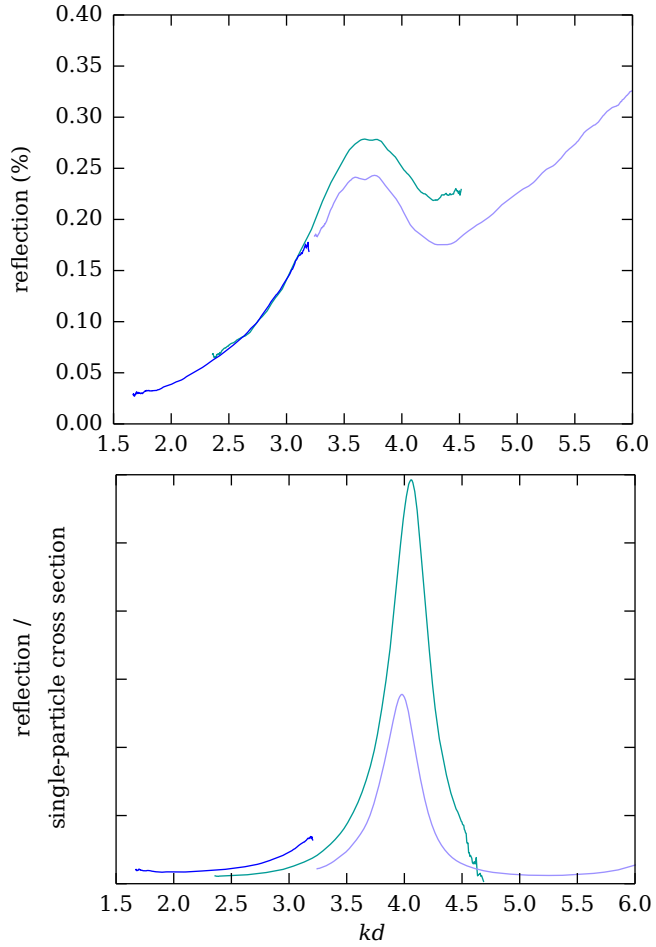

Figure 3.6: (a) Reflection spectra from Figure 3.1 plotted against the dimensionless lengthscale kd. Note the increased scattering at high kd-values (short wavelengths) for the $d = 330$ nm sample. (b) Same as (a) but normalized to the single-particle form factor integrated over the detected scattering angles, $\sigma_{F,\text{detected}}$, as defined in Eq. 3.7. The increased scattering at high kd-values disappears, indicating that it is due to the form factor. Differences in amplitude of the peaks are likely due to differences in the sample thickness l.

nm. Instead, as we shall show, the resonances that contribute to the high reflectivity at small wavelengths occur for scattering angles near backscattering.

We first consider the single-particle scattering cross-section for pure backscattering. This is proportional to the differential scattering cross-section for $\theta = \pi$. As shown in Figure 3.7, the backscattering cross-section can have one or more resonances, and the wavelengths at which these occur increase linearly with the particle "optical diameter," $n_{\mathrm{p}}d$, following the relation

$$\lambda_{\mathrm{resonant}} = 2n_{\mathrm{p}}d/z \tag{3.8}$$

where z is an integer that corresponds to the order of the resonance. This suggests that these resonances are akin to those of a Fabry-Pérot cavity, where constructive interference occurs for wavelengths that fit an integer number of times within the round-trip optical pathlength enclosed by the cavity [51]. Similar resonances occur in the differential scattering cross-section for all angles, as shown in Figure 3.8. Our calculations show that the resonant wavelength shifts toward the blue as the angle decreases. This blue-shift is consistent with the decrease in the round-trip optical pathlength inside the sphere with decreasing angle (see inset). When the differential scattering cross-section is integrated over the detected solid angle ($\theta = 150^\circ - 180^\circ$ for our detection numerical aperture of 0.8, after refraction), these resonances, though broadened, persist (Figure 3.5(c)). We therefore conclude that constructive interference of light inside the particles contributes to enhanced reflection at short wavelengths.

The model underestimates the amount of light scattered off-resonance, especially at short wavelengths. We attribute this discrepancy to multiple scattering. To esti-

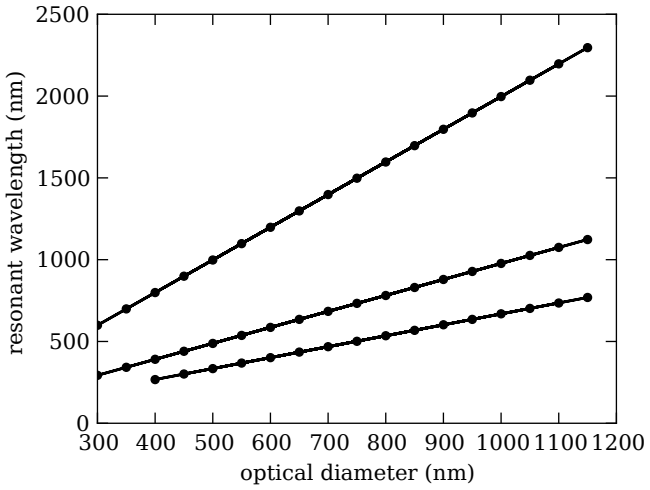

Figure 3.7: Resonant wavelengths of the backscattering cross-section, as calculated from Mie theory, as a function of optical diameter $n_{\mathrm{p}}d$ for a refractive index contrast $m = 1.2$, which corresponds to that in our experimental system. The resonant wavelength follows the linear relation $\lambda = 2n_{\mathrm{p}}d/z$ (solid lines), where z is the order of the resonance. Lines correspond to different values of z (top: $z = 1$, middle: $z = 2$, bottom: $z = 3$).

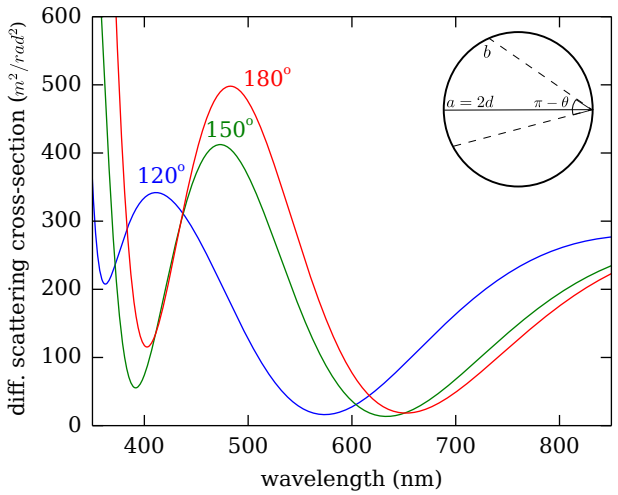

Figure 3.8: Single-particle differential scattering cross-sections for various scattering angles as a function of wavelength for a 330 nm PMMA sphere in a colloidal glass of spheres in air at a volume fraction $\phi = 0.55$. The blue-shift in the resonance is consistent with the decrease in optical pathlength inside the sphere with decreasing angle: The longest possible pathlength a is twice the diameter, and $a > b$ for any angle that differs from backscattering.

mate the relevance of multiple scattering in our samples, we calculate the transport length, l_t: the distance light traverses within a sample before its direction is randomized. If the sample thickness is larger than the transport length, then there is multiple scattering. Moreover, interference can lead to reduced values for the transport length on resonance that are associated with resonant backscattering [2]. The transport length provides an alternative way to describe the conditions for structural color: For a colloidal glass to have a specific color, the transport length for this color needs to be shorter than the transport length for the other colors – otherwise all wavelengths will undergo multiple scattering and mix diffusely, resulting in white. Mathematically, the transport length is given by the following expression:

$$l_t = 1/\rho\sigma_t \tag{3.9}$$

where ρ is the number density of particles and

$$\sigma_t = 1/k^2 \int_{\phi=0}^{2\pi} \int_{\theta=0}^{\pi} FS(1-\cos\theta)\sin\theta \, d\theta \, d\phi \tag{3.10}$$

is the transport cross section [2]. Figure 3.9 shows l_t as a function of wavelength for our green and purple samples, in comparison with the fitted sample thickness of 16 μm that we obtained from the reflectivity calculations shown in Figure 3.5. For both samples the transport length generally increases with wavelength but has a dip on the structure factor resonance, as previously observed [2]. Moreover, in both samples the transport length is smaller than the fitted sample thickness at short wavelengths, consistently with our hypothesis that multiple scattering contributes additional blue light that is not captured by our single-scattering model. Finally, only the green sample comes close to satisfying our condition for color: except for the

400–430 nm regime, its transport length on resonance is shorter than it is for all other wavelengths. The purple sample, on the other hand, fails to satisfy this condition entirely: its transport length on resonance is much longer than the transport length for most of the visible wavelengths, meaning that there is diffuse scattering of all colors in addition to resonant backscattering. This is consistent with the fact that the purple color we see is not very saturated, since multiple scattering contributes a white background to the structural color. The importance of multiple scattering in these samples can be studied in the future by investigating the effect of sample thickness on color. One effective way to control the thickness of the samples is by changing the amount of carbon black in them, that sets the absorption length in the sample – namely the distance light traverses in them before it is absorbed. To minimize multiple scattering and enhance color saturation, the samples should have enough carbon black to ensure that the absorption length in the sample is shorter than the transport length for the off-resonant wavelengths.

Our results show that the absence of red structural color in photonic glasses can be attributed to the blue scattering resonances within the component particles. The single-particle scattering resonances occur in addition to the resonances from inter-particle correlations, meaning that structural color in photonic glasses arises from the combination of resonant scattering from the structure *and* from the individual particles. For blue and green structural colors, these single-particle scattering resonances do not affect our perception of color, because they occur in the ultraviolet. While these observations are based on glasses of poly(methyl methacrylate) spheres, the same principles apply to most typical colloidal materials, such as polystyrene

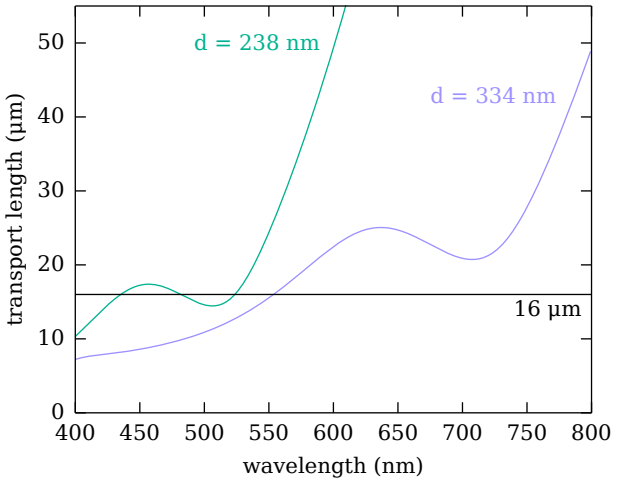

Figure 3.9: Calculated transport length as a function of wavelength for the green ($d = 238$ nm) and purple ($d = 334$ nm) photonic glasses of poly-methylmethacrylate spheres, using a volume fraction $\phi = 0.55$, as calculated from Equation 3.6 with the Fresnel reflection coefficient omitted. The vertical dashed lines denote the kd-values that correspond to the range of visible wavelengths we detect, 425 nm (blue line on the right) and 800 nm (red line on the left), when the particle size is $d = 334$ nm.

and silica, whose refractive indices are not significantly different from that of that of poly(methyl methacrylate). The chitin particles in beetle scales have similar optical properties [43].

Although the single-particle resonances we observe should also occur in photonic crystals, the structure factor in crystals is much more sharply peaked than in glasses, so that structural resonances can dominate the single-particle resonances and photonic crystals can have structural red color. The price to be paid for this red color is strong angular dependence: changing the angle between source and detector changes the resonant wavelength, leading to iridescence. Photonic glasses have a lower and broader peak in the structure factor as a consequence of their disorder. The breadth of the peak allows the glass to maintain nearly the same structural color over a range of angles between the source and the detector. At the same time, the low peak amplitude

(relative to a crystal) makes the color of the glass susceptible to contamination from the single-particle resonances. Thus we see that there is an inherent tradeoff between angular independence and structural red color.

Can this tradeoff be broken? To do so, we would need to manipulate the resonances from two independent processes: single-particle scattering and coherent scattering from the particle assembly. The characteristic lengthscale for the single-particle scattering resonances is the particle optical diameter $n_{\mathrm{p}}d$ (Equation 3.8), and for the structural resonances it is the effective interparticle spacing $n_{\mathrm{eff}}d_{\mathrm{avg}}$ (Equation 3.4). Our control parameters are therefore the particle diameter d, its refractive index n_{p}, the interparticle spacing d_{avg}, and the index of the medium n_{med}, which determines the effective index n_{eff}. To make a red photonic glass, we can tune these parameters to either eliminate the second resonance of the form factor entirely, or to blue-shift it into the ultraviolet while keeping the peak of the structure factor at long wavelengths.

To eliminate the form factor resonances we can take advantage of dispersion, namely the inherent wavelength dependence of the refractive index. Each material has its own dispersion curve, often described by a polynomial of the form $n(\lambda) = \sum_{\mathrm{i}} C_{\mathrm{i}}/\lambda^{2i}$, where C_{i} are called the "Cauchy coefficients" and are usually determined experimentally [51, 52]. With some consideration, it is possible to choose a combination of materials for the scatterers and the medium such that the refractive indices have very similar values at short wavelengths but deviate from each other at longer wavelengths, thus rendering the scatterers invisible to light only at short wavelengths. In Figure 3.10(a) we show the dispersion curves for such a combination of commercially available materials: poly-methylmethacrylate and refractive index

liquid Cargille A 1.484. As desired, the two dispersion curves come very close at short wavelengths, but then deviate from each other at long wavelengths. As we show in Figure 3.10(b) the reflectivity of a colloidal glass of poly-methylmethacrylate particles in this oil is almost zero at short wavelengths and the form factor resonance is substantially suppressed, allowing the structure factor resonance to dominate – in contrast to the reflectivity of a similar poly-methylmethacrylate particle in air. A similar dispersion trick has been previously employed in diffusely scattering structures to generate a variety of colors [41]. Note that, in designing such a system, it will be important to adjust the sample thickness to account for the much reduced refractive index contrast and scattering cross section.

Another way to eliminate the effect of the form factor resonance on color is by blueshifting it into the ultraviolet and away from the visible spectrum. This can be achieved with particles that have a small optical diameter, as shown in Figure 3.7. The simplest way to reduce the optical diameter is to use particles with a refractive index smaller than that of the medium. In these *inverse* glasses, the diameter of the particles is about the same as the spacing between their centers ($d_{\text{avg}} \sim \sqrt{6}d/3$), but their lower refractive index makes the optical pathlength inside each particle shorter than the optical pathlength between two particles. As a result, the form factor resonances are blue-shifted compared to those of our poly(methyl methacrylate) colloids of similar size, while the structure factor resonances remain at about the same wavelength. We present our progress towards the realization of such systems in Chapter 5.

Alternatively, blue-shifting the form factor resonance without shifting the structural resonance can also be achieved by decoupling the particle size from the interpar-

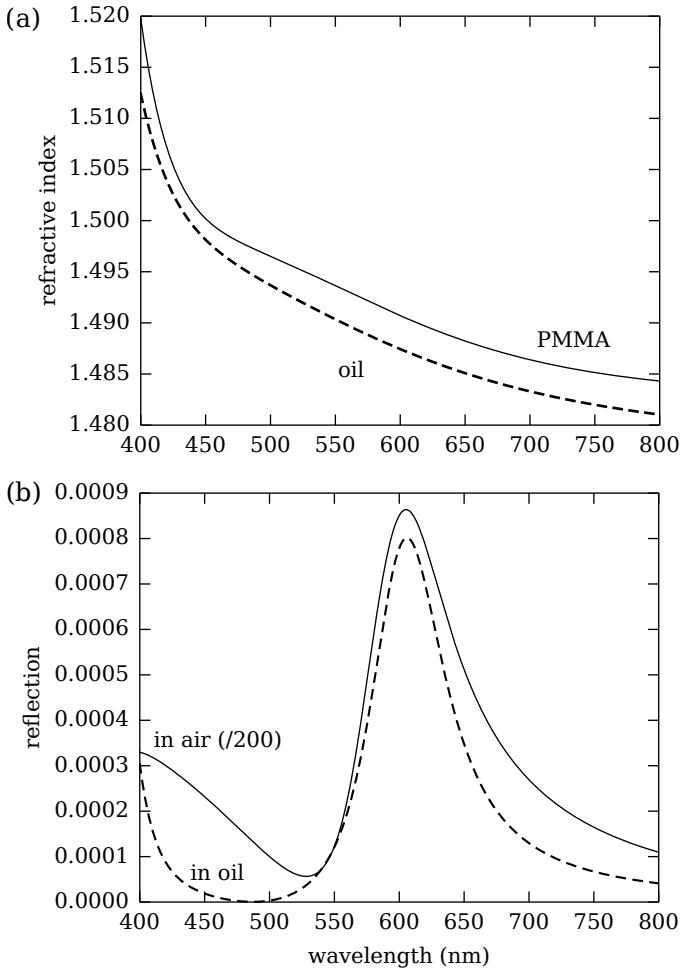

Figure 3.10: We can use dispersion to partially index-match the scatterers and the medium and suppress scattering in the blue. (a) Dispersion curves for poly-methylmethacrylate and for a Cargille refractive index liquid with $n = 1.486$ at 589 nm. The indices of the two materials are very similiar at short wavelengths and deviate from each other at larger wavelengths. (b) Detection cross section for a glass of poly-methylmethacrylate particles in air and in the same oil as in (a). Because the poly-methylmethacrylate is almost index-matched to the oil at short wavelengths, scattering in that regime is suppressed. For comparison, we also show the reflectivity for a similar glass of particles are in air, divided by 200. In both calculations we use $\phi = 0.55$ and $l = 16\mu$m; the particle sizes are 238 nm for the system in oil and 278 nm for the system in air, chosen to yield a resonance at the same wavelength.

ticle spacing and using smaller particles as the scatterers. This can be done by packing core-shell particles with a strongly scattering core and a transparent shell, like the ones described in Chapter 2. In Chapter 4 we show that this approach indeed enables the creation of full-spectrum, angle-independent structural pigments [42]. These pigments still suffer from poor color saturation in the red compared to the blue, but, as we discuss, the short-wavelength reflectivity is substantially reduced relative to colloidal glasses made of conventional, homogeneous particles.

One can combine the core-shell and inverse-structure approaches to design a system with a single visible resonance at long wavelengths. In particular, the shell diameter could be chosen such that the interparticle spacing gives rise to a resonance in the red, and the core diameter chosen such that the first-order peak in the form-factor boosts the peak from the structure factor, while the second-order form-factor peak is fully in the ultraviolet. Our calculations show that such a structure could be made from core-shell particles with air cores and silica shells, embedded in a silica matrix, as shown in Figure 3.11.

Curiously, the photonic structures found in bird feathers resemble these inverse glasses: they often consist of air pockets in a matrix of β-keratin [15, 6] that has a refractive index close to that of silica [53]. However, birds do not seem to have taken advantage of their inverse structures for colors other than blue. They rely instead on pigments to acquire yellow, orange and red colors [6, 54]. Whether this is due to a physical effect not accounted for in our model or is the result of evolution or chance remains to be seen.

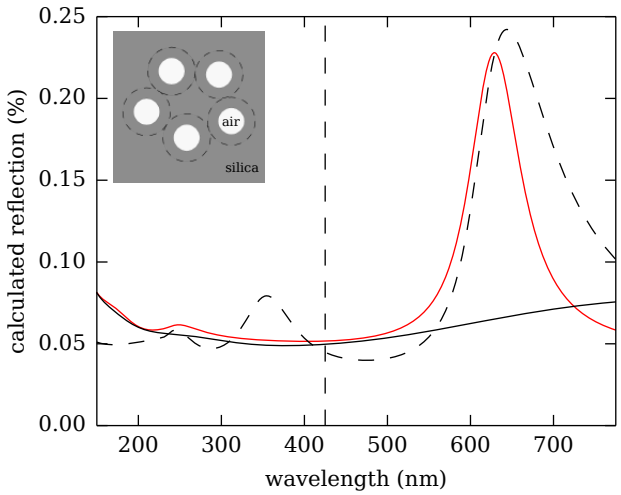

Figure 3.11: Calculated reflection for an inverse glass of core-shell spheres engineered to scatter most strongly in the red. The continuous red curve includes both the structure and the form factor, the dashed black curve only the structure factor (divided by 2), and the black continuous curve only the form factor. The vertical dashed line marks 425 nm, the low-wavelength limit in our spectral measurements. The optimal design has air cores with diameter 260 nm and silica shells with diameter 280 nm, and the particles are embedded in a silica matrix. The reflectivity peak at 632 nm is primarily due to the structure factor and determined by the shell diameter. One form-factor resonance occurs in the near-IR, boosting the structural resonance in the red, and another occurs deep in the ultra-violet (at about 150 nm), too far away from the visible regime to affect the color.

3.5 Conclusion

We have described a physical mechanism that explains the scarcity of angle-independent structural red color in photonic glasses. Our model shows that interparticle correlations alone are not sufficient to understand the reflectivity of photonic glasses. The scattering behavior of their constituent particles plays an equally important—and previously unrecognized—role. In particular, interference of light *inside* the particles can lead to enhanced scattering at wavelengths other than those related to the interparticle correlations. Our model describes our experimental observations well, and it can be used to guide the design of new photonic glasses with purely red structural color.

To this end, we have shown that it is possible to control the locations of both the single-particle scattering resonances and the structural resonances by tuning the refractive indices, particle sizes, and interparticle distances. Our model predicts that inverse glasses made of core-shell particles with a low-index core and a high-index shell that is index-matched to the medium might produce angle-independent structural red color. If future experiments show that such structures show poor color saturation in the red, these results would suggest that another mechanism, such as multiple scattering, should be accounted for. If successful, these structures would complete the palette of visible colors achievable with photonic glasses, opening the path to their use in practical applications such as long-lasting dyes or reflective displays.

In the following two chapters, we describe our progress towards angle-independent structural red color with the systems proposed here: core-shell particles with transparent shells, and inverse glasses.

This chapter is based on the following manuscript: Sofia Magkiriadou, Jin-Gyu Park, Young-Seok Kim, Vinothan N. Manoharan, "On the Absence of Red Structural Color in Photonic Glasses, Bird Feathers and Certain Beetles," Phys. Rev. E 90, 062302 (2014) [55].

Chapter 4

Full-Spectrum Photonic Pigments with Non-Iridescent Structural Colors through Colloidal Assembly

4.1 Introduction

As we have seen, there are two major challenges in making isotropic structural coloration through colloidal assembly: independent control of the resonances due to single-particle scattering from the resonances due to inter-particle correlations, and control over multiple scattering. If the size of the colloidal particles is too large, the structural resonance at long wavelengths is compromised by single-particle scattering resonances at shorter wavelengths [20]. If the particle aggregate is too thick, white color from multiple scattering dominates, compromising the color saturation [16]. Therefore, control over both single-particle and multiple scattering is necessary to

realize photonic pigments with pronounced structural colors that cover the visible range.

In this chapter we present a new colloidal assembly method to fabricate micro-encapsulated photonic pigments that cover the full spectrum. Our approach combines the flexibility of the soft core-shell particles that we described in Chapter 2 with a technique that allows precise control over the total sample size. Hence, our design has three structural length scales, each of which is primarily associated with a different scattering process that affects structural color. The scatterer size, set by the cores, determines the resonances of the form factor; the inter-scatterer distance, set by the shells, determines the resonances of the structure factor; and the sample size, set by the capsule size, determines the amount of multiple scattering. It is particularly important that, in this system, the core particles, which dominate the scattering, can be small compared to the shells. This has a twofold benefit: first, it allows blueshifting of the form factor resonances that can interfere with long-wavelength structural color, as we have seen in Chapter 3; second, it mitigates multiple scattering, since small particles scatter less. In this way, coherent scattering due to the structure factor dominates, and we are finally able to make photonic pigments with isotropic structural colors throughout the visible range.

4.2 Methods

We use microfluidic techniques to produce spherical microcapsules approximately 100 μm in diameter that contain densely packed, amorphous arrays of colloidal particles. The encapsulated particles are polystyrene/poly (N-isopropylacrylamide-co-

acrylic-acid) (PS/poly-NiPAm-AAc) core-shell particles with shells that are closely index-matched to the surrounding water, as described in Chapter 2.

We start with an aqueous suspension of PS/poly-NiPAm-AAc core-shell particles synthesized through seeded emulsion polymerization [28], using polystyrene nanoparticles of hydrodynamic radius $R_{\mathrm{h,PS}} = 78 \pm 5$ nm as seeds. The ratio of NiPAm monomer to seed particle, which controls the thickness of the soft polyNiPAm shell, is 0.5% w/w, yielding a core-shell hydrodynamic radius $R_{\mathrm{h,core-shell}} = 168 \pm 17$ nm. We match the refractive index of the shell to that of the suspension medium by co-polymerizing 4.0% w/w of acrylic acid (AAc) in the polyNiPAm shell. We then encapsulate this suspension in the innermost phase of water-in-oil-in-water double-emulsion droplets using a capillary microfluidic device, as shown in Figure 4.1(a) [56]. The aqueous suspension and an oil phase containing a UV-curable monomer, ethoxylated trimethylol-propane triacrylate (ETPTA), are injected simultaneously through a hydrophobic capillary, creating a train of suspension droplets in the continuous monomer flow. The hydrophobicity of the capillary prevents the droplets from wetting. This core-sheath is then emulsified into the continuous phase, aqueous poly(vinyl alcohol) (PVA, 10%, w/w), at the tip of the capillary, yielding water-in-oil-in-water double-emulsion drops where the innermost phase is the particle suspension and the middle phase is an ultra-thin shell of oil, as shown in Figure 4.1(b). These droplets are the precursors to our photonic microcapsules.

The precursor droplets are designed to facilitate the preparation of amorphous nanostructures. The double emulsion makes it possible to concentrate the suspension by an osmotic pressure gradient [57]. Furthermore, the softness of the particle

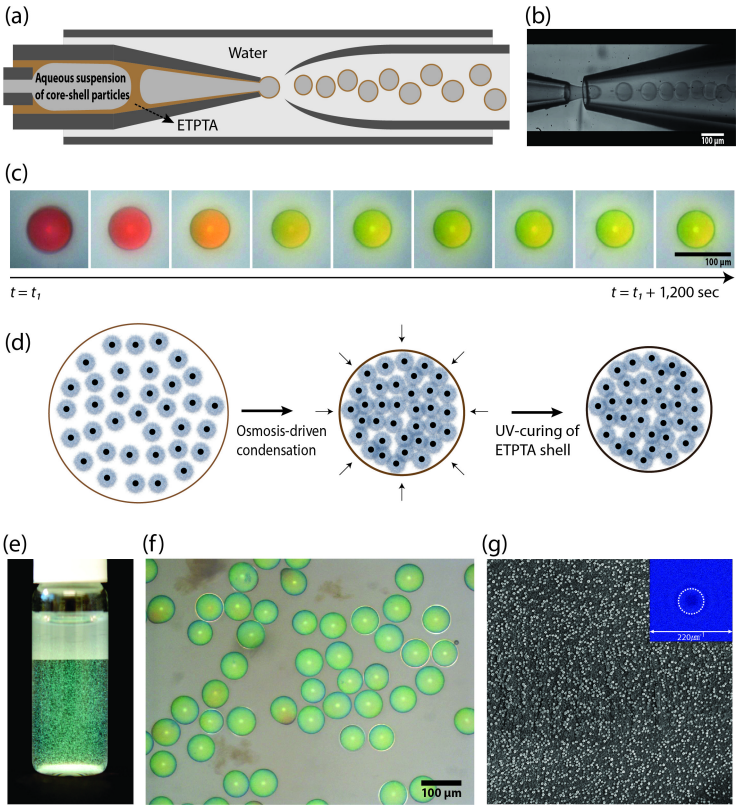

Figure 4.1: Fabrication of photonic pigments. a) Schematic of a capillary microfluidic device for the production of water-in-oil-in-water double-emulsion droplets with a thin ethoxylated trimethylolpropane triacrylate (ETPTA) membrane. b) Optical micrograph showing generation of uniform water-in-oil-in-water droplets. The innermost phase contains an aqueous suspension of coreshell particles with a volume fraction $\phi_{\text{coreshell}}) \sim 0.28$. c) Time-series optical micrographs of osmosis-driven condensation of droplets at 340 mOs/mL, where t_1, the elapsed time for microscope analysis, is about 5 minutes. d) Schematic of the structure of particles during osmosis-driven condensation. e,f) A photograph and an optical micrograph of the photonic pigments in water after UV-curing of the ETPTA shell. The sample is compressed at 440 mOs/mL. A few capsules show yellow spots due to local deformation of the polymer shell. g) Scanning electron micrograph of a cross-section of a cryogenically fractured photonic pigment microcapsule prepared under compression at 440 mOs/mL. The field of view is 20 μm wide. The inset in (g) is the two-dimensional Fourier power spectrum derived from (g), with a 220 μ^{-1}m field of view.

shells inhibits crystallization during concentration [29]. We concentrate the particles by placing the water-in-oil-in-water droplets into an aqueous solution of PVA and sodium chloride (NaCl), creating a positive osmotic pressure difference that forces the water out through the thin ETPTA membrane and causes the droplets to shrink isotropically, as shown in Figure 4.1(c). As the droplets shrink, they develop color that blue-shifts with increasing concentration (Figure 4.1(c)). We then polymerize the ETPTA layer by exposing it to ultraviolet light for 30 seconds, as illustrated in Figure 4.1(d). The ETPTA layer ($n_{\mathrm{ETPTA}} = 1.4689$) yields a 0.8-$\mu$m-thick, optically transparent shell after curing. The resulting microcapsules are monodisperse and display non-iridescent structural colors, as shown in Figures 4.1(e) and (f).

The internal structure of these photonic pigments is random and isotropic, as we see in the scanning electron microscope image of a cryogenically fractured microcapsule in Figure 4.1(g). The two-dimensional power spectrum of a 20 μm $\times$ 20 μm cross-section is in the inset. We observe a ring pattern; as we discussed in the Introduction, this indicates that the structure is isotropic, with a characteristic lengthscale of short-range order that we calculate to be 217 nm.

We can control the colors by changing the average distance between the polystyrene cores, which are the primary scatterers. The inter-scatterer distance depends on the degree of droplet compression, which depends on the osmotic pressure difference used to concentrate the particles. For example, we can prepare red microcapsules at 180 mOsm/L, yellow ones at 260 mOsm/L, and green ones at 440 mOsm/L. At each osmolarity, we incubate emulsion droplets containing core-shell particles with $R_{\mathrm{h,core-shell}} = 168 \pm 17$ nm for two hours to equilibrate the osmotic pressure before

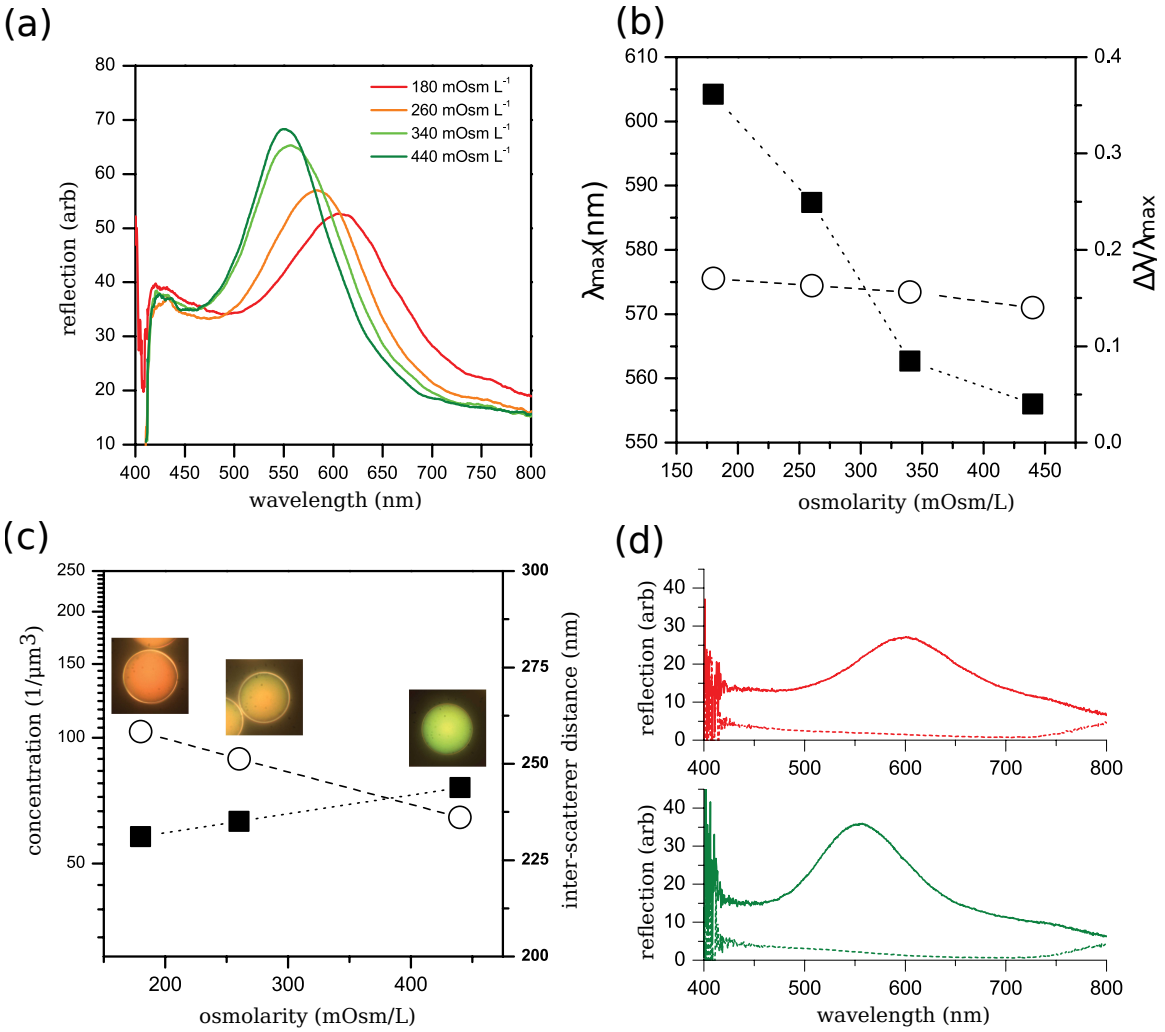

Figure 4.2: Control of structural colors through osmotic pressure. a) Reflectance spectra of the microcapsules equilibrated under different osmotic pressures. b) Plots of peak positions (dark squares) and normalized full-width at half maximum (FWHM; open circles) of the microcapsules as a function of osmotic pressure. c) Estimated concentration of PS scatterers (dark squares) and average spacing between PS scatterers (open circles) as a function of osmotic pressure. Insets are bright-field (reflection) optical micrographs of red, yellow, and green microcapsules prepared under 180 mOsm/L, 260 mOsm/L, and 440 mOsm/L, respectively. The field of view for the insets is 100 μm wide. d) Co-polarization (lines) and cross-polarization (dots) reflection spectra of red (upper) and green (lower) photonic microcapsules.

we polymerize the ETPTA shell. As we see in the reflectance spectra of the resulting microcapsules, shown in Figure 4.2(a), the characteristic peak shifts from 610 nm to 550 nm as the osmotic pressure increases, but the normalized full width at half-maximum $\Delta\lambda/\lambda_{\max}$, shown in Figure 4.2(b), remains almost constant, indicating that the shrinking leads to rescaling of the structures without inducing any qualitative change.

4.3 Results and Discussion

To understand the relation between the optical properties of the photonic balls and the structures they contain, we first estimate the inter-scatterer distance d from the reflection spectra. For simplicity, we assume back-reflected light, namely a scattering angle $\theta = 180$ degrees. Then, from Equation 1.10

$$d = 0.6\lambda_{\mathrm{o}}/n_{\mathrm{medium}} \tag{4.1}$$

where λ_{o} is the resonant wavelength and n_{medium} is the effective refractive index of the medium, which depends on the volume fraction of the polystyrene cores via the Maxwell-Garnett relation (Equation 3.2). The factor of 0.6 in Equation 4.1 comes from the average spacing between particles in a colloidal glass of hard spheres with volume fraction $\phi = 0.65$. Our particles are soft, however this serves as a useful starting point. Because we do not know a priori the volume fraction of polystyrene, we calculate d using an iterative process: We first use Equation 4.1 to calculate d_0 with $n_{\mathrm{medium},0}$ equal to the refractive index of water, then we use d_0 to estimate the volume fraction of polystyrene, $\phi_{\mathrm{PS}} = (d_{\mathrm{core}}/d_0)^3$, and a new effective $n_{\mathrm{medium},1}$, and

from Equation 4.1 we calculate a new d_1 from $n_{\text{medium},1}$. The values for d converge quickly, and we find a reasonable $n_{\text{medium}} \sim 1.39$. From this calculation, we estimate the number density of polystyrene scatterers and the average distance between them as a function of osmotic pressure, shown in Figure 4.2(c). We find that, for the green microcapsules, the inter-scatterer distance calculated from the spectrum (236 nm) agrees reasonably well with that obtained through Fourier analysis of an SEM image of the same sample (217 $\pm$ 14 nm). On the basis of the spectra, calculations, and SEM analysis, we conclude that the particles are compressed into roughly 35% of their original volume at 440 mOsm/L.

In all of these samples, coherent scattering from the inter-particle correlations dominates over single-particle scattering and over multiple scattering. We characterize all scattering away from the structure factor resonance by the intensity at short wavelengths (420-435 nm), where it contributes the most. The ratio of the peak intensity on the structure factor resonance to the background intensity, $I_{\text{max,S}}/I_{\text{background}}$ shown in Figure 4.2(a), increases from 1.35 for red photonic microcapsules to 1.83 for green. This quantity is one measure of color saturation: the lower the value, the whiter the sample, due to mixing of the resonant color with blue light. Although the background scattering is not negligible, particularly for red microcapsules, it is significantly less than scattering due to inter-particle correlations for all the samples. Moreover, for all microcapsules, this background scattering is drastically less than it is for the more conventional colloidal glasses of poly-methylmethacrylate particles discussed in Chapter 3. For comparison, the corresponding ratio $I_{\text{max,S}}/I_{\text{background}}$ for those is 1.24 for the green sample and 0.74 for the purple sample. In the last case

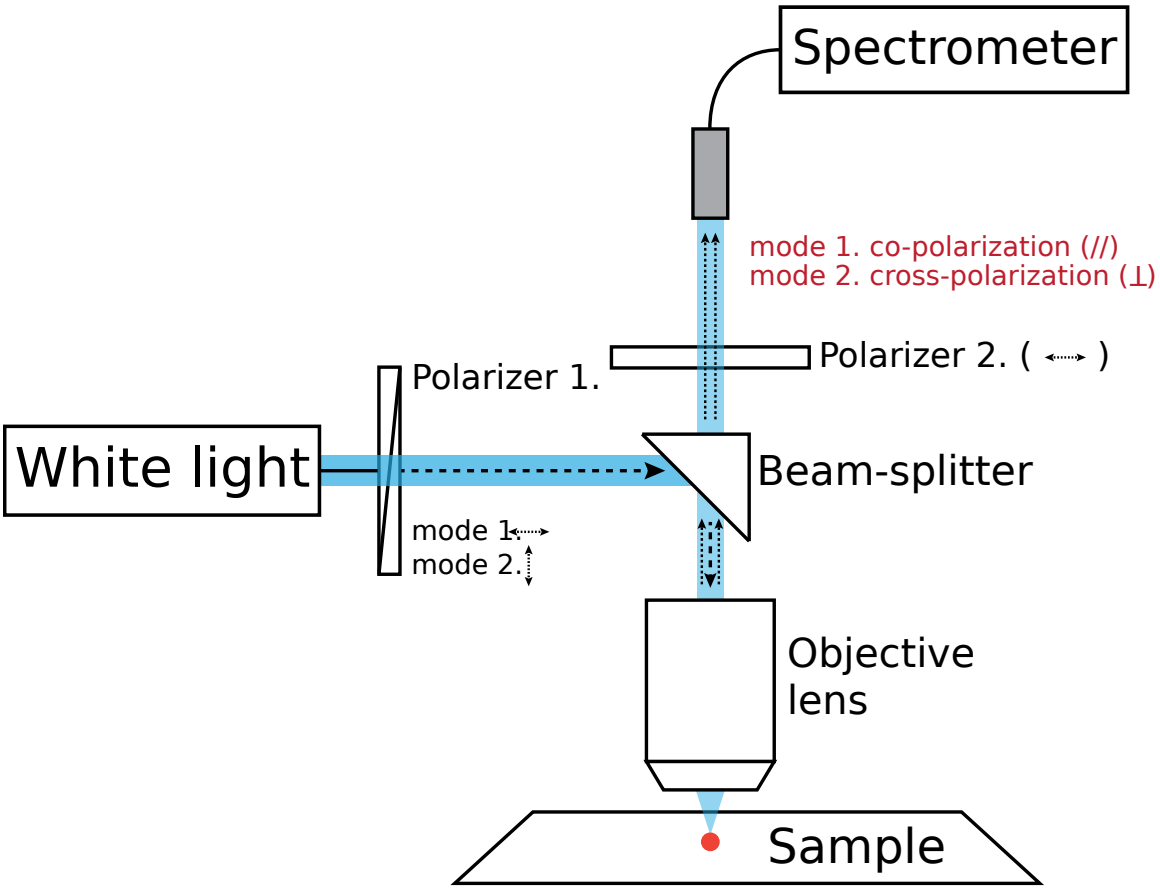

Figure 4.3: A schematic illustration of our spectrometry setup for measuring the co-polarized and cross-polarized reflection spectra of the photonic microcapsules.

it is even less than one; as we have already discussed, for particles larger than ∼240 nm the second-order form factor resonances can be much stronger than the structure factor resonances and prevent entirely structural color of longer wavelengths. Using smaller scatterers, we have demonstrated a way to blueshift the second-order form factor resonances away from the visible spectrum and thus to decrease their effect on structural color: for a $d = 156$ nm polystyrene particle in this system, the second-order form factor resonance occurs at 305 nm, and only the much weaker first-order form factor resonance is within the visible.

We isolate the contribution of multiply scattered light to the background scattering by measuring the polarization dependence of the reflection spectra, since multiply scattered light loses memory of its original polarization. We linearly polarize the incident light and place another linear polarizer in front of the detector, as shown in Figure 4.3. The resulting spectra, shown in Figure 4.2(d), are very different. When the two polarizers are parallel, we observe a single spectral peak at approximately 560 nm for the green and 600 nm for the red microcapsules; whereas when the two polarizers are crossed the spectra for both samples are nearly flat. From these measurements we calculate the ratio of singly to multiply scattered light at the resonant wavelength, assuming that the cross-polarized signal is due to multiple scattering and that the contribution of multiple scattering to the signal is the same in both the co- and cross-polarized spectra. We find values of 16.2 for the green and 17.3 for the red microcapsules, indicating that multiple scattering does not contribute significantly to the color. We also calculate the contribution of multiple scattering to the background from the average reflectivity through crossed (I_{crossed}) and parallel (I_{parallel}) polarizers at short wavelengths (420-435 nm), $I_{\text{crossed}}/(I_{\text{crossed}} + I_{\text{parallel}})$. We find that multiple scattering accounts for only 23% of the background intensity in green and 24% in red microcapsules, indicating that the primary source of background scattering is single-particle scattering from the polystyrene cores. From these measurements we conclude that multiple scattering does not compromise the color saturation in our system, in contrast to other systems with isotropic structural colors where multiple scattering has to be suppressed through absorption [22, 16, 58, 59, 60].

To complete the color spectrum, we make microcapsules from core-shell particles

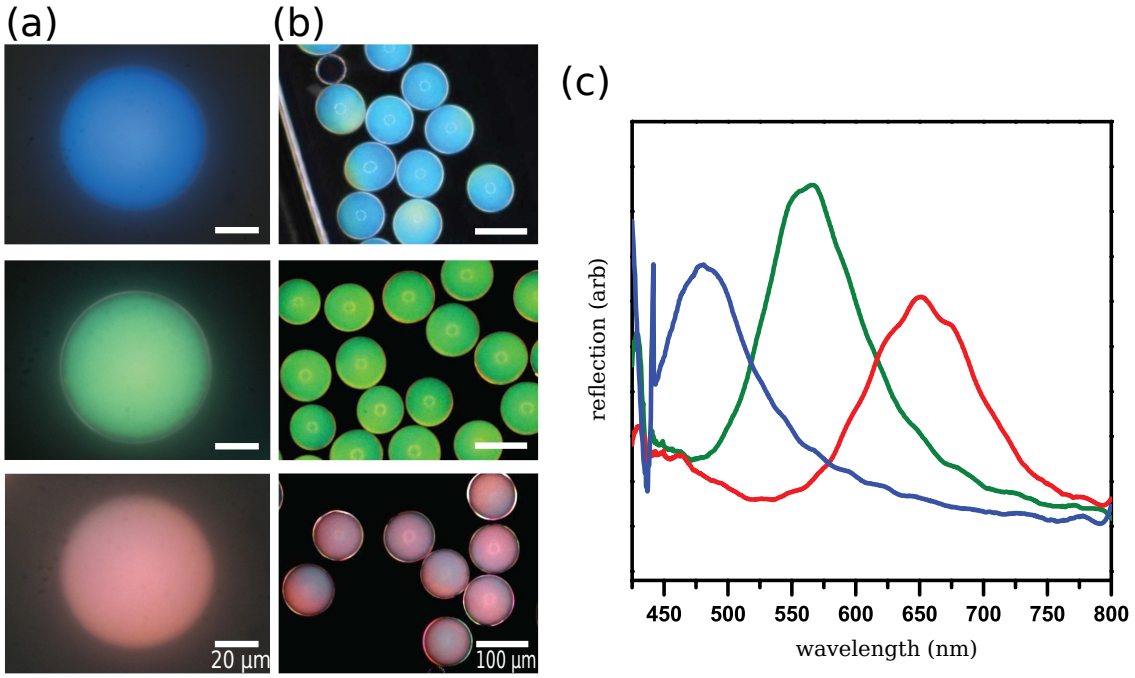

Figure 4.4: Photonic microcapsules with blue, green, and red structural colors prepared with different shell thicknesses of coreshell particles. a) Bright-field (reflection) and b) dark-field (reflection) optical micrographs of photonic microcapsules. c) Reflectance spectra of the microcapsules. All droplets are incubated at 440 mOsm/L for one hour before ETPTA polymerization.

of different sizes. We use the same osmotic compression and cores for all samples, so that the inter-scatterer distance is controlled by the thickness of the particle shells. We obtain blue photonic microcapsules with $R_{\mathrm{h,core-shell}} = 135 \pm 24$ nm, green with $R_{\mathrm{h,core-shell}} = 168 \pm 17$ nm, and red with $R_{\mathrm{h,core-shell}} = 210 \pm 15$ nm, as shown in Figure 4.4.

The optical properties of our amorphous microcapsules are qualitatively different from those of crystalline structures, even for samples prepared with comparable particle sizes. For comparison, we prepare crystalline photonic balls with a diameter of about 90 μm through consolidation of 250 nm polystyrene spheres in W/O droplets [61]. Reflection optical micrographs in Figure 4.5(a) and (b) show the dramatic differences between the two samples: the amorphous microcapsules show colors that are uniform across each capsule and from capsule to capsule, whereas the crystalline balls show patches of different colors and variations between balls. To quantify these differences, we measure the spectra of single microcapsules and crystalline balls as a function of position (x) with our microscope-mounted, fiber-optic spectrometer (Figure 4.5(c)). The position of the spectral peak remains constant for the microcapsule (Figure 4.5(d)), while in the crystalline ball it shifts by 40 nm or more (Figure 4.5(e)). This behavior arises from the anisotropy of the crystal, which leads to a variation in the resonant condition with angle. At the same time, the incompatibility of crystalline order with the spherical symmetry of the droplet likely leads to the formation of grain boundaries, which could account for the variation in colors from ball to ball. Our measurements highlight the trade-off in optical performance between crystalline and isotropic structures: while the crystalline ball has sharper

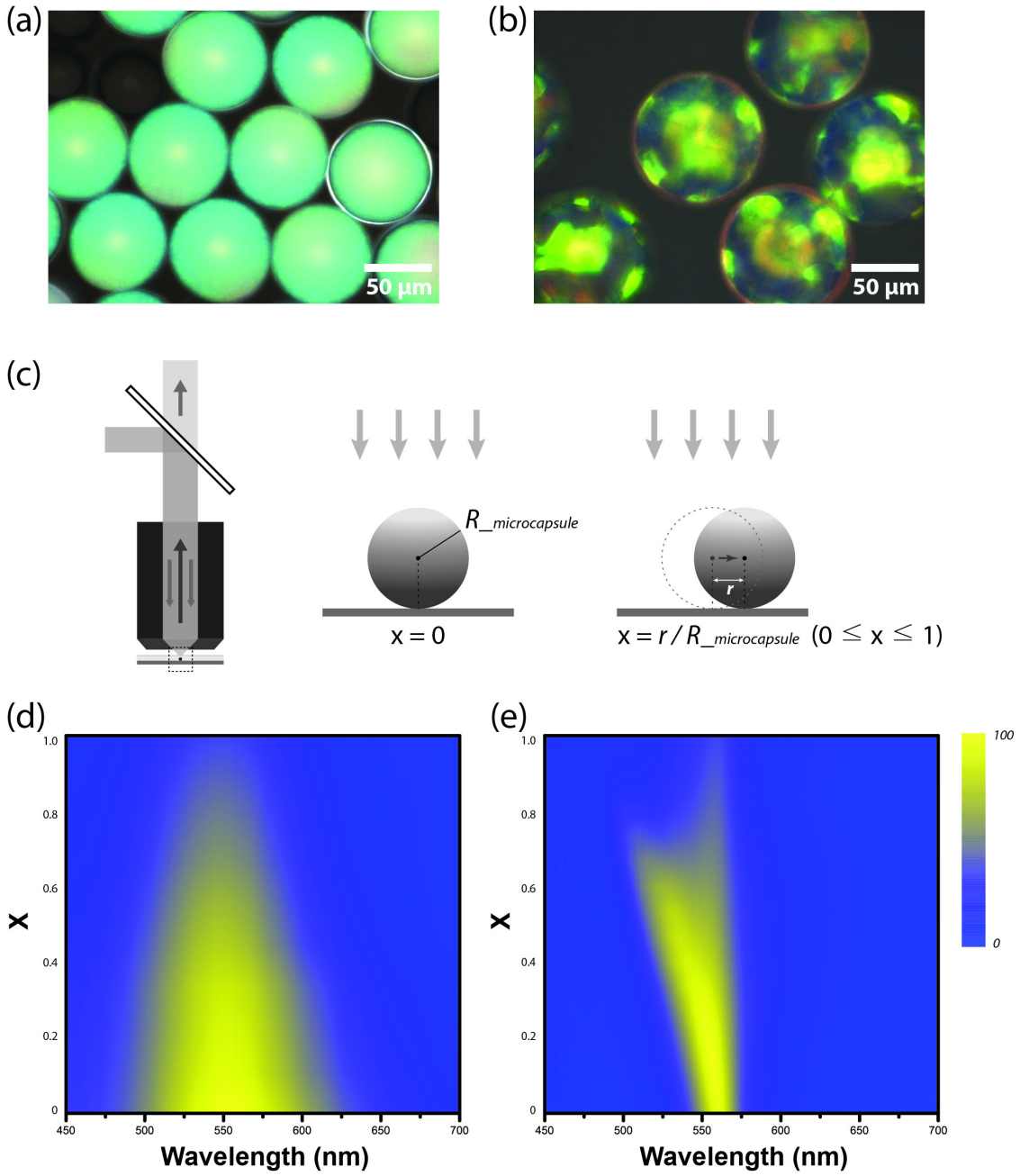

Figure 4.5: Photonic microcapsules show uniform structural colors under different illumination directions. Bright-field (reflection) optical micrographs of (a) photonic microcapsules and (b) crystalline balls. (c) Schematic of the apparatus used to measure the reflection spectra of a single microcapsule or ball. (d,e) Reflectivity (yellow: 100%, blue: 0%) of a microcapsule (d) and a crystalline ball (e) as a function of position (x), where x=0 at the center and x=1 at the edge.

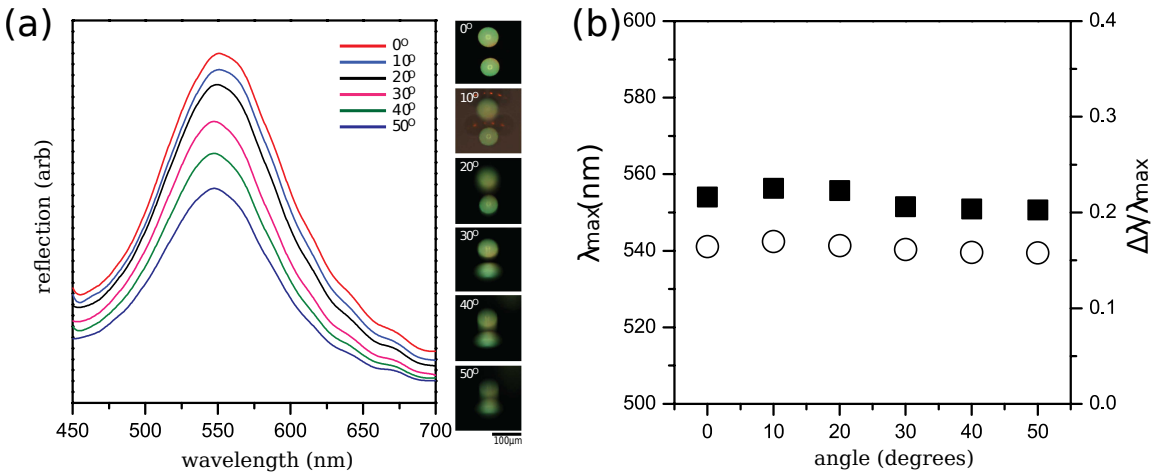

Figure 4.6: (a) Reflectance spectra of the photonic pigments at various viewing angles. (b) Peak position ($\lambda_{\max}$, dark squares) and normalized full-width at half-maximum ($\Delta\lambda/\lambda_{\max}$, open circles) of each peak at various angles. In this measurement we varied the angles of the sample stage with respect to the normal to the substrate.

resonant peaks at some locations, the isotropic microcapsule shows a broader but more consistent peak across a wide range of positions. We also measure the reflectivity of the microcapsules at various angles by rotating the sample stage. As shown in Figure 4.6, the peak moves less than 10 nm and is independent of the viewing angle. Plots of as a function of angle in Figure 4.6 confirm that the optical properties of our microcapsules are independent of orientation.

In conclusion, we have demonstrated a new colloidal assembly method to fabricate photonic microcapsules with non-iridescent structural colors that cover the entire visible range. The length scales of our system are such that both single-particle and multiple scattering is suppressed, so that resonant scattering from the inter-particle correlations is the dominant process determining color. In this way, this design has enabled the creation of structural colors that were inaccessible with conventional colloidal particles. We note that this system is optimized for structural inks that

remain in a fluid medium. Pigments than can be dried might be made using a more rigid microcapsule. Another challenge is to further increase the saturation across the visible range; as our experiments show, red microcapsules are not as saturated as green or blue ones due to scattering at short wavelengths. Our system provides several potential ways to reduce incoherent scattering; for example, one could vary the refractive indices of the core and shell, or optimize the ratio of the core size to the inter-particle spacing. The ability to independently tune refractive indices and length scales to optimize the color – all while maintaining the ability to form amorphous packings – make this a promising system for mass-produced photonic pigments.

This chapter is based on the following publication: Jin-Gyu Park, Shin-Hyun Kim, Sofia Magkiriadou, Tae Min Choi, Young-Seok Kim, and Vinothan N. Manoharan, "Full-spectrum photonic pigments with non-iridescent structural colors through colloidal assembly," Angewandte Chemie, 126(11):29432947, 2014 [42].

Chapter 5

Inverse Glasses

5.1 Introduction

In this chapter we describe a different approach to angle-independent red structural color, based on *inverse* glasses: colloidal glasses where the refractive index of the scatterers is lower than the refractive index of the medium. As we have discussed in Chapter 3, in this type of system it should be possible to protect the long-wavelength resonances of the structure factor from the short-wavelength resonances of the form factor by blueshifting the resonances of the form factor into the ultra-violet, leading to photonic glasses with pronounced scattering at long wavelengths and red structural color.

To guide our experiments, we first estimate the optimal value for the refractive index contrast, $m = n_{\text{scatterer}}/n_{\text{medium}}$, for which the intensity of unwanted scattering at short wavelengths is minimal within the visible regime. We find that the requirement that a structure be inverse is not sufficient, and that there is only a narrow

range of values for m for which red structural color might be possible. While this range is difficult to achieve, we report on our progress towards the realization of photonic glasses where the refractive index contrast is closer to this optimum than in the more conventional glasses we have discussed so far. We make these new, inverse glasses following two different methods: infiltration of conventional glasses with high-index media, and calcination of polystyrene-in-silica colloidal glasses to make air-in-silica structures. We observe weak red structural color in one of our infiltrated samples. However, there are also significant deviations between theory and experiment: in our infiltrated samples we observe additional scattering peaks in the blue, and in our calcinated samples we systematically over-estimate the primary scattering resonances. We conclude that the infiltration approach is a promising route towards angle-independent red structural color, and we suggest further studies to understand the differences between theory and experiment and to evaluate the potential of calcinated structures.

5.2 Theory

To estimate the optimal value for the refractive index contrast that minimizes the intensity of the short-wavelength form factor peaks, we focus on scattering into the backscattering hemisphere and we calculate a "reflection" cross section for various values of m:

$$\sigma_{\text{reflection}} = 1/k^2 \int_{\phi=0}^{2\pi} \int_{\theta=\pi/2}^{\pi} FS \sin\theta \, d\theta \, d\phi. \tag{5.1}$$

This expression for $\sigma_{\text{reflection}}$ is the same as Equation 3.5, except here we omit the Fresnel transmission coefficient at the sample – air interface, $T_{\text{s-a}}$, for simplicity:

its exact value, in the 0.8–0.95 range, depends on the materials at the interface of the colloidal glass, and we do not wish to restrict our search to a particular system. This omission may lead to an overestimation of the width and intensity of all the scattering peaks, since now there is no cutoff in the scattering angle θ from total internal reflection. However, it should affect all peaks in a similar way, so we do not expect it to alter the qualitative conclusions of this calculation.

Figure 5.1(a) shows the reflection cross-section for various m as a function of a dimensionless size parameter for the scatterers, $kd = 2\pi n_{\text{medium}} d/\lambda$, where n_{medium} is the refractive index of the medium, d is the scatterer diameter, and we have assumed $\phi = 0.5$ for the structure factor. These theoretical curves are similar to the master data curve we encountered in Figure 3.6 of Chapter 3: given a value for m, each curve can be rescaled with the particle size and medium index to describe the reflection cross-section as a function of wavelength for any system. Since we are interested in finding the optimal values for red color, we have marked with a blue dashed line the kd value that corresponds to 400 nm if the resonance of the structure factor is at 650 nm. Of all the calculated curves, we see that only one describes a system that scatters significantly more in the red than in the blue, for $m = 0.7$.

What is so special about this refractive index contrast that minimizes scattering at short wavelengths? To gain further insight into the scattering behavior of these inverse glasses, we compare our calculation for the reflection cross section to two similar calculations, where in one we include only the form factor, shown in Figure 5.1(b), and in the other we include only the structure factor, shown in Figure 5.1(c). From the calculation that only includes the structure factor, we immediately see that the

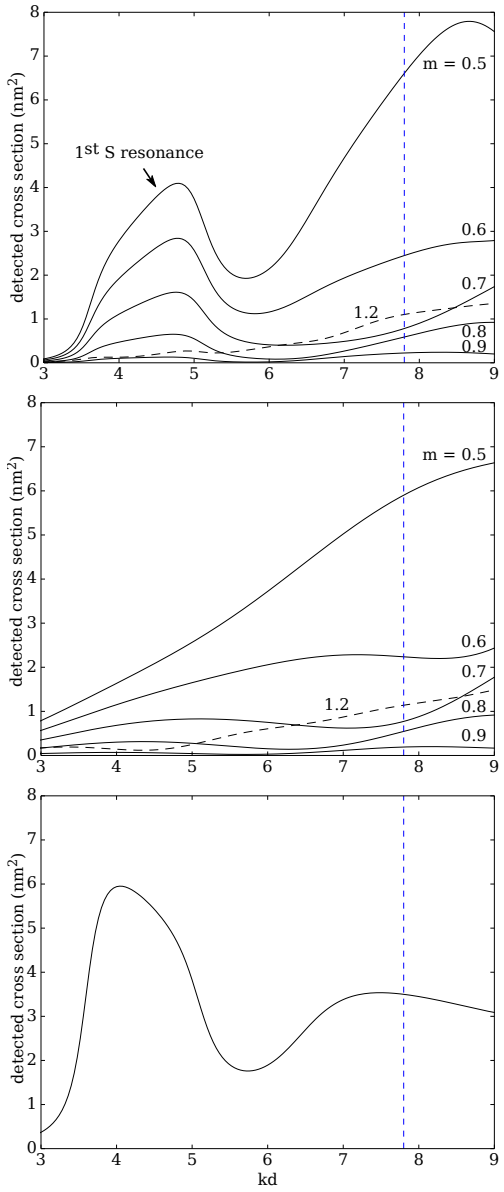

Figure 5.1: There is an optimal value for the refractive index contrast, $m \sim 0.7$, for which the resonances of the structure factor dominate scattering. (a) Reflection cross section as a function of kd, for various values of m, including both the form and the structure factor, (b) only the form factor, (c) only the structure factor. By inspection, we see that, in the full calculation shown in (a), the resonance at $x =\sim 4.8$ comes from the first resonance of the structure factor, while the resonances at higher x come from a combination of resonances of the structure and of the form factor. The vertical dashed blue line corresponds to 400 nm if the resonance of the structure factor is at 650 nm, chosen for red color. For comparison, we also show the curves for $m = 1.2$, corresponding to a typical glass of colloidal particles.

structure factor itself can contribute a lot of scattering in the blue when its first resonance is in the red. For $m > 0.7$, this second resonance of the structure factor is boosted by the familiar second-order resonance of the form factor that we have encountered in conventional glasses – for comparison, we show a representative (dashed) curve for these with $m = 1.2$. For $m < 0.7$, the second-order form factor resonances at high kd are replaced by the *first*-order form factor resonances, leading, again, to pronounced scattering at short wavelengths. However, at $m = 0.7$ there is a sweet spot: the second resonance of the structure factor overlaps with a local minimum of the form factor, resulting in a reduced magnitude for the reflection cross section at short wavelengths.

To make a colloidal glass with this optimal value for $m \sim 0.7$, we need to find an appropriate combination of materials for the scatterers and their medium. This is not a trivial task: for scatterers with the lowest possible refractive index, $n_s = 1$, the effective refractive index of the medium needs to be $n_{\text{eff}} = 1/0.7 = 1.43$. For a colloidal glass of spheres with volume fraction $\phi = 0.55$, and if we assume the Maxwell-Garnett approximation for the effective index of the medium (Equation 3.2), this requires a medium with index $n_{\text{medium}} = 1.93$ – a high value that is only accessible with a handful of materials. This value can be lower in a system of core-shell particles with shells that are made of the same material as the medium, because there the volume fraction of air can be decreased substantially by a factor of $(d_{\text{core}}/d_{\text{shell}})^3$.

Regardless, we can test the validity of this prediction with inverse glasses that have different values for m than the optimum of 0.7, by comparing their spectra to our model. In what follows, we describe our observations on three systems with

$m = 0.65$ (poly-methylmethacrylate in high-index oil), $m = 0.68$ (silica in high-index oil) and $m = 0.85$ (air in silica).

5.3 Experiments

To make inverse glasses we follow two different approaches. The first approach is based on conventional colloidal glasses that are inflitrated with oils of high refractive index. The second approach is based on solid foam-like structures, where the scatterers are air cavities in a silica matrix.

5.3.1 Infiltration of Colloidal Glasses with High-Refractive Index Oils

For our infiltration experiments, we first assemble two types of colloidal glasses, one of poly-methylmethacrylate particles and one of silica particles. In the poly-methylmethacrylate glasses we use particles with diameter $d = 240$ nm and we follow the protocol described in Chapter 3. In the silica glasses we use particles with diameter $d = 250$ nm; we start with an aqueous suspension at 33 % w/w, we mix in a small amount of carbon black (about 1:30 carbon black:silica by mass), centrifuge the mixture at 2,000 g for 10 minutes, condense to about 45 % w/w and deposit the suspension on a gypsum substrate to dry at room temperature. We then infiltrate both types of glasses with refractive index oils that have indices ranging from $n_{\text{oil}} = 1.48$ to $n_{\text{oil}} = 1.6$ (Cargille Refractive Index Liquids, Series A). Two representative samples are shown in the insets of Figure 5.2.

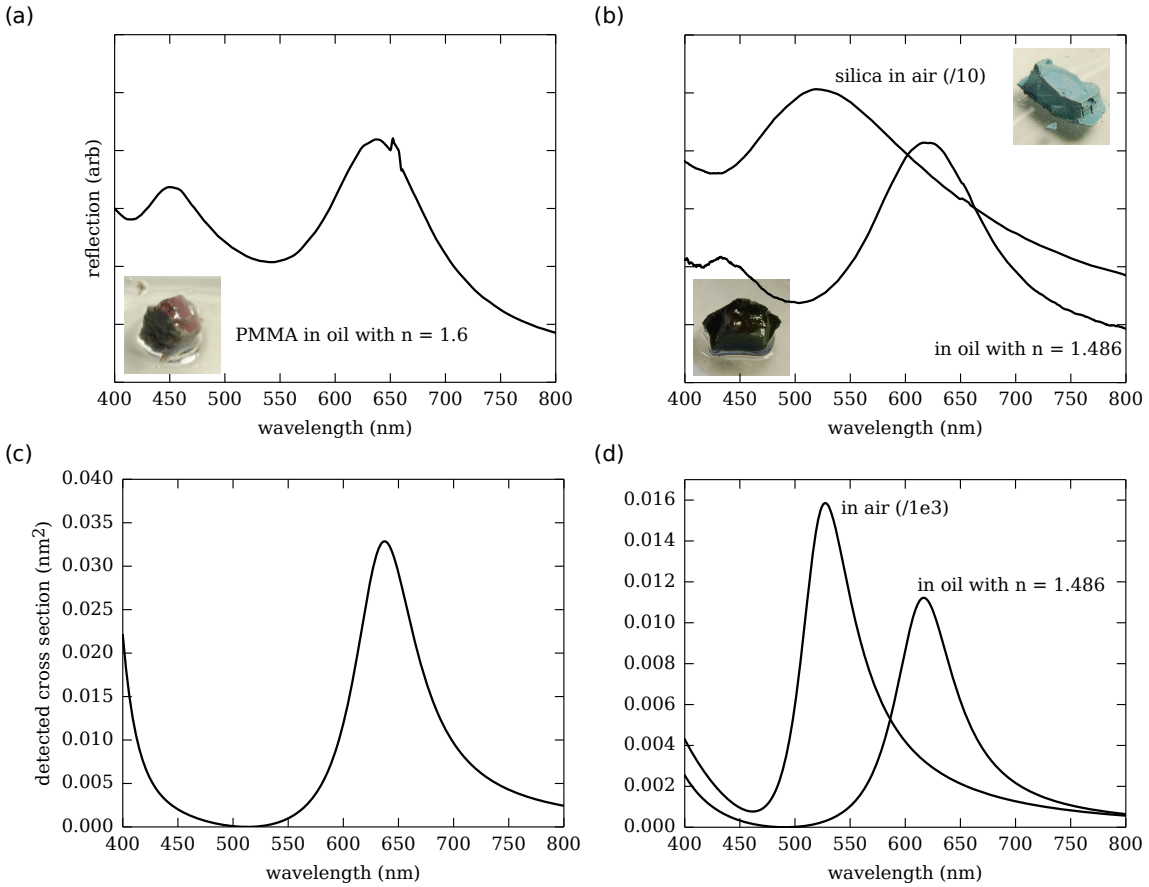

Figure 5.2: Inverse glasses made of colloidal particles immersed in high-index oils can have weak, red structural color; however their spectra have short-wavelength features that our model does not predict. (a) Reflection spectrum of a glass of PMMA particles with diameter $d = 240$ nm, infiltrated with an oil of refractive index $n_{\text{medium}} = 1.6$ (shown in the inset). (b) Reflection spectrum of a glass of silica particles with diameter $d = 250$ nm, before and after infiltration with an oil of refractive index $n_{\text{medium}} = 1.486$ (shown in the inset). (c) Calculated cross section for the system in (a) for near backscattering, with $170 < \theta < 180$ degrees. The cross section has a peak that matches the data for $d = 246$ nm, but no other peak at shorter wavelengths. (d) Calculated cross-section for the system in (b) for near backscattering, with $170 < \theta < 180$ degrees, before and after inflitration. The peaks of the cross sections match the data for $d = 242$ nm, but, again, our theory does not predict another visible peak at short wavelengths.

5.3.2 Air Cavities in a Silica Matrix

Our method for making inverse colloidal glasses of air cavities inside a silica matrix is based on a protocol developed by Hatton et al. for the assembly of large area, crack-free inverse opals [62]. Briefly, we mix an aqueous binary suspension containing equal numbers of polystyrene particles of two different sizes with a solution of silica precursor containing hydrocloric acid, ethanol, and tetraethylorthosilicate (TEOS). We then immerse a silica wafer in the suspension and let the solvent evaporate slowly at 65°C for two days. During this time, two processes take place: the colloidal particles form a thin film on the wafer, driven by capillary forces, and the ingredients of the silica precursor solution react to yield silica. At the end of this slow bake we retrieve polystyrene-in-silica colloidal glasses. We then calcine these at 500°C for two hours to burn the polystyrene. The final result is a glassy packing of air cavities inside a continuous silica matrix, as revealed by the SEM images shown in Figure 5.3(a–b). The use of two different particle sizes in this process is essential for preventing crystallization [63, 16] because the template assembly is very slow – unlike the protocols we have so far described that are based on fast centrifugation, where the timescale for assembly is too fast for the particles to crystallize and we therefore can use monodisperse suspensions. We have included a more detailed protocol in Appendix A.

The structures we obtain are isotropic with short-range order, as we see from the ring patterns in the power spectra of their scanning electron microscope images in Figure 5.3(c–d). We calculate the characteristic lengthscales of order, a, from the location of the maxima of the azimuthal average of the power spectra, q_o: $a = 2\pi/q_o$.

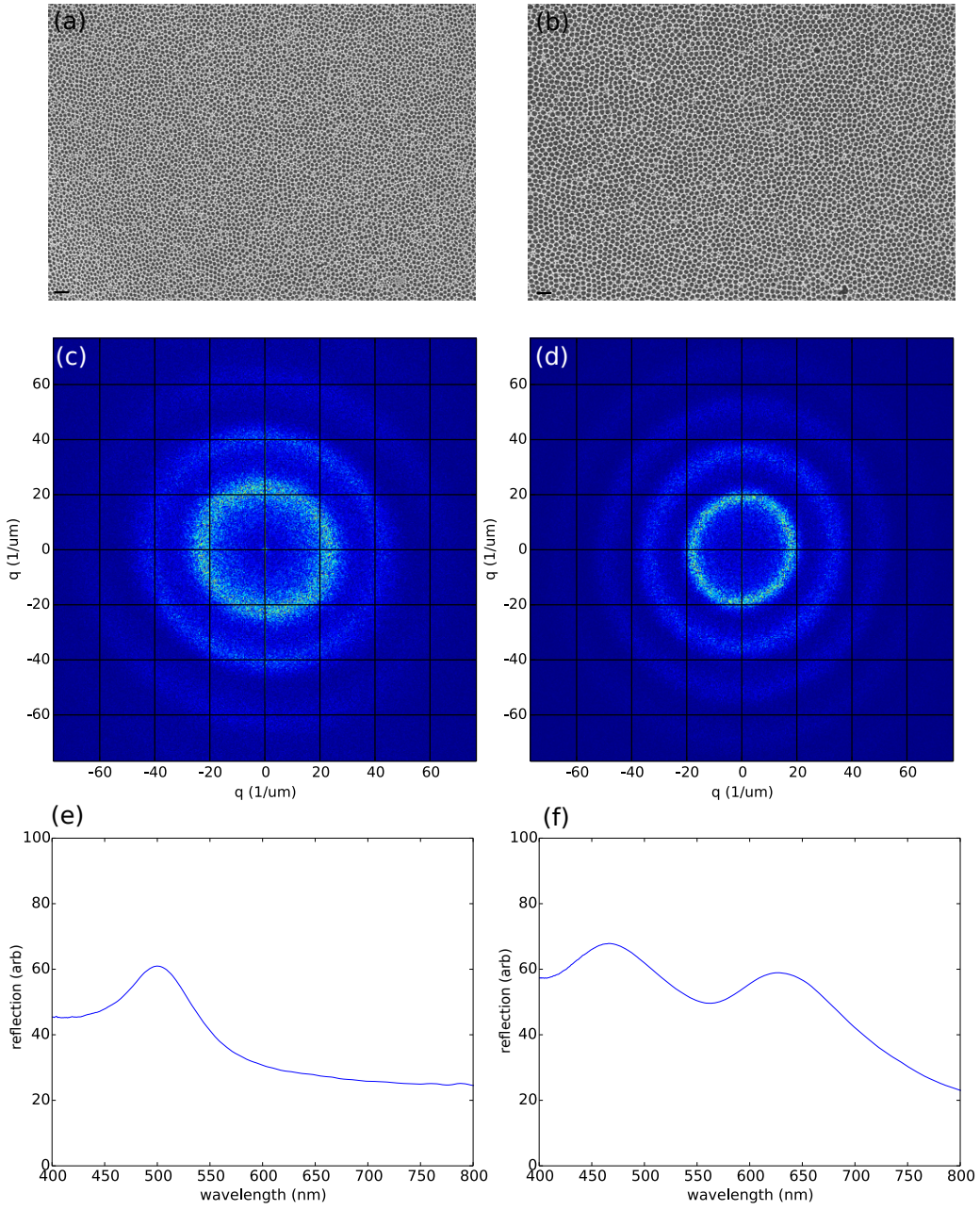

Figure 5.3: Our calcination method for making inverse glasses is succesful in yielding glassy packings of air spheres, with short-range order and long range disorder; SEM images courtesy of Nicolas Vogel.

In our experiments we can control this lengthscale using different particle sizes in the template. For instance, for the sample shown in Figure 5.3(a) we use a mixture of 180 nm and 336 nm spheres, resulting in characteristic lengthscales of 154 nm and 278 nm; and for the sample shown in Figure 5.3(b) we use a mixture of 180 nm and 408 nm spheres, resulting in characteristic lengthscales of 183 nm and 339 nm. We omit discussion of the lengthscales associated with larger q-values, because those would correspond to wavelengths much below the visible spectrum. Note that to obtain glassy structures it is important that the particle sizes not be too different, otherwise crystals may still form. This is arguably the case already in the sample shown in Figure 5.3(b), where small crystalline domains can be seen; at the time of this experiment, we were limited in the choice of particle sizes we had at hand. In one occasion we observed an extensive square lattice in a sample made of 180 nm and 450 nm spheres – most likely because the smaller particles can fit in the interstices of the square lattice formed by the larger ones.

5.3.3 Spectrometry

We measure the spectra of all our glasses with a fiber-coupled spectrometer. We use a bifurcated fiber that contains two concentric waveguides, one for illumination and one for collection of reflected light near the backscattering direction (OceanOptics R400-7-VIS/NIR). We illuminate the samples with a halogen lamp (OceanOptics DH-2000) and we detect the scattered light with a spectrometer (OceanOptics HR2000+). We normalize the signal to the reflection from a white standard (Labsphere SRS-99-010); note that this is a Lambertian surface that reflects light in all directions, and

so these reflection measurements are not absolute. To avoid thin-film interference in our calcinated glasses, we measure their spectra after we pulverize them by hitting them with the flat end of a wooden stick and we glue the powder on carbon tape.

5.4 Results and Discussion

5.4.1 Infiltrated Colloidal Glasses

The spectra of our infiltrated glasses, shown in Figure 5.2(a–b), have a global maximum at wavelengths corresponding to orange or red, indicating that we have succeeded in suppressing scattering at short wavelengths. However, there are also additional – albeit weaker – reflection peaks in the blue. The glass of poly-methylmethacrylate particles in an oil with n =1.6 has a weak red color and a corresponding peak in reflection at 620 nm, but also a weaker peak at 450 nm. The glass of silica particles in an oil with $n = 1.486$ looks almost black, since the silica is now closely index-matched to the medium, revealing the carbon black. Even so, its reflection spectrum has a peak at 640 nm and a weaker one at $\sim$ 440 nm. We also show a photograph and a spectrum of a similar but unfiltrated silica sample: it has a light blue color and a corresponding reflection peak at 523 nm.

The blue peaks of the infiltrated samples cannot be explained with our model. According to Figure 5.1, there may still be increased scattering at short wavelengths for $m = 0.65, 0.68 < 0.7$; however the peaks we observe are much more narrow than the ones we might expect theoretically. To demonstrate this discrepancy more clearly, we calculate the "detected" scattering cross-section for these glasses, namely

the scattering cross section near backscattering with $170° < \theta < 180°$ in Equation 3.5. The results are shown in Figure 5.2(c–d), where we use a volume fraction $\phi = 0.55$. In all cases, we can reproduce the primary scattering peaks using parameters that are consistent with our experiments: we obtain best agreement using a particle diameter $d = 246$ nm for the 240-nm poly-methylmethacrylate glass and a particle diameter $d = 242$ nm for the 250-nm silica glass, both for the infiltrated and the uninfiltrated case. However, our model does not predict any additional peaks in the blue for either one of these samples.

This difference between theory and experiment can either be because the assumptions of our model are not valid, or because there are imperfections in the samples. The main assumption of our model is single scattering. In Chapter 3, we saw that this can lead to underestimating reflectivity at shorter wavelengths. However, we would expect features due to multiple scattering to be broad, since they arise from an incoherent process; here, the peaks we observe are fairly well-defined and narrow. Therefore, we speculate that our short-wavelength peaks are due to imperfections in the samples. After infiltration, the refractive index difference between the particles and the medium is much smaller than in any samples we have previously studied. This means that the scattering length is now much longer: light traverses a longer distance before it scatters or is absorbed. As a result, light can probe a larger volume of the samples, and their scattering properties are more susceptible to inhomogeneities. For instance, if there is a crystallite inside a sample, it can contribute a Bragg peak at any wavelength that is shorter than the resonance of the structure factor, depending on its orientation. Whether this is the case here can be resolved in future experiments that

check the repeatability of these blue peaks and measure their angular dependence.

We note that this increase in scattering length may also have contributed to the suppression of scattering in the blue. As the next step of this study, it will be important to compare these samples to samples with less carbon black, where the optical thickness – and thus the amount of multiple scattering – is comparable to that of our conventional glasses. This is a necessary control experiment to check that having an inverted refractive index contrast can indeed lead to reduced scattering at short wavelengths, as predicted.

5.4.2 Air Cavities in a Silica Matrix

The spectra of our samples, shown in Figures 5.3(e–f), correlate qualitatively with the underlying structures. Both samples show a tendency for increased scattering at short wavelengths. The glass made of smaller particles in the template has a scattering peak at 515 nm; the glass made of larger particles has a scattering peak at a longer wavelength, at 632 nm, but also a stronger peak at 421 nm.

The increased scattering at short wavelengths is consistent with our calculation for the reflection cross section of a glass with $m = 0.9$, shown in Figure 5.1(a). However, the locations of the resonances are far from what we would expect based on our analysis of the underlying structures. To estimate the resonant wavelengths predicted by our model, we assume single scattering and we use the characteristic lengthscales that we extract from the power spectra into Equation 1.10 with $\theta = 180°$: $\lambda = 2n_{\text{eff}}a\sin(\theta/2)$. We treat the samples as packings of air spheres in silica where the interparticle spacing is the lengthscale that we extract from the power spectra,

we assume the volume fraction of a random close packing, $\phi = 0.65$, and we calculate the effective medium index $n_{\text{eff}} = 1.13$ with the Maxwell-Garnett approximation (Equation 3.2) using a refractive index for silica $n_{\text{silica}} = 1.38$, as measured from the reflection spectra of inverse opals made in the same way by Phillips et al. [64]. From this calculation we expect, within the visible regime, a resonance at 630 nm for the sample in (e) and two resonances, at 466 nm and at 768 nm, for the sample in (f). Interestingly, for two of our data points we overestimate the resonant wavelengths by a constant amount: $630/515 = 768/632 = 1.22$. This suggests a systematic error in our analysis, although the same error cannot account for the discrepancy concerning the resonance at 466 nm of the second sample, which our prediction underestimates. In what follows, we discuss where these differences might originate.

A very likely source of systematic error is in our analysis of the structures. We assume that our two-dimensional images are representative of our three-dimensional structures. However, the samples may not be uniform. Heterogeneities may arise during calcination, while water evaporates and the structure shrinks, because one side of the sample is adhered to a silicon substrate. This may lead to a compression in the direction perpendicular to the substrate, because the adhered side of the structure is constrained from shrinking parallel to the substrate. This phenomenon has been exploited to tune anisotropy in similarly made inverse opals [65]. There, asymmetries of $\sim 30 - 50\%$ were observed in samples made similarly to ours[1]. Furthermore, we expect this anisotropy to be more pronounced close to the substrate, meaning that there may be a gradual change in characteristic lengthscale with depth. Our two-

[1]See points corresponding to 500°C in Figure 1B of [65].

dimensional images cannot reveal such asymmetries, and this may well accont for our systematic error of 20%. A three-dimensional analysis of our structures, for instance using a focused ion beam to sequentially expose and image layers deeper within them, could elucidate whether this is the source of error.

Moreover, the air cavities are not always complete spheres. A closer look, as shown in the inset of Figure 5.4, reveals spherical cavities that intersect: The structure is more accurately described as a bi-continuous packing of *overlapping* air spheres in silica. This may have lead to an overestimation of the effective refractive index, n_{eff}, and consequently of the resonant wavelength. In our calculation of n_{eff}, we used the maximum possible volume fraction of spheres in a random close packing, $\phi_{\text{rcp}} = 0.65$, leading to $n_{\text{eff}} = 1.19$. However, the fact that we have overlapping spheres means that the volume fraction of air can exceed ϕ_{rcp} and the effective refractive index can be lower, leading to a predicted wavelength that is closer to what we measure – at least for two of our three data points. This error alone is not sufficient to account for our systematic of 22%: this would require $n_{\text{eff}} \sim 1.19/1.22 <\sim 1$, which is unphysical. However, it could certainly contribute, in combination with the effects discussed above. In a future study, the volume fraction of air can be estimated from the scanning electron microscopy images, by measuring the diameter of the tunnels that connect the spherical cavities. Once the degree of sphere overlap is known, the volume fraction can be easily estimated: In Figure 5.4 we show the volume fraction of a glass of overlapping spheres (x-axis), as a function of the overlap (y-axis), obtained from numerical simulations of packings of overlapping spheres.

None of these effects can explain the deviation between our estimate and mea-

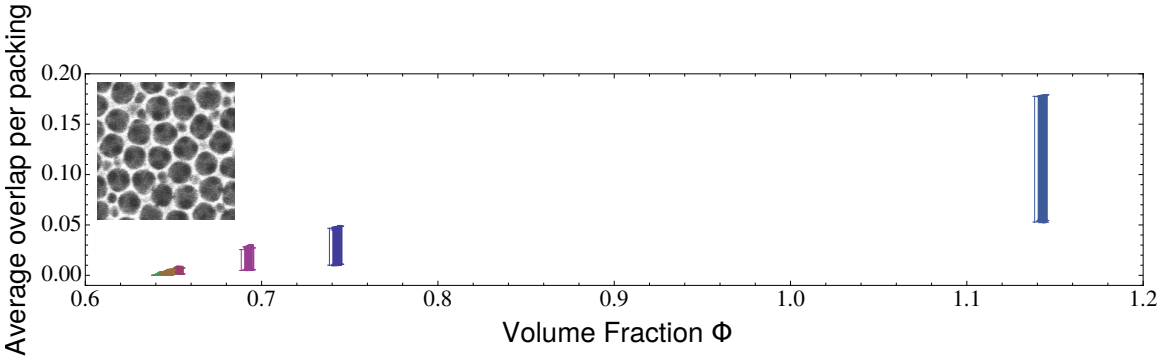

Figure 5.4: The volume fraction can exceed the random close packing limit of $\phi_{\mathrm{rcp}} = 0.65$ in a random packing of spheres that are allowed to overlap, as is the case in our samples (see inset). Here the overlap is defined as the difference between the distance of the centers of touching particles and the sum of their radii. Volume fraction (x axis) versus average overlap (y-axis) in simulated glassy packings of spheres with bidispersity 1:1.2. For each volume fraction there are 100 different realizations of packings. The error bars are the standard deviation of overlaps within a single packing. Simulation courtesy of Zorana Zeravcic.

surement of the short-wavelength peak in the sample made of larger spheres. We speculate that this peak is due to resonant scattering of light from clusters of cavities made by the smaller particles alone. As discussed, this sample was made using two very different sphere sizes. The big size difference between the two particle types may have lead them phase-segregate during assembly, leading to patches of short-ranged order with different characteristic lengthscales. A study of the Fourier spectra of more images, that capture a larger area, could help characterize the density of these phase-segregated areas and estimate their contribution to the scattering properties of the sample.

5.5 Conclusion

Our calculations indicate that, to make a photonic glass that scatters predominantly at long wavelengths, the refractive index contrast needs to be within a narrow range of values in the vicinity of 0.7, so that the second resonance of the structure factor can be mitigated by a minimum of the form factor. This requirement is more stringent than our original proposal, which simply suggested a refractive index contrast that is less than one. We have demonstrated two ways to make inverse glasses: infiltration of conventional colloidal glasses with higher index media, and calcination of glasses of polymer particles in a silica precursor to make air-in-silica structures. The preliminary results of our infiltration studies are encouraging: one of our samples has a weak red color, and all of them scatter predominantly at long wavelengths. However, there are significant deviations between theory and data in all of our inverse glasses. Our infiltrated samples have unexpected blue peaks, while most of the scattering peaks of our calcinated samples deviate systematically from our expectations. Further studies are required to elucidate the origin of these deviations.

Future experiments should also focus on core-shell inverse structures, where the colloidal particles have a low-index core and a high-index shell that can be index-matched to the medium. In these systems, the ability to control the resonances of the form factor via the diameter of the scattering core should allow more flexibility in the choice of refractive indices.

This work was done in close collaboration with Nicolas Vogel, who provided the protocol, most ingredients and samples, and many ideas. We are also grateful to Zorana Zeravcic for the numerical simulation of packings of overlapping spheres, and

to W. Benjamin Rogers and Nicholas B. Schade for stimulating conversations.

Chapter 6

Towards Design Rules for Photonic Glasses as Pigments

6.1 Introduction

While the academic study of the optical properties of colloidal photonic glasses is intellectually interesting, we hope that our findings can also contribute to practical applications. Structural colors can offer new capabilities that are not accessible with conventional pigments. The most durable pigments we know are based on inorganic materials such as aluminum, iron, lead, chromium, zinc, cadmium or arsenic, many of which are severely toxic [66]. Organic pigments are often much safer, and some are even consumable, however they are often susceptible to bleaching. Pigments that are both durable and safe to use are the subject of ongoing investigation [67, 66].

Structural colors can provide a resolution to this search, as they can be both long-lasting and non-toxic. Because these colors originate primarily from their nanostruc-

ture, and not from their chemical composition, it is possible to choose their constituent materials based both on safety and stability. Nature has proved this already: a visit to a natural history museum with old bird specimens is sufficient to notice that blue colors, that come from nanostructures within bird feathers, tend to be much more vivid than yellow, orange, or red colors, that come from organic pigments [6]. Even older than these is the brilliant blue of fifty-million-year old beetle fossils found in Messel, Germany, whose photonic structures have been preserved [68] – although in this case it has been argued that some changes in chemical composition have lead to a blueshift in color [69].

Furthermore, this decoupling of appearance from chemistry makes structural colors very versatile. It means that the same visual effect can be achieved with different combinations of materials, and that the materials can be chosen depending on the application – as long as the refractive index contrast between the scatterers and the medium falls within a certain range, as we have discussed in Chapters 3,5. For instance, if the goal is to make a colored coating, the photonic glass can be a spreadable polymer with scatterers embedded within, or even molded on the surface of the material itself as is already done with photonic crystals; if, instead, the goal is electronic ink for a reflective display, it may be desirable to have encapsulated suspensions of color, analogous to the photonic balls we described in Chapter 4, that can move in response to an electric field and change the color of a pixel. No matter what the system is, the rules for color are determined only by the structure and the refractive indices involved. Moreover, if the materials themselves are responsive to an external stimulus, such as temperature, pressure, or electric field, it is even possible to change

the color dynamically [70, 71, 72, 73].

Inspired by these potential applications, here we ask: what colors are possible with photonic glasses, and what are the requirements on the materials and their arrangement in order to make a complete set of visible colors? To begin answering these questions, we need to relate all that we have learned about the optical properties of photonic glasses to the colors that we actually see. With this goal in mind, here we present some preliminary results from converting the calculated reflection spectra of photonic glasses to RGB color values. We show that it is possible to create structural colors with a very wide range of hue and saturation using realistic system parameters. Our conclusions share the same limitations as our model: they are only valid if single elastic scattering is the primary determinant of color. However, even if this assumption turns out to be invalid in some cases, the algorithm that we use can be easily adapted to subsequent versions of the model. In this way, we hope to pave the way towards bridging the gap between theory and application.

6.2 From Scattering Theory to Color

To find the color that corresponds to a reflection spectrum, we need to account for two factors: the spectrum of illumination and the responsivity of our eyes to light. The spectra we have so far been discussing do not represent the scattered intensity that reaches our eyes. They are normalized reflection spectra, meaning that they only contain information about the scattering properties of the material. The illumination spectrum has either been divided out, in our experimental measurements, or not included, in our theoretical calculations. However, illumination, too, affects

color. Assuming linear scattering, namely no absorption or frequency conversion, the scattered intensity is proportional to the incident intensity at all wavelengths – for instance, white objects appear red under red light. Therefore, to obtain the scattered intensity as a function of wavelength, we must first multiply the normalized reflection spectrum with the illumination spectrum. Moreover, our eyes are not equally sensitive to all wavelengths. Most of us detect light via three color cones, each of which is mostly sensitive to a different color: red, green, and blue [74]. The signal that reaches our brain and is interpreted as color is then proportional to a convolution of the scattered intensity with the wavelength sensitivity curves, or matching functions [75, 76, 77], of our color cones.

The calculation of RGB values from reflection spectra then becomes a relatively simple affair thanks to an open-source python package that was developed to perform precisely this task, ColorPy [78], appended with a script provided to us by Steve Byrnes. This code receives curves of normalized reflectivity versus wavelength, multiplies them with the spectrum of illumination of our choice, and calculates sRGB values, or standard RGB values, which is a widely used RGB color standard for electronic devices and printers [79, 80]. We acknowledge that, by definition, this algorithm cannot capture colors that are either more bright or more saturated than a display can show; and that the same sRGB value may yield a different color in different displays. Regardless, this is a good starting point for describing the colors of photonic glasses in terms of a widely accepted standard, and it is certainly appropriate for applications related to reflective displays. For other applications, a comparison with other color standards may be more suitable – such as the RAL or PANTONE color

standards for paints, coatings and plastics.

6.3 sRGB Colors of Photonic Glasses

To check the validity of this framework for calculating sRGB colors, we first apply it to the reflection spectra of our own colloidal glasses and compare the results to pictures of the samples. We make the samples out of poly-methylmethacrylate particles according to the procedure described in Chapter 3. We measure the reflection spectra as a function of wavelength with a fiber-optic spectrometer (OceanOptics HR2000+) mounted on an optical microscope (Nikon LV-100), and we illuminate the samples with a halogen lamp that is collimated by minimizing the condenser aperture. We collect the light scattered by the sample with a 50× objective (Nikon LU Plan Fluor, NA = 0.8) and we image it onto a detection fiber (OceanOptics QP600-2-UV/VIS) that is connected to the spectrometer. The range of scattering angles that we collect with this setup is limited by the objective NA: $2.2 < \theta < 3.14$ radians. Regardless, this range of angles is representative of the range relevant for natural lighting conditions, because total internal reflection at the sample–air interface sets a limit to the scattering angle at 2.4 radians – meaning that even under ambient illumination the range of scattering angles that are relevant for color is limited to $2.4 < \theta < 3.14$ radians. We normalize all spectra to the reflected intensity from an aluminum mirror, we average the spectra measured over five different locations on the sample, and we smooth the spectra using a 50-nm window; we have encountered the resulting curves in Figure 3.1. These spectra are our input to ColorPy, from which we calculate the corresponding sRGB values. In all our color calculations we assume sunlight illumina-

tion, meaning that we multiply the absolute spectra with the spectrum of illumination using a standard representation spectrum sunlight defined by the International Commission on Illumination, illuminant D65 [77]. To account for the responsivity of our camera to different wavelengths, we white-balance our pictures to a picture of white paper under the same illumination conditions.

6.4 Results and Discussion

Figure 6.1 shows the sRGB values and photographs for some of our photonic glasses. The calculated colors agree reasonably well with the colors we observe, suggesting that our framework is valid - at least for the colors that we have created in the lab.

Next, we investigate what colors are accessible with different glassy systems. Experimentally, there are six parameters that can be varied: the diameter of the colloidal spheres, which may include a core and a shell diameter, the refractive index of the spheres, the refractive index of the medium they are embedded in, their volume fraction and the material thickness (see Equation 3.6). In what follows we will focus on the particle dimensions and on the refractive indices of the particles and of the medium. We will assume a volume fraction $\phi = 0.5$ and a material thickness $l = 15$ μm, chosen to represent the thickness of industrial color coatings. Note that this thickness may, in some cases, be longer than the scattering length in the sample, meaning that the single-scattering approximation may not always be valid. The next iteration of this calculation should include an adjustment of the sample thickness based on the scattering length in the system.

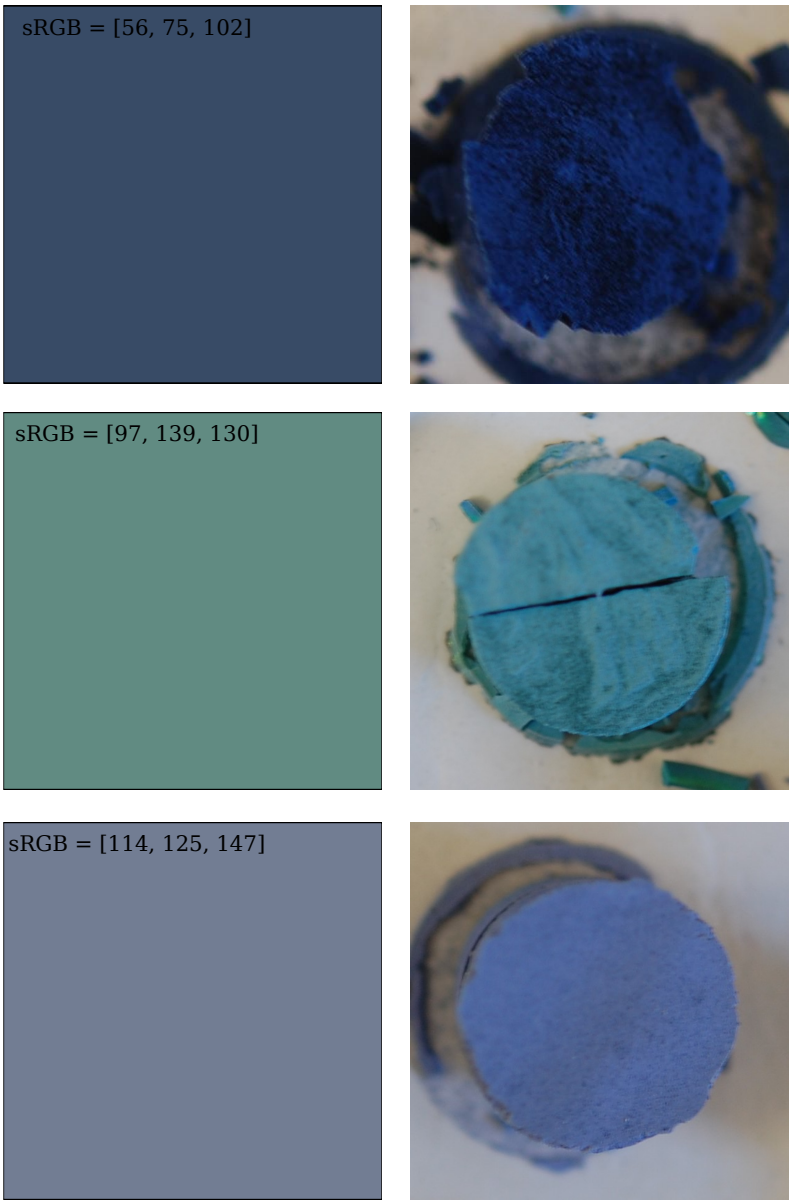

Figure 6.1: The sRGB values calculated from the measured reflection spectra of our colloidal glasses agree reasonably well with the appearance of the samples. Left column: sRGB colors calculated with ColorPy. Right column: pictures of colloidal glasses made with poly-methylmethacrylate particles.

Figure 6.2 shows the sRGB colors from four different systems of core-shell particles where the shells are index-matched to the medium. We plot the colors as a function of the core and shell radii, and we represent color saturation with darkness: the darker the color, the less saturated it is. Before we describe what each system is, a few general observations are of note. First, there appears to be a very wide range of structural colors that are accessible with photonic glasses. These colors generally redshift with increasing shell size, as one would expect: the larger the interparticle spacing, the longer the resonant wavelength, according to Equation 3.4. However, color hue is not only a function of the shell radius: sometimes the color can change with the core radius only, most noticeably in Figure 6.2(c). This is due to the form factor; while up until now we considered the form factor resonances a nuisance that prevented us from making red, here we see that we can actually use them to our advantage to tune the hue. Moreover, we see that each system has the potential to produce a different range of colors and that not all colors are possible in all systems. One color in particular is conspicuous in its absence: red.

In Figure 6.2(a) we consider inverse glasses made of air spheres in a medium with $n_{\text{medium}} = 1.4$, close to the index of colloidal silica that we make with the sol-gel process described in Chapter 5[64]. This is the type of system that we proposed in Chapter 3 could show red color: the small refractive index of the scattering cores is meant to ensure that the resonances of the form factor occur in the ultra-violet, leaving the resonances of the structure factor as the primary spectral feature. From the distribution of color hues in this graph we see that color is indeed primarily determined by the shell diameter, and that there are no significant changes in hue

along the axis of core radius. Unfortunately, however, there are no particle dimensions for which the sRGB color is a saturated red, although yellow and orange are both accessible. The specific system we propose, of air spheres with radius 130 nm in silica shells with radius 140 nm embedded in silica, is marked with the white arrow, and the corresponding color is orange. We attribute this lack of red color, despite a prominent scattering peak in the red, to the low sensitivity of the human eye at long wavelengths: it appears that not only is angle-independent red structural color difficult to make, but it is also difficult to see[74].

Figure 6.2(b) represents photonic glasses of polystyrene spheres in water, like the ones in our photonic balls of Chapter 4. The white arrow marks the row corresponding to cores with diameter 80 nm, as is the case for the particles we used. According to this graph, it appears that we could achieve more saturated long-wavelength colors with larger cores. This conclusion is not immediately obvious from our scattering model, based on which we proposed small cores for red color; it suggests that red-shifting the form factor resonances could also help. Overall, this system seems capable of producing a wide range of colors that sweep the visible range, from blue to pink. We note that the colors corresponding to the shell radii for our red (r =210 nm), green (r = 170 nm), and blue (r = 140 nm) photonic balls do not match our observations. This deviation may arise from the fact that the particles we use are soft, so their packings may not be accurately described by a structure factor for hard spheres.

Figure 6.2(c) describes an odd thought experiment: silica particles of refractive index 1.4 floating in air, separated by an invisible spacer with refractive index 1. This refractive index contrast is similar to most typical colloidal glass systems; the

arrows mark the sizes of the poly-methylmethacrylate spheres we used for the samples shown in Figure 6.1. The colors close to the diagonal for shell diameters above 130 nm are not very saturated: this is consistent with our experimental observations and occupied us extensively in Chapter 3. The colors we obtain with cores that are slightly smaller than the shells – corresponding to particles hovering in mid-air – are the most saturated of all.

This motivated us to look into an easier-to-assemble system with a similar refractive index contrast: titania particles in a medium with index 1.7. The resulting colors are shown in Figure 6.2(d). Alas, these colors are the dullest of all: high refractive index contrast does not seem to guarantee bright color.

These calculations are a visual rendering of our model for scattering from colloidal glasses. As such, they can provide insight in a number of ways. In fundamental studies, they can be used to quantify the effect of each of the system parameters on color. They can also serve as experimental guides, to estimate the tolerance in the particle sizes and to inform the fine-tuning of parameters for creating a certain color. Systematic deviations between the resulting colors and what these tables predict can point to flaws in our model and help construct a more accurate one.

At the same time, these results raise a lot of questions. For instance, are there overarching rules that describe the variety and intensity of the colors accessible with different systems? Why is the parameter space for yellow and orange wider than the parameter space for green? Why is red color so elusive, and why do we often get magenta or dark orange instead? The answers to these questions require a further understanding not only of scattering, but also of the response of our visual system to

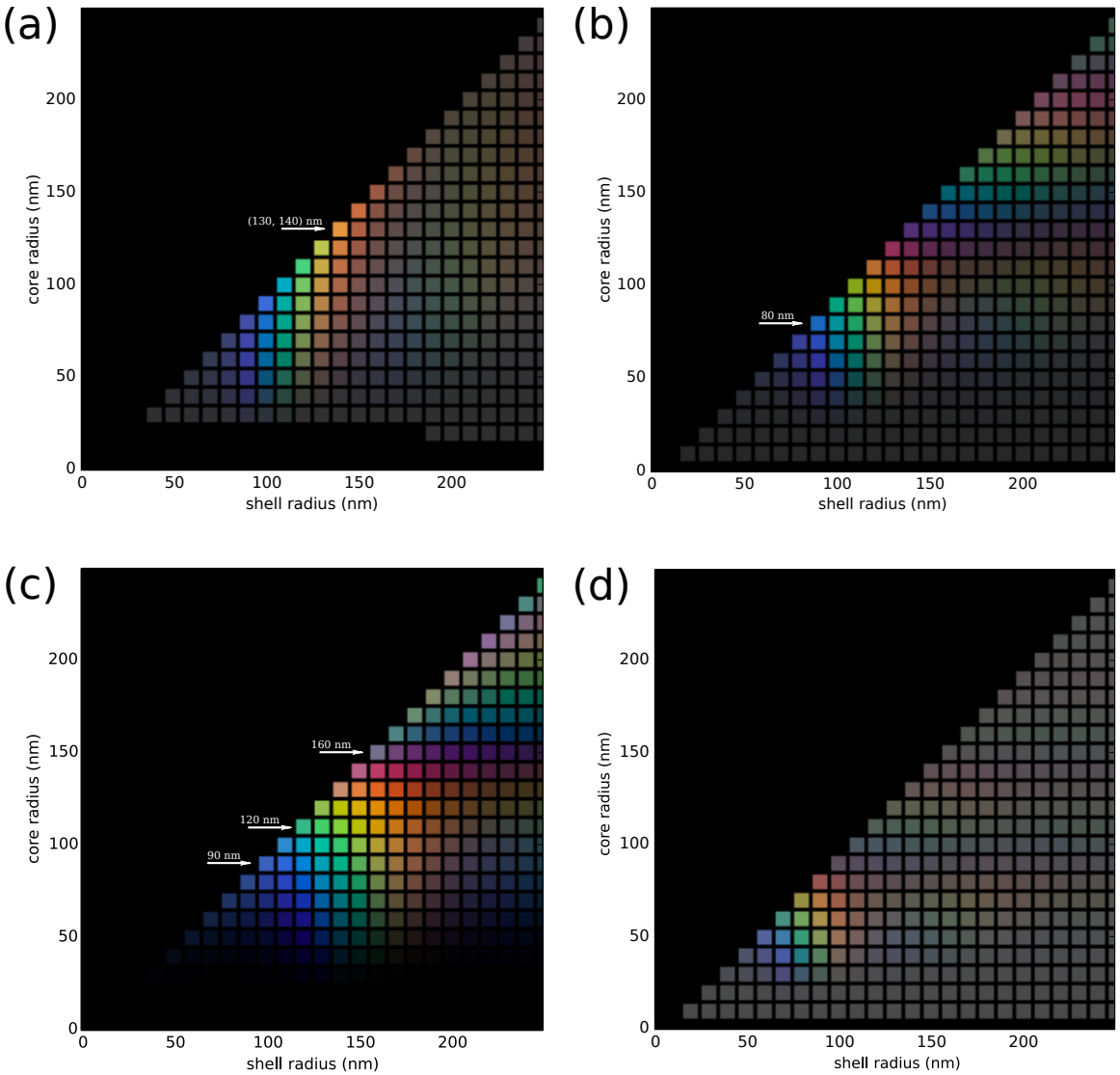

Figure 6.2: Our model predicts that colloidal glasses can produce a wide range of structural colors. Calculated sRGB colorsfor colloidal glasses of core-shell particles as a function of core and shell diameter. We used a thickness of 15μm and a volume fraction $\phi = 0.5$, and we have index-matched the shells to the medium. (a) Air-silica core-shell particles in silica. The colors are primarily determined by the shell diameter, indicating that the form factor does not have strong features in the visible. (b) Polystyrene scatterers in water. (c) Silica scatterers (n=1.4) suspended in air. In (b) and (c), the range of colors is fairly wide and the hue can be tuned with both the shell and the core diameter. (d) Titania cores in silica. While the refractive index contrast here is the same as in (c), the range and saturation of colors is limited.

color.

Our preliminary calculations are only the beginning of what we hope will continue as a "chromaticity study" of photonic glasses. In future studies, it will be interesting to use this algorithm to investigate the effect of other system parameters on color, such as the refractive index contrast, the volume fraction, or even the structure factor itself: perhaps there are other structures with isotropic optical properties that would be more suitable as photonic pigments than our photonic glasses.

6.5 Conclusion

We have combined our scattering model with an open-source algorithm to calculate RGB values for the colors of colloidal photonic glasses. With this code, we have demonstrated that colloidal photonic glasses can produce a wide range of colors that span the visible range – assuming that our model is valid. We have discussed the relevance of this type of calculation both for fundamental studies, where it can reveal underlying trends and guide experimental design, as well as for practical applications, where it can be used as a starting point for the identification of design rules for color. It is our hope that tables similar to the ones we present here may one day be used as reference points for the design and application of photonic glasses as pigments.

Chapter 7

Conclusion and Outlook

In this thesis we have studied the optical properties and colors of colloidal photonic glasses. In the theoretical part of our work, we have constructed the first model that accurately predicts the absolute reflectivity of a colloidal glass; we have provided a reason to explain the difficulty in making red color; and we have preliminary results to suggest that the range of possible colors far exceeds what has so far been created in the lab. In the experimental part of our work, we have created and studied novel colloidal systems that offer a high degree of control over scattering: glasses of core-shell particles with scattering cores and transparent shells, where the hue can be tuned independently of saturation; encapsulated suspensions of these particles, or photonic balls, in which incoherent scattering can be suppressed, leading to the first observation of a full-spectrum photonic glass system; and inverse glasses, where we expect to see more saturated, long-wavelength colors.

In subsequent work, the potential of inverse glasses needs to be investigated further. In particular, it will be interesting to use the core-shell architecture in an inverse

system. This could be achieved in numerous ways. Our calcination method for creating inverse glasses could easily be modified to include core-shell polymer-silica particles in the template, instead of simple polymer particles, leading to inverse structures where the size of the air cores can be controlled independently of the spacing between them. Such particles have already been synthesized [81]; our collaborator Gi-Ra Yi and his students are currently working on providing us with a batch for structural color applications. Similarly, our infiltration protocol can as easily be applied to glasses of core-shell particles with low-index cores. My colleague Jin-Gyu Park has already synthesized polymer particles with low refractive index, on the order of 1.38, using a fluorinated monomer, 1H,1H-heptafluorobutylmethacrylate. Covering these particles with a polymer shell has turned out to be challenging due to their different wetting properties, and further experiments on synthesis are required to find a material for the shell that is compatible. Along similar lines, Dr. Park has also synthesized polystyrene-poly(tert buthylmethacrylate) core-shell particles, which, if the sequence of materials can be inverted, can also be used in infiltrated inverse glasses.

A natural extension to particles with two layers is particles with many layers. One idea we originally had to obtain structural red color was to include in our glasses multi-layered particles as anti-reflection coatings for blue wavelengths. We have since analytically shown and independently learned that a stack of dielectrics on a spherical surface cannot establish perfect destructive interference [82]. Regardless, a multi-layer architecture can offer even more precise control over the form factor. The potential advantages of this approach can be checked readily, as our code for calculating the single particle scattering cross section can be applied to particles with an arbitrary

number of layers.

At a higher level, we have not at all investigated whether a glassy structure is optimal for angle-independent structural color. Are there other structure factors that lead to more saturated colors? By symmetry, we know that, to obtain angle-independent structural color, we need an isotropic material with long-range disorder – unless we wait for a complete band gap to be realized with a photonic crystal in the visible. From Fourier theory, we also know that we need some degree of order, characterized by some lengthscale, in order to have constructive interference and color. But we do not currently know whether there is an optimum value for the spatial extent of the short-range order, or an optimum class for its local symmetries. In glassy packings of spherical particles, the pockets of order usually have the form of slightly distorted hexagonal packings. This local geometry defines the location of the first peak of the structure factor, since it determines the average spacing between coordination shells. It is conceivable, then, that the first peak of the structure factor could be controlled by imposing a different geometry of short-range order, for example by randomly packing particle *clusters* instead of individual particles. This is certainly within the realm of possibility, since techniques for the assembly of colloidal clusters of various sizes and shapes have already been established [83, 84, 85].

Turning more directly to applications, another open question pertains to the optimal thickness of a photonic glass. It has already been discussed that, if the samples are too thick, incoherent multiple scattering overwhelms coherent single scattering, bleaching any structural color [16]. But the converse question has not been answered: how *thin* can a photonic glass be and still have a saturated, visible color? This is

particularly relevant for coating applications, where the film thickness cannot exceed a few dozen micrometers. Our newest recruit, Victoria Hwang, is currently addressing this question experimentally, with microfluidic techniques that allow her to create colloidal glasses with precisely controlled thickness.

Moreover, a striking feature of structural colors that cannot be matched with conventional pigments is their potential to be interactive and dynamically tunable. We have begun exploring this feature with temperature-tunable photonic crystals of core-shell particles that can be synthesized to span the visible range over a variety of temperature ranges [73]. This concept can be extended to temperature-tunable glasses. Other ways to make tunable structural colors could be by embedding small magnets in them, or using dielectrophoretic materials that, when placed between two electrodes, can either be displaced or swollen, leading to a change in appearance – for instance, in the pixel of a reflective electronic display.

Finally, no application of photonic pigments will be very appealing if their colors are not comparable to what we already have with absorbing dyes. To ensure that the color-fastness and dynamic tunability of structural colors does not come with aesthetic compromises, we hope that our calculations of the RGB colors of colloidal glasses will inspire a more thorough chromaticity study aimed at identifying the key parameters for color saturation and hue.

While this work has helped elucidate some aspects of the physics behind the colors of photonic glasses, we hope to have also shown that these can be just the first steps of an exciting quest.

Bibliography

[1] John Ballato. Tailoring visible photonic bandgaps through microstructural order and coupled material effects in SiO_2 colloidal crystals. *J. Opt. Soc. Am. B*, 17(2):219–225, Feb 2000.

[2] L. F. Rojas-Ochoa, J. M. Mendez-Alcaraz, J. J. Sáenz, P. Schurtenberger, and F. Scheffold. Photonic properties of strongly correlated colloidal liquids. *Phys. Rev. Lett.*, 93:073903, Aug 2004.

[3] Mary L. Boas. *Mathematical Methods in the Physical Sciences*. Wiley, third edition, 2006.

[4] P. M. Chaikin and T. C. Lubensky. *Principles of Condensed Matter Physics*. Cambridge University Press, 2007.

[5] Richard O. Prum, Rodolfo H. Torres, Scott Williamson, and Jan Dyck. Coherent light scattering by blue feather barbs. *Nature*, 396, Nov 1998.

[6] Vinodkumar Saranathan, Jason D. Forster, Heeso Noh, Seng-Fatt Liew, Simon G. J. Mochrie, Hui Cao, Eric R. Dufresne, and Richard O. Prum. Structure and optical function of amorphous photonic nanostructures from avian feather barbs: a comparative small angle x-ray scattering (SAXS) analysis of 230 bird species. *Journal of The Royal Society Interface*, 2012.

[7] Lei Shi, Haiwei Yin, Renyuan Zhang, Xiaohan Liu, Jian Zi, and Dongyuan Zhao. Macroporous oxide structures with short-range order and bright structural coloration: a replication from parrot feather barbs. *J. Mater. Chem.*, 20:90–93, 2010.

[8] Richard O. Prum and Rodolfo H. Torres. Structural colouration of mammalian skin: convergent evolution of coherently scattering dermal collagen arrays. *Journal of Experimental Biology*, 207(12):2157–2172, 2004.

[9] Gang Sheng Zhang and Zeng Qiong Huang. Two-dimensional amorphous photonic structure in the ligament of bivalve lutraria maximum. *Opt. Express*, 18(13):13361–13367, Jun 2010.

[10] Eric R. Dufresne, Heeso Noh, Vinodkumar Saranathan, Simon G. J. Mochrie, Hui Cao, and Richard O. Prum. Self-assembly of amorphous biophotonic nanostructures by phase separation. *Soft Matter*, 5:1792–1795, 2009.

[11] L.S. Froufe-Pérez, S. Albaladejo, E. Sahagún, P. García-Mochales, M. Reufer, F. Scheffold, and J.J. Sáenz. Light transport through photonic liquids. In *Noise and Fluctuations: 18th International Conference on Noise and Fluctuations – ICNF 2005*. American Institute of Physics, 2005.

[12] Mathias Reufer, Luis Fernando Rojas-Ochoa, Stefanie Eiden, Juan José Sáenz, and Frank Scheffold. Transport of light in amorphous photonic materials. *Applied Physics Letters*, 91(17), 2007.

[13] Pedro David García, Riccardo Sapienza, and Cefe López. Photonic glasses: A step beyond white paint. *Advanced Materials*, 22(1):12–19, 2010.

[14] P. D. García, R. Sapienza, J. Bertolotti, M. D. Martín, Á Blanco, A. Altube, L. Viña, D. S. Wiersma, and C. López. Resonant light transport through Mie modes in photonic glasses. *Phys. Rev. A*, 78:023823, Aug 2008.

[15] Heeso Noh, Seng Fatt Liew, Vinodkumar Saranathan, Simon G. J. Mochrie, Richard O. Prum, Eric R. Dufresne, and Hui Cao. Structural color: How non-iridescent colors are generated by quasi-ordered structures of bird feathers. *Advanced Materials*, 22(26-27), 2010.

[16] Jason D. Forster, Heeso Noh, Seng Fatt Liew, Vinodkumar Saranathan, Crl F. Schreck, Lin Yang, Jin-Gyu Park, Richard O. Prum, Simon G. J. Mochrie, Corey S. O'Hern, Hui Cao, and Eric R. Dufresne. Biomimetic isotropic nanostructures for structural coloration. *Advanced Materials*, 22(26-27):2939–2944, 2010.

[17] Mohammad Harun-Ur-Rashid, Abu Bin Imran, Takahiro Seki, Masahiko Ishii, Hiroshi Nakamura, and Yukikazu Takeoka. Angle-independent structural color in colloidal amorphous arrays. *ChemPhysChem*, 11(3):579–583, 2010.

[18] Kazuhide Ueno, Aya Inaba, Yuta Sano, Masashi Kondoh, and Masayoshi Watanabe. A soft glassy colloidal array in ionic liquid, which exhibits homogeneous, non-brilliant and angle-independent structural colours. *Chemical Communications*, pages 3603–3605, 2009.

[19] Kazuhide Ueno, Yuta Sano, Aya Inaba, Masashi Kondoh, and Masayoshi Watanabe. Soft glassy colloidal arrays in an ionic liquid: Colloidal glass transition, ionic transport, and structural color in relation to microstructure. *The Journal of Physical Chemistry B*, 114(41):13095–13103, 2010. PMID: 20879726.

[20] Yukikazu Takeoka, Shinya Yoshioka, Atsushi Takano, Shigeo Arai, Khanin Nueangnoraj, Hirotomo Nishihara, Midori Teshima, Yumiko Ohtsuka, and Takahiro Seki. Production of colored pigments with amorphous arrays of black and white colloidal particles. *Angewandte Chemie International Edition*, 52(28):7261–7265, 2013.

[21] Dengteng Ge, Lili Yang, Gaoxiang Wu, and Shu Yang. Spray coating of superhydrophobic and angle-independent coloured films. *Chem. Commun.*, 50:2469–2472, 2014.

[22] Yukikazu Takeoka, Masaki Honda, Takahiro Seki, Masahiko Ishii, and Hiroshi Nakamura. Structural colored liquid membrane without angle dependence. *ACS Applied Materials & Interfaces*, 1(5):982–986, 2009. PMID: 20355881.

[23] Insook Lee, Daihyun Kim, Jinha Kal, Heeyoel Baek, Dongwoo Kwak, Dahyeon Go, Eunjoo Kim, Changjoon Kang, Jeyon Chung, Yulim Jang, Seungwook Ji, Jaehyun Joo, and Youngjong Kang. Quasi-amorphous colloidal structures for electrically tunable full-color photonic pixels with angle-independency. *Adv. Mater.*, 44:4973–4977, 2010.

[24] Yoshie Gotoh, Hiromasa Suzuki, Naomi Kumano, Takahiro Seki, Kiyofumi Katagiri, and Yukikazu Takeoka. An amorphous array of poly(N-isopropylacrylamide) brush-coated silica particles for thermally tunable angle-independent photonic band gap materials. *New J. Chem.*, 36:2171–2175, 2012.

[25] Krassimir P. Velikov, Alexander Moroz, and Alfons van Blaaderen. Photonic crystals of core-shell colloidal particles. *Applied Physics Letters*, 80(1):49–51, 2002.

[26] Matthias Karg, Thomas Hellweg, and Paul Mulvaney. Self-assembly of tunable nanocrystal superlattices using poly-(NIPAM) spacers. *Advanced Functional Materials*, 21(24):4668–4676, 2011.

[27] Gwenaelle Bazin and X. X. Zhu. Understanding the thermo-sensitivity of crystalline colloidal arrays formed by poly(styrene-co-N-isopropylacrylamide) core-shell microspheres. *Soft Matter*, 8:1909–1915, 2012.

[28] Adeline Perro, Guangnan Meng, Jerome Fung, and Vinothan N. Manoharan. Design and synthesis of model transparent aqueous colloids with optimal scattering properties. *Langmuir*, 25(19):11295–11298, 2009.

[29] Johan Mattsson, Hans M. Wyss, Alberto Fernandez-Nieves, Kunimasa Miyazaki, Zhibing Hu, David R. Reichman, and David A. Weitz. Soft colloids make strong glasses. *Nature*, 462:83–86, Nov 2009.

[30] L. F. Rojas, C. Urban, P. Schurtenberger, T. Gisler, and H. H. von Grünberg. Reappearance of structure in colloidal suspensions. *Europhys.Lett.*, 60:802–808, Dec 2002.

[31] J. W. Goodwin, J. Hearn, C. C. Ho, and R. H. Ottewill. Studies on the preparation and characterisation of monodisperse polystyrene latices. *Colloid and Polymer Sci.*, 252(6):464–471, 1974.

[32] N. Dingenouts, Ch. Norhausen, and M. Ballauff. Observation of the volume transition in thermosensitive core-shell latex particles by small-angle X-ray scattering. *Macromolecules*, 31(25):8912–8917, 1998.

[33] Sho Asakura and Fumio Oosawa. On interaction between two bodies immersed in a solution of macromolecules. *Journal of Chemical Physics*, 22:1255–1256, 1954.

[34] Sho Asakura and Fumio Oosawa. Interaction between particles suspended in solutions of macromolecules. *Journal of Polymer Science*, 33(126):183–192, 1958.

[35] Craig F. Bohren and Donald R. Huffman. *Absorption and Scattering of Light by Small Particles*. Wiley-VCH, 2004.

[36] Michael J Rust, Mark Bates, and Xiaowei Zhuang. Sub-diffraction-limit imaging by stochastic optical reconstruction microscopy (STORM). *Nature Methods*, 3:793–796, Oct 2006.

[37] Eric Betzig, George H. Patterson, Rachid Sougrat, O. Wolf Lindwasser, Scott Olenych, Juan S. Bonifacino, Michael W. Davidson, Jennifer Lippincott-Schwartz, and Harald F. Hess. Imaging intracellular fluorescent proteins at nanometer resolution. *Science*, 313(5793):1642–1645, 2006.

[38] J. C. Maxwell Garnett. Colours in metal glasses and in metallic films. *Phil. Trans. R. Soc. Lond. A*, 203:385–420, 1904.

[39] Willem L. Vos, Rudolf Sprik, Alfons van Blaaderen, Arnout Imhof, Ad Lagendijk, and Gerard H. Wegdam. Strong effects of photonic band structures on the diffraction of colloidal crystals. *Phys. Rev. B*, 53:16231–16235, Jun 1996.

[40] Sofia Magkiriadou, Jin-Gyu Park, Young-Seok Kim, and Vinothan N. Manoharan. Disordered packings of core-shell particles with angle-independent structural colors. *Opt. Mater. Express*, 2(10):1343–1352, Oct 2012.

[41] Naomi Kumano, Takahiro Seki, Masahiko Ishii, Hiroshi Nakamura, and Yukikazu Takeoka. Tunable angle-independent structural color from a phase-separated porous gel. *Angew. Chem. Int. Ed.*, 50(17):4012–4015, 2011.

[42] Jin-Gyu Park, Shin-Hyun Kim, Sofia Magkiriadou, Tae Min Choi, Young-Seok Kim, and Vinothan N. Manoharan. Full-spectrum photonic pigments with non-iridescent structural colors through colloidal assembly. *Angewandte Chemie*, 126(11):2943–2947, 2014.

[43] B. Q. Dong, X. H. Liu, T. R. Zhan, L. P. Jiang, H. W. Yin, F. Liu, and J. Zi. Structural coloration and photonic pseudogap in natural random close-packing photonic structures. *Opt. Express*, 18(14):14430–14438, Jul 2010.

[44] Seng Fatt Liew, Jin-Kyu Yang, Heeso Noh, Carl F. Schreck, Eric R. Dufresne, Corey S. O'Hern, and Hui Cao. Photonic band gaps in three-dimensional network structures with short-range order. *Phys. Rev. A*, 84:063818, Dec 2011.

[45] Liliana D'Alba, Vinodkumar Saranathan, Julia A. Clarke, Jakob A. Vinther, Richard O. Prum, and Matthew D. Shawkey. Colour-producing β-keratin nanofibres in blue penguin (Eudyptula minor) feathers. *Biology Letters*, 7(4):543–546, 2011.

[46] Heeso Noh, Seng Fatt Liew, Vinodkumar Saranathan, Richard O. Prum, Simon G. J. Mochrie, Eric R. Dufresne, and Hui Cao. Double scattering of light from biophotonic nanostructures with short-range order. *Opt. Express*, 18(11):11942–11948, May 2010.

[47] Heeso Noh, Seng Fatt Liew, Vinodkumar Saranathan, Richard O. Prum, Simon G. J. Mochrie, Eric R. Dufresne, and Hui Cao. Contribution of double scattering to structural coloration in quasiordered nanostructures of bird feathers. *Phys. Rev. E*, 81:051923, May 2010.

[48] P. D. Kaplan, A. D. Dinsmore, A. G. Yodh, and D. J. Pine. Diffuse-transmission spectroscopy: A structural probe of opaque colloidal mixtures. *Phys. Rev. E*, 50:4827–4835, Dec 1994.

[49] Gustav Mie. Contributions to the optics of turbid media, particularly of colloidal metal solutions. *Annalen der Physik*, 25(3):377–445, 1908.

[50] Jerome K. Percus and George J. Yevick. Analysis of classical statistical mechanics by means of collective coordinates. *Phys. Rev.*, 110:1–13, Apr 1958.

[51] Eugene Hecht. *Optics*. Addison Wesley, 2002.

[52] Refractive index database. `http://refractiveindex.info` (accessed October 27 2014), 2008–2014.

[53] Hein L. Leertouwer, Bodo D. Wilts, and Doekele G. Stavenga. Refractive index and dispersion of butterfly chitin and bird keratin measured by polarizing interference microscopy. *Opt. Express*, 19(24):24061–24066, Nov 2011.

[54] Mary Caswell Stoddard and Richard O. Prum. How colorful are birds? Evolution of the avian plumage color gamut. *Behavioral Ecology*, 22:1042–1052, 2011.

[55] Sofia Magkiriadou, Jin-Gyu Park, Young-Seok Kim, and Vinothan N. Manoharan. Absence of red structural color in photonic glasses, bird feathers, and certain beetles. *Phys. Rev. E*, 90:062302, Dec 2014.

[56] Shin-Hyun Kim, Jin Woong Kim, Jun-Cheol Cho, and David A. Weitz. Double–emulsion drops with ultra–thin shells for capsule templates. *Lab Chip*, 11:3162–3166, 2011.

[57] Ki-Hyun Kim, Nhu-Thuc Phan, Yong-Hyun Kim, Hye-On Yoon, and Richard J. C. Brown. Major sources of uncertainties in the analysis of methylmercury using gold amalgamation sampling. *Anal. Methods*, 5:3068–3073, 2013.

[58] P. Jiang, J. F. Bertone, K. S. Hwang, and V. L. Colvin. Single-crystal colloidal multilayers of controlled thickness. *Chemistry of Materials*, 11(8):2132–2140, 1999.

[59] D.J. Norris, E.G. Arlinghaus, L. Meng, R. Heiny, and L.E. Scriven. Opaline photonic crystals: How does self–assembly work? *Advanced Materials*, 16(16):1393–1399, 2004.

[60] Orlin D. Velev, Abraham M. Lenhoff, and Eric W. Kaler. A class of microstructured particles through colloidal crystallization. *Science*, 287(5461):2240–2243, 2000.

[61] Shin-Hyun Kim, Su Yeon Lee, Gi-Ra Yi, David J. Pine, and Seung-Man Yang. Microwave-assisted self-organization of colloidal particles in confining aqueous droplets. *Journal of the American Chemical Society*, 128(33):10897–10904, 2006. PMID: 16910685.

[62] Benjamin Hatton, Lidiya Mishchenko, Stan Davis, Kenneth H. Sandhage, and Joanna Aizenberg. Assembly of large-area, highly ordered, crack-free inverse opal films. *Proceedings of the National Academy of Sciences*, 107(23):10354–10359, 2010.

[63] P.N. Pusey. The effect of polydispersity on the crystallization of hard spherical colloids. *Journal de Physique France*, 48(5):709–712, 1987.

[64] Katherine Phillips et al. In preparation.

[65] Katherine R. Phillips, Nicolas Vogel, Yuhang Hu, Mathias Kolle, Carole C. Perry, and Joanna Aizenberg. Tunable anisotropy in inverse opals and emerging optical properties. *Chemistry of Materials*, 26(4):1622–1628, 2014.

[66] M. Jansen and H.P. Letschert. Inorganic yellow-red pigments without toxic metals. *Nature*, 404:980–982, 2000.

[67] Wendusu, Toshiyuki Masui, and Nobuhito Imanaka. Novel environment-friendly inorganic red pigments based on (Bi, Er, Y, Fe)$_2$O$_3$ solid solutions. *Journal of Asian Ceramic Societies*, 2(3):195–198, 2014.

[68] Andrew R. Parker and David R. McKenzie. The cause of 50 million-year-old colour. *Proceedings of the Royal Society of London. Series B: Biological Sciences*, 270(Suppl 2):S151–S153, 2003.

[69] Maria E. McNamara, Derek E. G. Briggs, Patrick J. Orr, Sonja Wedmann, Heeso Noh, and Hui Cao. Fossilized biophotonic nanostructures reveal the original colors of 47-million-year-old moths. *PLoS Biol*, 9(11), 2011.

[70] Justin D. Debord and L. Andrew Lyon. Thermoresponsive photonic crystals. *The Journal of Physical Chemistry B*, 104(27):6327–6331, 2000.

[71] Ji-Hwan Kang, Jun Hyuk Moon, Seung-Kon Lee, Sung-Gyu Park, Se Gyu Jang, Shu Yang, and Seung-Man Yang. Thermoresponsive hydrogel photonic crystals by three-dimensional holographic lithography. *Advanced Materials*, 20(16):3061–3065, 2008.

[72] Mathias Kolle, Alfred Lethbridge, Moritz Kreysing, Jeremy J. Baumberg, Joanna Aizenberg, and Peter Vukusic. Bio-inspired band-gap tunable elastic optical multilayer fibers. *Advanced Materials*, 25(15):2239–2245, 2013.

[73] Jin-Gyu Park, W. Benjamin Rogers, Sofia Magkiriadou, Tom Kodger, Shin-Hyun Kim, Young-Seok Kim, and Vinothan N. Manoharan. Photonic-crystal hydrogels with a rapidly tunable stop band and high reflectivity across the visible. *Angewandte Chemie*, submitted.

[74] Margaret Livingstone. *Vision and art: the biology of seeing*. Harry N. Abrams, 2002.

[75] W.D. Wright. A re-determination of the trichromatic coefficients of the spectral colours. *Transactions of the Optical Society*, 30(4):141, 1929.

[76] T. Smith and J. Guild. The C.I.E. colorimetric standards and their use. *Transactions of the Optical Society*, 33(3):73, 1931.

[77] Commission Internationale de l'Eclairage. http://www.cie.co.at/ (accessed October 28 2014), 2000–2014.

[78] Mark Kness. ColorPy - A Python package for handling physical descriptions of color and light spectra. http://markkness.net/colorpy/ColorPy.html (accessed October 28 2014), 2008.

[79] Michael Stokes (Hewlett-Packard), Matthew Anderson (Microsoft), Srinivasan Chandrasekar (Microsoft), and Ricardo Motta (Hewlett-Packard). A standard default color space for the internet – sRGB. http://www.w3.org/Graphics/Color/sRGB.html, 1996.

[80] International Color Consortium. sRGB. http://www.color.org/chardata/rgb/srgb.xalter.

[81] Yu Lu, Joe McLellan, and Younan Xia. Synthesis and crystallization of hybrid spherical colloids composed of polystyrene cores and silica shells. *Langmuir*, 20(8):3464–3470, 2004. PMID: 15875883.

[82] Alex Small, Sheng Hong, and David Pine. Scattering properties of core-shell particles in plastic matrices. *Journal of Polymer Science Part B: Polymer Physics*, 43(24):3534–3548, 2005.

[83] Vinothan N. Manoharan, Mark T. Elsesser, and David J. Pine. Dense packing and symmetry in small clusters of microspheres. *Science*, 301(5632):483–487, 2003.

[84] Stefano Sacanna and David J. Pine. Shape-anisotropic colloids: Building blocks for complex assemblies. *Current Opinion in Colloid & Interface Science*, 16(2):96–105, 2011.

[85] Nicholas B. Schade, Miranda C. Holmes-Cerfon, Elizabeth R. Chen, Dina Aronzon, Jesse W. Collins, Jonathan A. Fan, Federico Capasso, and Vinothan N. Manoharan. Tetrahedral colloidal clusters from random parking of bidisperse spheres. *Phys. Rev. Lett.*, 110:148303, Apr 2013.

[86] Boualem Hammouda. *Probing Nanoscale Structures – The SANS Toolbox*. National Institute of Standards and Technology, 2010.

Appendix A

Protocol for Inverse Glasses of Air Cavities in Silica

In this appendix we describe our protocol for making inverse glasses of air cavities in a silica matrix. This protocol was established by Nicolas Vogel and Katherine Phillips.

For all steps including the piranha solution, you must wear acid gloves and a protective mask.

A.1 Clean the substrates

It is important that the surfaces of the substrates are very clean, so that the particles will assembly uniformly on them.

1. Cut glass slides or silica wafers into pieces of about the same length as the height of the vials you will use and of width that fits into these vials.

2. Immerse (carefully, no splashing!) the susbtrates into a piranha solution (1:3 hydrogen peroxide:sulfuric acid) at approx 80°C. Avoid having overlapping surfaces, so that the solution can access and clean the entire substrate surface. You should wear acid gloves and a protective mask for this step.

3. Let the substrates sit for about half an hour.

4. If you want to prepare twin samples (see E) keep several pieces of cut out glass or silica to use as spacers.

A.2 Prepare the silica precursor

1. In a glass vial, add 2.5 g hydrochloric acid 0.1mol/l (you can buy it like this)
2. 3.75 g ethanol
3. and 2.5 g silica precursor (Tetraethylorthosilicate, TEOS).
4. Add a magnetic mixer
5. and let the solution mix for one hour.

A.3 Prepare the colloidal suspensions

For opals, aim for a final suspension of 0.1wt% (for polystyrene). For glasses, prepare a bidisperse suspension where the particle number ratio of the two species is about 1.

1. Figure out what amounts of colloidal suspension you need based on the volume

fractions of what you have.

2. Rinse glass vials with DI water.

3. Fill glass vials with the desired water amount. If your colloidal suspensions are at around 4wt% and you are using 20mL vials, you can fill the vials with ∼20mL if you fill them up to the vial shoulder. The additional volume of colloidal suspension will be on the order of 0.5mL or less.

4. Add the colloids and the hydrolysed TEOS solution (140 μl in a 20 ml vial with 0.1wt-% colloids).

5. Sonicate the suspensions for a few minutes.

A.4 Retrieve the substrates

1. Add DI water into a glass container.

2. Carefully remove the substrates from the piranha solution with tweezers, maintaining the surface orientation. You should wear acid gloves and a protective mask for this step.

3. Rinse each piece with DI water.

4. Dip it in a small vial of ethanol to replace the water with ethanol, so that it will dry more quickly.

5. Blow-dry it (for careful experimentalists, maintain the air flow towards the tweezers to avoid tweezer dirt from spreading onto your substrate).

6. Deposit on a clean surface, such as aluminum foil. Make sure the clean side is always facing up!

A.5 Assemble it all together for slow evaporation

During this step, the suspension will dry slowing, and capillary forces will drive the particles up on the glass slide, making them form a film.

1. If you want two samples per particle suspension: take a spacer and put a substrate on top of it (right side up). Pick up another substrate and make a sandwich with the previous two pieces, such that the spacer is in the middle and both clean surfaces are on the outside. Clamp it all together with two small paper clips, one along each of the two longer sides of the substrates.

2. Check that the substrates have approximately the right height from the clippers down, so that they do not touch the bottom of the vials that contain the particle suspensions.

3. Immerse the substrates into the suspensions checking that they are not touching the bottom. Adjust the clipper position if necessary. Make sure the substrates are suspended in the middle of the vial.

4. Transfer into the oven, which has been preheated to 65°C.

5. Leave for 48 hours.

A.6 Bake

During this step, the polymer particles burn and the silica is cintered. 1. Transfer into calcination oven.

2. Program the oven to reach 500°C in five hours, stay at that temperature for two hours, and then to cool back down to room temperature in five hours.

Appendix B

Analytic Structure Factor for a Glass of Hard Spheres

In this thesis we adopt the solution to the Ornstein-Zernike equation for the pair correlation function in a glass of hard spheres under the Perkus-Yevick approximation [50]. The details of this equation will not concern us here further. The solution that we used came from [86] and it has the following form:

$$S(y) = \frac{1}{1 - c(y, \phi)} \tag{B.1}$$

with

$$\begin{aligned} c(y,\phi) = &-24\phi\frac{(1+2\phi)^2}{(1-\phi)^4}\frac{\sin y - y\cos y}{y^3} \\ &-6\phi\frac{-(1+\phi/2)^2}{(1-\phi)^4}\frac{y^2\cos y - 2y\sin y - 2\cos y + 2}{y^4} \\ &-\phi\frac{(1+2\phi)^2}{2(1-\phi)^4}[\frac{1}{y^6}(y^4\cos y - 4y^3\sin y - 12y^2\cos y + 24y\sin y) + 24\cos y - 24)]. \end{aligned} \tag{B.2}$$